THEORY AND RESEARCH IN SCIENCE AND MATHEMATICS

EDITORS:
PROF.DR.E.NİHAL ERCAN
PROF.DR.HASAN AKGÜL

gece
kitaplığı

İmtiyaz Sahibi / Publisher • Yaşar Hız
Genel Yayın Yönetmeni / Editor in Chief • Eda Altunel
Editörler / Editors • Prof. Dr. E. Nihal Ercan
Prof. Dr. Hasan Akgül
Kapak & İç Tasarım / Cover & Interior Design • Gece Kitaplığı

Birinci Basım / First Edition • © Eylül 2020
ISBN • 978-625-7243-77-3

Gece Kitaplığı / Gece Publishing
Türkiye Adres / Turkey Address: Kızılay Mah. Fevzi Çakmak 1. Sokak
Ümit Apt. No: 22/A Çankaya / Ankara / TR
Telefon / Phone: +90 312 384 80 40
web: www.gecekitapligi.com
e-mail: gecekitapligi@gmail.com

Baskı & Cilt / Printing & Volume
Sertifika / Certificate No: 47083

Theory and Research in Science and Mathematics

Editors

Prof. Dr. E. Nihal Ercan
Prof. Dr. Hasan Akgül

gece kitaplığı

CONTENTS

Chapter 1

A SURVEY OF SOME COMPLEXES ABOUT ANTICANCER ACTIVITY APPEARED IN 2020

***Barbaros AKKURT*[1]**

***Altuğ Mert SEVİM*[2]**

---

[1] Lecturer, PhD. Istanbul Technical University, Mustafa İnan Central Library, 34469 Maslak, Sarıyer – İstanbul.

[2] Assoc. Prof. Dr., Istanbul Technical University, Faculty of Science and Letters, Department of Chemistry, 34469 Maslak, Sarıyer-İstanbul.

Different metal-ligand complexes (non-Schiff base derived)

Abyar and Tabrizi prepared a new coordination compound having an imidazole and juglone, and also prepared its oxovanadium(IV) complex **3** (see Figure 1). They report that pUC19 DNA was efficiently cleaved by the complex and hydrogen peroxide. *In vitro* cytotoxicity on cancer cell lines and fibroblasts that are not malignant were studied and they compared against the ligands free of the complex, the metal salt free of complex, and cisplatin as control (Abyar & Tabrizi, 2020).

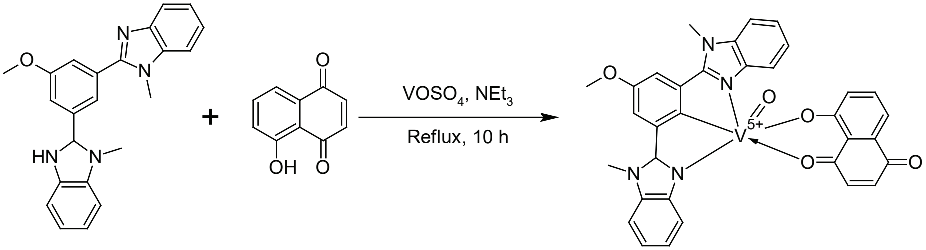

1 **2** **3**

Figure 1. *The preparation of the oxovanadium(V) complex (***3***) from a benzimidazole derivative (***1***) and juglone (***2***).*

New alpha-aminophosphonates were obtained with a one-pot procedure. Different copper(II) salts were used (see Figure 2). Two ligands **7** and **9**, along with their Cu(II) complexes, were tested against HT-29 and cisplatin for control. Complexes of **9** displayed better anticancer activity, whereas the ligand **7** did not show any activity. Ligand **9** showed a better activity than its complexes (Azzam et al., 2020).

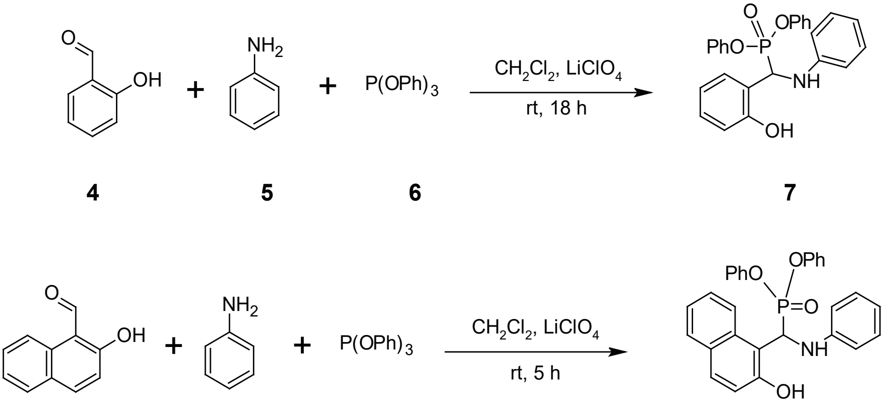

4 **5** **6** **7**

8 **5** **6** **9**

Figure 2. *New alpha-aminophosphonates for testing of antitumoral activity.*

A group of authors from Argentina has showed the antimetastatic activity of tropolone copper(II) complex [Cu(trp)$_2$] (**10**, see Figure 3) in human breast cancer cells. Cytotoxicity studies show that the complex shows better antitumoral activity than cisplatin (Balsa et al., 2020).

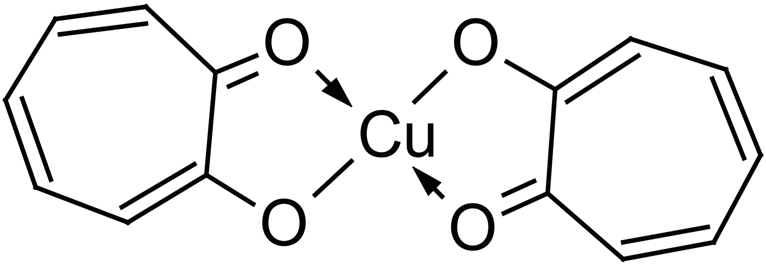

10

Figure 3. *The structure of bis(tropolonato)copper(II).*

Hepatocellular carcinoma (HCC) is recently known to increase thioredoxin reductase (TrxR) levels, which might be used as a marker. In the study, four gold(III) complexes (see Figures 4 and 5) were synthesized and characterized. Compound **14** showed the highest activity against HCC (Bian et al., 2020).

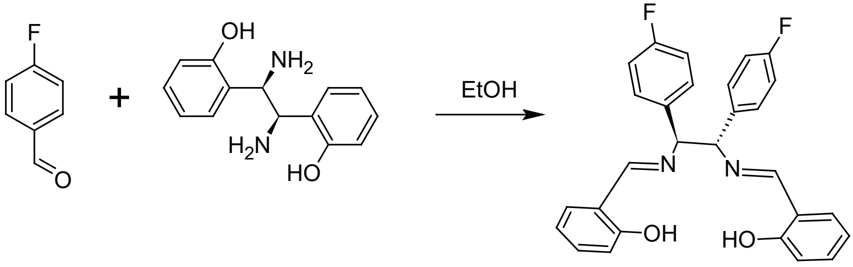

11 **12** **13**

Figure 4. *Formation of the Schiff's base from 4-fluorobenzaldehyde (***11***) and 1,2-bis(2-hydroxyphenyl)-1,2-diaminoethane (***12***).*

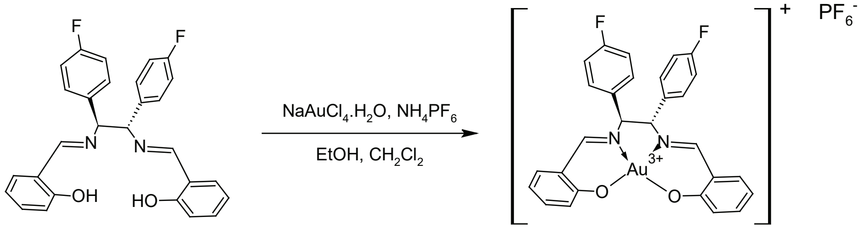

13 **14**

Figure 5. *Formation of the gold(III) complex (***14***) from the Schiff's base* **13**.

Ruthenium species are employed in chemotherapy, but they do not have the features of specific targeting and controlled release. The authors synthesized a prodrug Ru(III) complex, including 5-aminophenanthroline, dimethylsulfoxide, and chloro ligands and reduced this to the corresponding Ru(II), which is very reactive, blocking the replication of DNA and coordination that led to cleavage of nuclear DNA (Chen et al., 2020).

o- and p-phenylenediacetic acid reacts with $Cd(NO_3)_2•4H_2O$ in the presence of bis(imidazolyl)benzene co-ligand. In this study, two new polymeric Cd(II) complexes have been prepared. Furthermore, these two complexes were tested on MG-63 cells (Han et al., 2020).

Eight Sn(IV) complexes (see Figures 6-10) were prepared. MTT assays were used for the cytotoxicity of all complexes against MCF-7, NCI-H460, and HepG2. Diorganotin complexes' *in vitro* activity was better than that of monoorganotin complexes. The dibutyltin compound featured a very good activity against HepG2 and MCF-7 (W. Jiang et al., 2020).

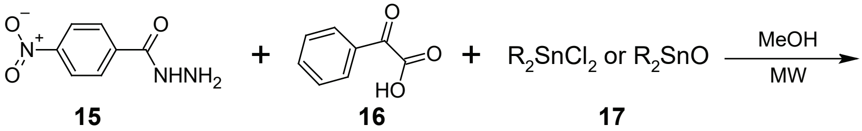

Figure 6. *The first part of the reaction. Eight tin complexes resulted.*

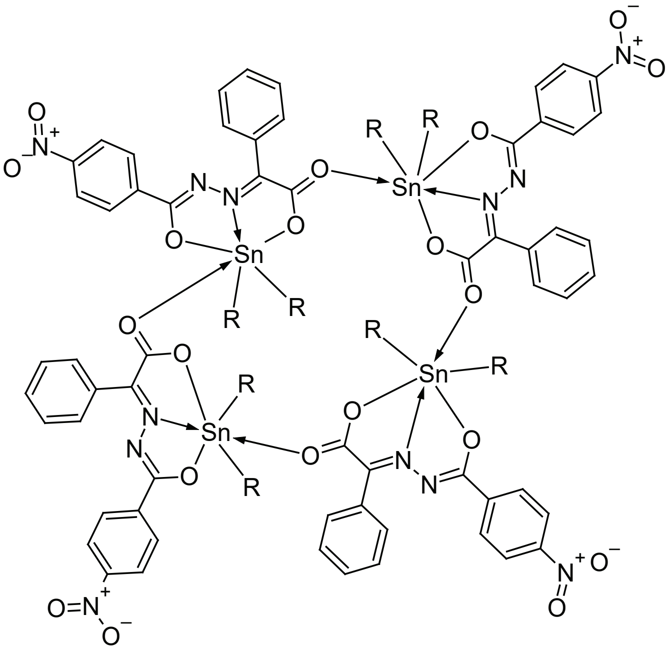

18

Figure 7. *The tetrameric tin complex. The R is phenyl.*

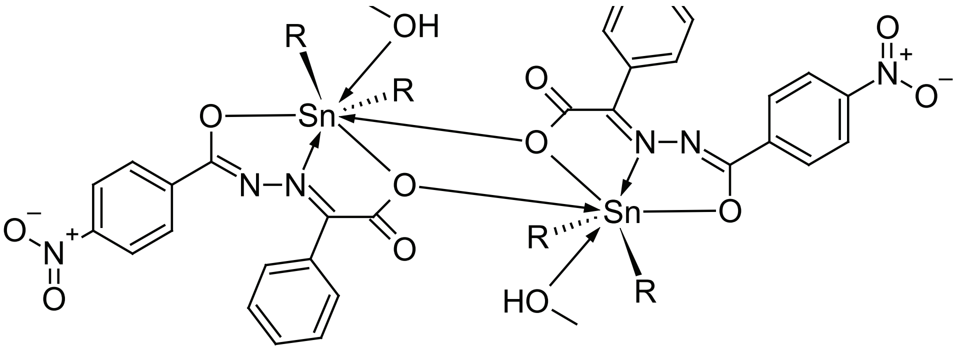

19

Figure 8. *The dimeric tin complex. The R is n-butyl, benzyl, p-methylbenzyl, and o-chlorobenzyl.*

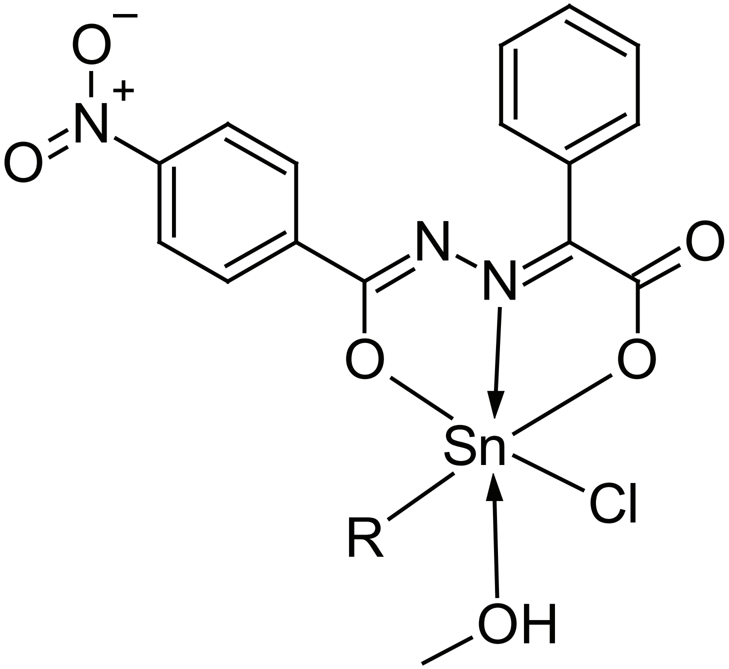

20

Figure 9. *The monomeric tin complex. The R is o-methoxybenzyl and p-chlorobenzyl.*

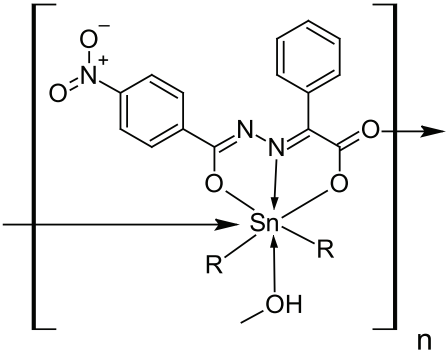

21

Figure 10. *The polymeric tin complex. The R is 2,4-dichlorobenzyl.*

Jiang and coworkers reported two new ruthenium(II) complexes having polypyridyl moieties (see Figures 11 and 12). In addition, the complexes Ru(II)-1 and Ru(II)-2, yielded good cytotoxicity on A549 cells. These values were higher than the ligands, the control drug cisplatin, and other related Ru(II) complexes. It is understood that these two complexes could be suitable candidates in the treatment of tumors (G.-B. Jiang et al., 2020).

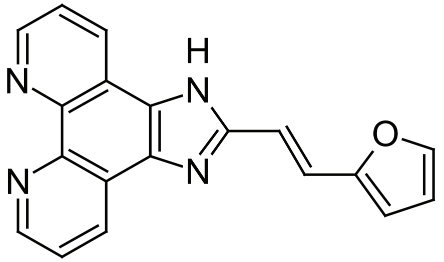

22

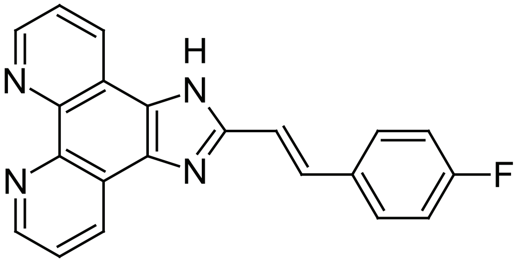

23

Figure 11. *Phenanthroline-imidazole fusion with two substituents.*

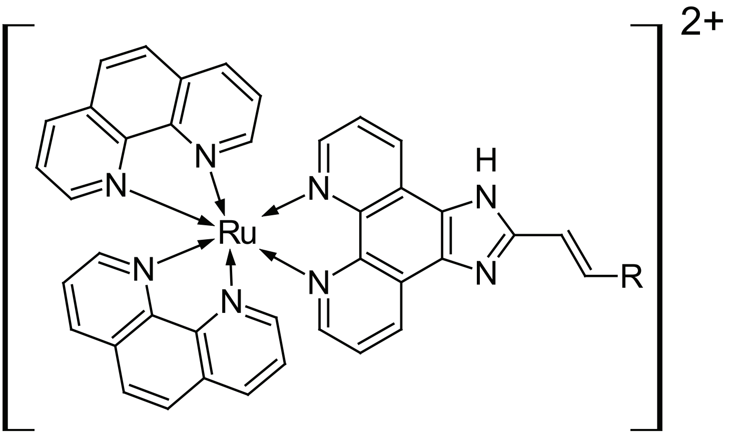

24

Figure 12. *Complexation with ruthenium(II) ion.*

Disulfiram's antitumor activity is increased by Cu(II) ions, but there is a problem that DSF decomposes in the body, losing its activity. Bis(diethyldithiocarbamatocopper(II) is the latest potent metabolite in the cells (see Figure 13) and how it serves as an antitumor agent remains a mystery until now. DDC-Cu is able to penetrate into A549's cellular membrane, and accumulate there. DDC-Cu shows promise as an agent in cancer therapy (Lu et al., 2020).

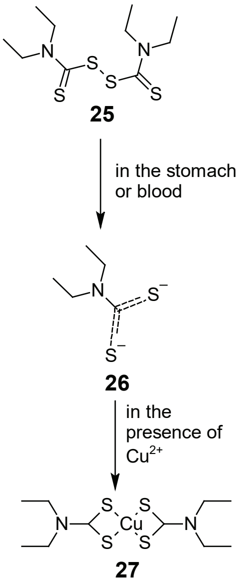

Figure 13. *Metabolism of disulfiram into diethyldithiocarbamate, a potent form.*

In the work by Mutlu Gençkal and coworkers, mixed ligand complexes with Co(II), Ni(II), and Cu(II) metal ions of synthesized using quercetin, phen, and bipy ligands (see Figure 14). Cu(II) complexes are found to be more effective than the others and complex 3 having phenanthroline and quercetin with Cu(II) ion shows promise against MDA-MB-231 and MCF-7 and cells (Mutlu Gençkal et al., 2020).

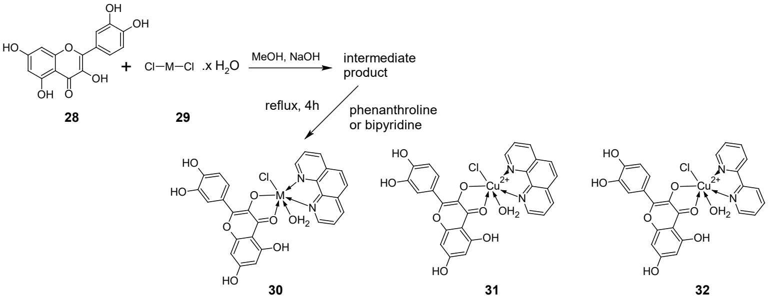

M is Cu^{2+} or Ni^{2+} for 30.

Figure 14. *Quercetin forms complexes for nickel(II) and copper(II) with two different co-ligands with different crystalline water compositions.*

Non-small-cell lung cancer (NSCLC) is most common, and small-cell lung cancer (SCLC) is very aggressive. There are not many therapeutic approaches of the latter. However, there are new molecules for treatment of SCLC and a big innovation is going on. In the study, two novel chiral Pd(II) (**33**) and Ru(II) complexes (**34**) were prepared (see Figure 15). In this study, the results showed that complex **33** (pyridine pincer structure with dichloropalladium ion) has the strongest cytotoxic effects on SCLC and NSCLC cell lines (Tokgun et al., 2020).

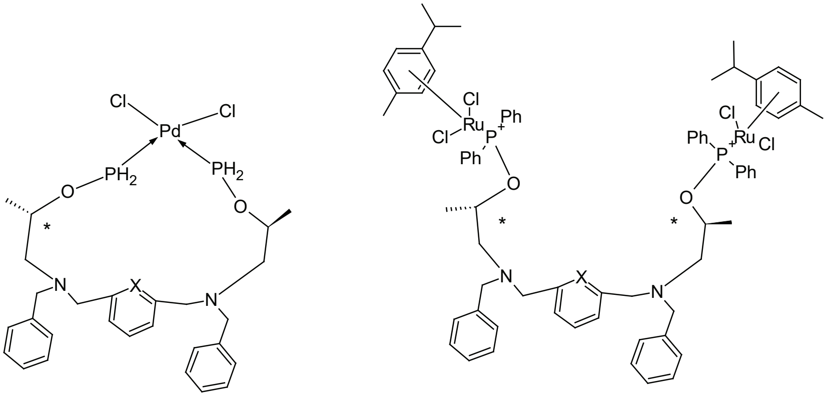

33

34

Figure 15. *Dichloropalladium and ruthenium arene complexes for the search of anticancer activity.*

Novel platinum- and pyrazole-containing complexes featuring *p*-C_6H_5F and p-CH_3, F, and Cl were reported by Querino and coworkers (**35**, see Figure 16), along with their potential antitumor activity. 4T1, B16F10, and BHK21 cell lines were treated with the compounds, and the cytotoxicity strongly increased after complexation by the metal (Querino et al., 2020).

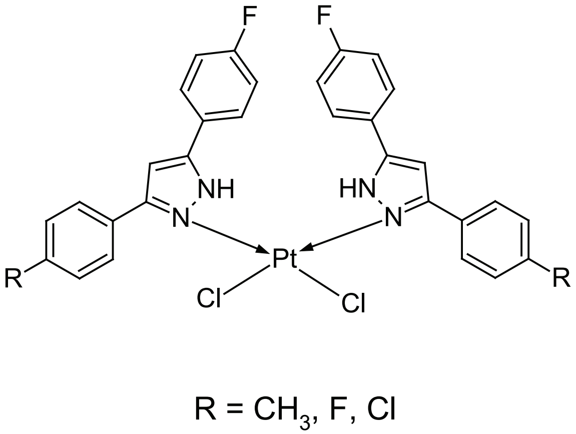

35

Figure 16. *The platinum complex obtained in the study.*

For the treatment of cancer, many approaches have been used, but chemotherapy is the most successful one, however it is toxic and selectivity is low. Less toxic and highly selective molecules are under development. The authors prepared report five copper(II) complexes (**36-40**; see Figure 17) having good biological activities. The results are important for metal anticancer drug development (Q. Zhang et al., 2020).

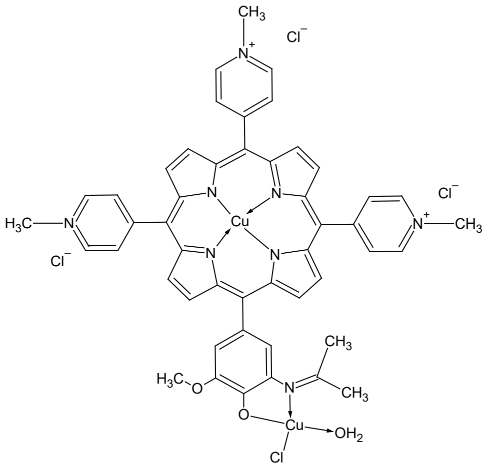

36

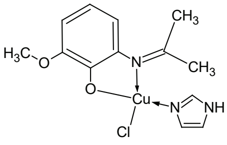

37

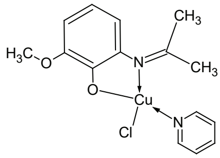

38

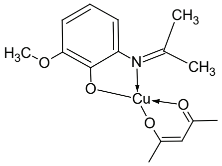

39

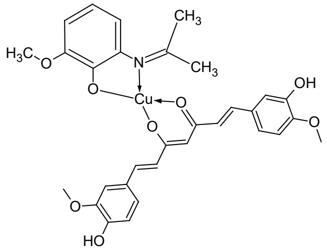

40

Figure 17. *Five complexes sharing the same porphyrin structure; only the different groups are shown in* **37**-**40**.

Schiff bases and related complexes

In a study by Raman and coworkers, four nonplatinated transition metal(II) complexes (**41**; see Figure 18) containing pyridine were investigated. The complexes (M = Cu, Co, Ni, Zn) adopted octahedral geometry. They showed increased activity against cancer cell lines and reduced toxicity against NHDF cell line. Most notably, CoL_2 showed very good activity (Raman et al., 2020).

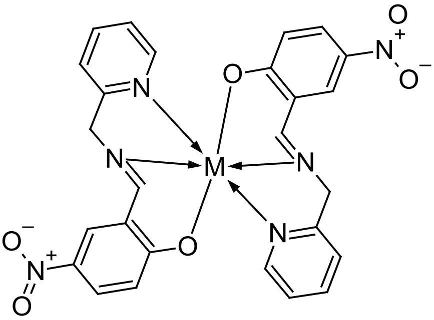

M = Co(II), Ni(II), Zn(II)

41

Figure 18. *Cobalt(II), nickel(II), and zinc(II) complexes of a Schiff's base containing salicyl aldehyde and amino pyridine molecules.*

A new Schiff base ligand's preparation and characterization containing difluorophenyl moiety (HSBL) and related metal(II) complexes [M(SBL)$_2$] (M = Cu, Ni, Pd) were reported by Amali and co-workers (**42;** see Figure 19). [Pd(SBL)$_2$] on MCF-7, complex #3 has also been suggested as a nice cytotoxic material with IC50 = 15.7 ± 0.6 µg/mL (Amali et al., 2020).

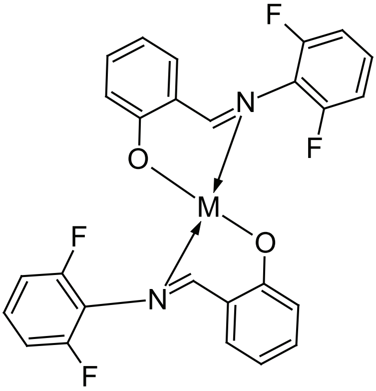

M = Cu(II), Ni(II), Pd(II)
42

Figure 19. *A new Schiff's base complex with some metal ions.*

A novel Schiff base containing aminopyrimidine and chromenone, and related complexes were synthesized in which M = Ni(II), Co(II), Cd(II), and Cu(II), (**43-47**; see Figure 20). The anticancerous activity of the ligand and related metal complexes was assayed against HEPG2 cell. It was found that Co(II) complexes featured strong cytotoxicity against 5-fluorouracil (Gaber et al., 2020).

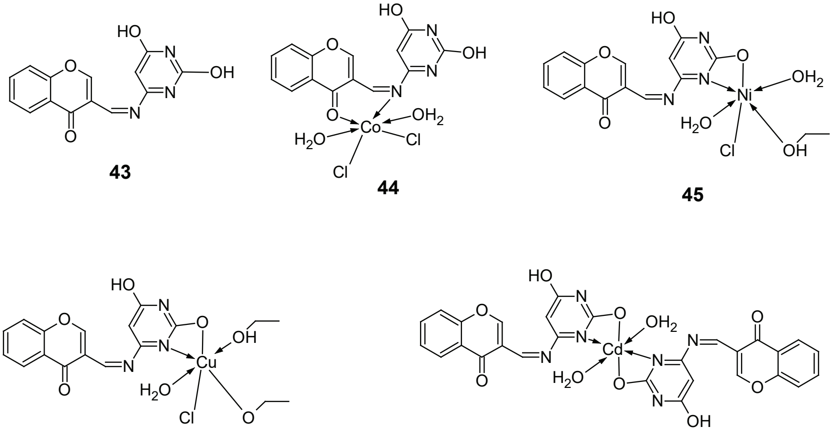

43 **44** **45** **46** **47**

Figure 20. *Co(II), Ni(II), Cu(II), and Cd(II) complexes of the new Schiff's base.*

Phenylthiosemicarbazones are reportedly new apoptosis-inducing agents. In the study by Haddadi and coworkers, copper(II) complex of phenylthiosemicarbazone (CuPTSC (**48**); see Figure 21) was investigated in KG1a. The authors concluded that Cu-PTSC may provide a new treatment of acute myeloid leukemia (Haddadi et al., 2020).

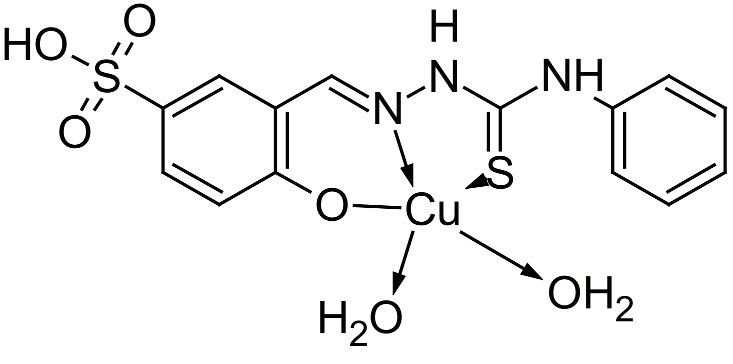

48

Figure 21. *Copper complex of a phenylthiosemicarbazone.*

Iminophosphine complexes in which the metal ions were Ni, Pd, and Pt were prepared by Kim and coworkers (see Figure 22). Evaluation of the cytotoxicities of the complexes and the ligand was performed against SK-OV-3, A549, HCT15, and SM-MEL-2. Notably, the PdL complex was the most successful one (Kim et al., 2020).

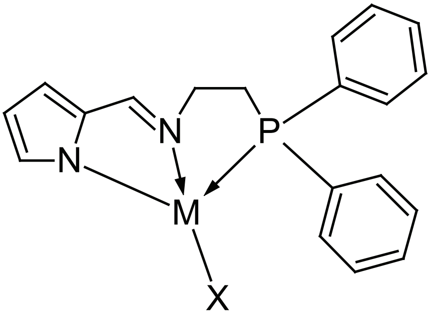

49

M = Ni, Pd, Pt; X = halide

Figure 22. *The nickel, palladium, and platinum complexes used in the study.*

Cu(II) complexes of Schiff base ligands are considered as good alternatives in chemotherapy with significant results. Here, the authors synthesized three new camphoric acid-derivatives including salen and their copper(II) complexes (see Figure 23) and their antitumoral activity against WiDr and LS1034, MCF-7 and HCC1806. Tetrachlorinated Cu(II) complex reportedly possesses a significantly more pronounced antitumor effect than the reference drugs currently in use (Pires et al., 2020).

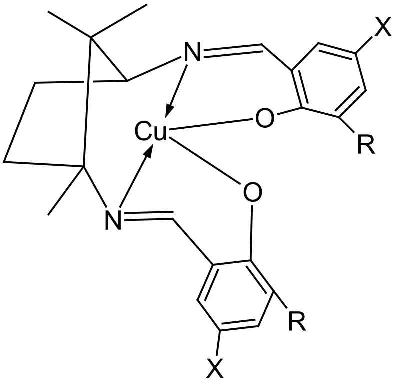

50

Figure 23. *The copper complex used in the study.*

A series of metal complexes of fluorene-2-carboxaldehyde N-substituted thiosemicarbazones (see Figure 24). In addition, a ligand and a complex displayed a better performance than HCT 116 when compared to cisplatin (Savir et al., 2020).

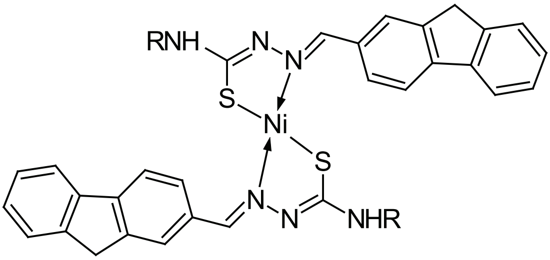

51
R = H, Me, Et

Figure 24. *Fluorene-containing Schiff base Nickel(II) complex.*

Dinuclear lanthanum, europium, and dysprosium complexes of the ligand derived from nicotinohydrazide (see Figure 25) have been synthesized. Three complexes showed promise to A549 cancer cells and less toxicity than that of cisplatin for HUVEC (Song et al., 2020).

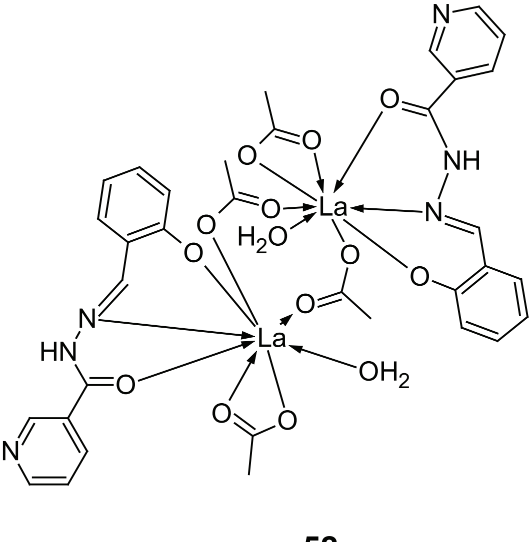

52

Figure 25. *The dinuclear lanthanum complex's structure.*

Subasi and colleagues reported four organoruthenium(II) arene complexes containing thiosemicarbazone ligands (see Figure 26). The compounds were then screened for *in vitro* anticancer properties against DLD-1, Caco-2, CCD18Co, and SW620. The authors stressed that all organoruthenium (II)-arenes could hold promise against the platinum counterparts in cancer treatment (Subasi et al., 2020).

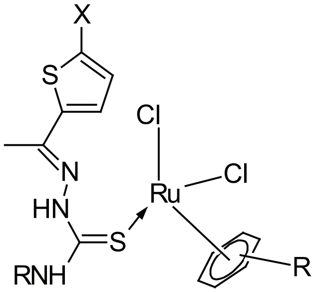

53

X = Cl, Me; R = Ph, Me

Figure 26. *Acetylthiophene thiosemicarbazone ruthenium arene complex.*

Some reduced amino-Schiff base ligands were used to synthesize ruthenium(III) complexes (see Figure 27); it is known that amino acids have more than one coordinating atoms and they increase the solubility of drugs when administered to the body. The ligands' *in vitro* cytotoxicity against A549, HeLa, and MCF-7 cells increased remarkably (Z. Zhang et al., 2020).

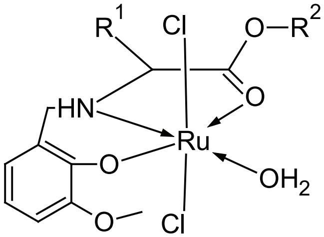

54

Figure 27. *A total of twelve ruthenium complexes were synthesized in this study.*

REFERENCES

Abyar, F., & Tabrizi, L. (2020). Experimental and theoretical investigations of novel oxidovanadium(IV) juglone complex: DNA/HSA interaction and cytotoxic activity. *Journal of Biomolecular Structure and Dynamics*, *38*(2), 474–487. https://doi.org/10.1080/07391102.2019.1580221

Amali, I. B., Kesavan, M. P., Vijayakumar, V., Rajasekaran, R., Rajesh, J., & Rajagopal, G. (2020). Biological Impacts of Metal(II) Complex–Based DNA Probes Derived from Bidentate N,O Donor Schiff Base Ligand. *Applied Biochemistry and Biotechnology*, *190*(2), 373–390. https://doi.org/10.1007/s12010-019-03110-1

Azzam, M. A., El-Boraey, H. A. L., & El-Sayed, I. E. T. (2020). Transition metal complexes of α-aminophosphonates part II: Synthesis, spectroscopic characterization, and *in vitro* anticancer activity of copper(II) complexes of α-aminophosphonates. *Phosphorus, Sulfur, and Silicon and the Related Elements*, *195*(4), 339–347. https://doi.org/10.1080/10426507.2019.1700258

Balsa, L. M., Ruiz, M. C., Santa Maria de la Parra, L., Baran, E. J., & León, I. E. (2020). Anticancer and antimetastatic activity of copper(II)-tropolone complex against human breast cancer cells, breast multicellular spheroids and mammospheres. *Journal of Inorganic Biochemistry*, *204*, 110975. https://doi.org/10.1016/j.jinorgbio.2019.110975

Bian, M., Wang, X., Sun, Y., & Liu, W. (2020). Synthesis and biological evaluation of gold(III) Schiff base complexes for the treatment of hepatocellular carcinoma through attenuating TrxR activity. *European Journal of Medicinal Chemistry*, *193*, 112234. https://doi.org/10.1016/j.ejmech.2020.112234

Chen, F., Zhang, F., Shao, D., Zhang, W., Zheng, L., Wang, W., Yang, W., Wang, Z., Chen, J., Dong, W., Xiao, F., & Wu, Y. (2020). Bioreducible and traceable Ru(III) prodrug-loaded mesoporous silica nanoparticles for sequentially targeted nonsmall cell lung cancer chemotherapy. *Applied Materials Today*, *19*, 100558. https://doi.org/10.1016/j.apmt.2020.100558

Gaber, M., El-Baradie, K., El-Wakiel, N., & Hafez, S. (2020). Synthesis and characterization studies of 3-formyl chromone Schiff base complexes and their application as antitumor, antioxidant and antimicrobial. *Applied Organometallic Chemistry*, *34*(2). https://doi.org/10.1002/aoc.5348

Haddadi, P., Mahdavi, M., & Rahbarghazi, R. (2020). Down-regulation of Bcl2 and Survivin, and up-regulation of Bax involved in copper (II) phenylthiosemicarbazone complex-induced apoptosis in leukemia stem-like KG1a cells. *Process Biochemistry*, *92*, 190–196. https://doi.org/10.1016/j.procbio.2020.01.010

Han, F., Cao, S., Ding, H., Chen, Z., Zhang, Q., & Xu, S.-D. (2020). Two mixed-ligand Cd(II)-coordination polymers: Structural diversity and antitumor activity against human osteogenic sarcoma cells. *Inorganic and Nano-Metal Chemistry*, 1–8. https://doi.org/10.1080/24701556.2020.1727516

Jiang, G.-B., Zhang, W.-Y., He, M., Gu, Y.-Y., Bai, L., Wang, Y.-J., Yi, Q.-Y., & Du, F. (2020). New ruthenium polypyridyl complexes functionalized with fluorine atom or furan: Synthesis, DNA-binding, cytotoxicity and antitumor mechanism studies. *Spectrochimica Acta Part A: Molecular and Biomolecular Spectroscopy*, *227*, 117534. https://doi.org/10.1016/j.saa.2019.117534

Jiang, W., Fan, S., Zhou, Q., Zhang, F., Kuang, D., & Tan, Y. (2020). Diversity of complexes based on p-nitrobenzoylhydrazide, benzoylformic acid and diorganotin halides or oxides self-assemble: Cytotoxicity, the induction of apoptosis in cancer cells and DNA-binding properties. *Bioorganic Chemistry*, *94*, 103402. https://doi.org/10.1016/j.bioorg.2019.103402

Kim, Y., Lee, J., Son, Y.-H., Choi, S.-U., Alam, M., & Park, S. (2020). Novel nickel(II), palladium(II), and platinum(II) complexes having a pyrrolyl-iminophosphine (PNN) pincer: Synthesis, crystal structures, and cytotoxic activity. *Journal of Inorganic Biochemistry*, *205*, 111015. https://doi.org/10.1016/j.jinorgbio.2020.111015

Lu, X., Lin, B., Xu, N., Huang, H., Wang, Y., & Lin, J.-M. (2020). Evaluation of the accumulation of disulfiram and its copper complex in A549 cells using mass spectrometry. *Talanta*, *211*, 120732. https://doi.org/10.1016/j.talanta.2020.120732

Mutlu Gençkal, H., Erkisa, M., Alper, P., Sahin, S., Ulukaya, E., & Ari, F. (2020). Mixed ligand complexes of Co(II), Ni(II) and Cu(II) with quercetin and diimine ligands: Synthesis, characterization, anti-cancer and anti-oxidant activity. *JBIC Journal of Biological Inorganic Chemistry*, *25*(1), 161–177. https://doi.org/10.1007/s00775-019-01749-z

Pires, A. S., Batista, J., Murtinho, D., Nogueira, C., Karamysheva, A., Luísa Ramos, M., Milne, B. F., Tavares, N. T., Gonçalves, J., Gonçalves, A. C., Abrantes, A. M., Soares, R., Gonçalves, T., Botelho, M. F., & Silva Serra, M. E. (2020). Synthesis, Characterization and Evaluation of the Antibacterial and Antitumor Activity of HalogenatedSalen Copper (II) Complexes derived from Camphoric Acid. *Applied Organometallic Chemistry*, *34*(5). https://doi.org/10.1002/aoc.5569

Querino, A. L. de A., Enes, K. B., Chaves, O. A., Dittz, D., Couri, M. R. C., Diniz, R., & Silva, H. (2020). Modified pyrazole platinum(II) complex can circumvent albumin and glutathione: Synthesis, structure and cytotoxic activity. *Bioorganic Chemistry*, *100*, 103936. https://doi.org/10.1016/j.bioorg.2020.103936

Raman, N., Utthra, P. P., & Chellapandi, T. (2020). Insight into the *in vitro* anticancer screening, molecular docking and biological efficiency of pyridine-based transition metal(II) complexes. *Journal of Coordination*

Chemistry, *73*(1), 103–119. https://doi.org/10.1080/00958972.2020.1716218

Savir, S., Wei, Z. J., Liew, J. W. K., Vythilingam, I., Lim, Y. A. L., Saad, H. M., Sim, K. S., & Tan, K. W. (2020). Synthesis, cytotoxicity and antimalarial activities of thiosemicarbazones and their nickel (II) complexes. *Journal of Molecular Structure*, *1211*, 128090. https://doi.org/10.1016/j.molstruc.2020.128090

Song, X.-Q., Wang, Z.-G., Wang, Y., Huang, Y.-Y., Sun, Y.-X., Ouyang, Y., Xie, C.-Z., & Xu, J.-Y. (2020). Syntheses, characterization, DNA/HSA binding ability and antitumor activities of a family of isostructural binuclear lanthanide complexes containing hydrazine Schiff base. *Journal of Biomolecular Structure and Dynamics*, *38*(3), 733–743. https://doi.org/10.1080/07391102.2019.1587511

Subasi, E., Atalay, E. B., Erdogan, D., Sen, B., Pakyapan, B., & Kayali, H. A. (2020). Synthesis and characterization of thiosemicarbazone-functionalized organoruthenium (II)-arene complexes: Investigation of antitumor characteristics in colorectal cancer cell lines. *Materials Science and Engineering: C*, *106*, 110152. https://doi.org/10.1016/j.msec.2019.110152

Tokgun, O., Karakas, D. E., Tan, S., Karagür, E. R., İnal, B., Akca, H., Durap, F., Baysal, A., & Aydemir, M. (2020). Novel ruthenium and palladium complexes as potential anticancer molecules on SCLC and NSCLC cell lines. *Chemical Papers*. https://doi.org/10.1007/s11696-020-01129-x

Zhang, Q., Zhang, Q., Li, Z., Liu, H., & Liu, J. (2020). Copper (II) complexes modified with water-soluble porphyrin and various small molecules ligand for DNA binding and potential selectivity antitumor agents. *Dyes and Pigments*, *173*, 107923. https://doi.org/10.1016/j.dyepig.2019.107923

Zhang, Z., Yang, Z., Wu, Y., Yuan, Z., Du, J., & Li, L. (2020). Reduced amino acid Schiff base containing ruthenium(III) complexes: Synthesis, characterization, DNA interaction, and in vitro cytotoxicity. *Journal of Biochemical and Molecular Toxicology*. https://doi.org/10.1002/jbt.22510

Chapter 2

DFT/TD-DFT STUDY AND NBO ANALYSIS OF CONFORMATIONAL PROPERTIES OF 2-AMINO-5-METHYLBENZOIC ACID

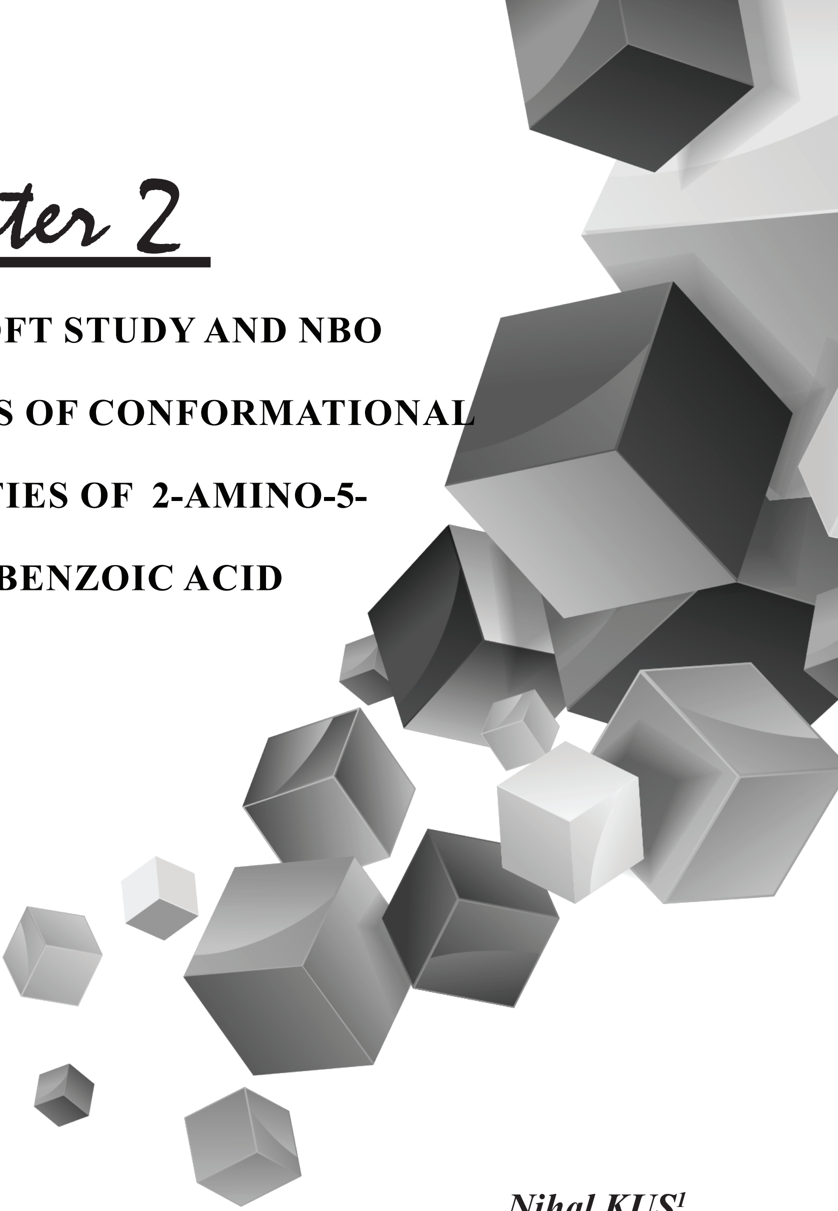

Nihal KUŞ[1]

Saliha ILICAN[2]

---

[1] Prof. Dr. Nihal KUŞ, Eskişehir Teknik Üniversitesi

[2] Prof. Dr. Saliha ILICAN, Eskişehir Teknik Üniversitesi

1. Introduction

Benzoic acid (BA) is belonging to the family of carboxylic acids naturally present in plant and also be produced by microorganisms. BA and its derivatives are frequently used in the manufacture of various cosmetics, hygiene, dyes and plastics products, antibacterial and antifungal preservatives and insect repellents [1-4]. Besides, researchers have proven that it stimulates chemical sensation by activating trigeminal nerve endings [5].

Many studies have been done on the spectral structure of BA and its derivatives. Nagaoka et al. studied 13C NMR on the hydrogen bonded dimeric of BA. At the same time, they determined the proton transfer rate, potential barriers, and the relative population of the two different configurations [6]. Vibrational spectra, normal modes and infrared spectra of six isotopic BAs were studied in the crystalline state by Kim and Machida in 1986 [7]. Stöckli et al. studied the hydrogen pair transfers in hydrogen bonded dimers of BA and its two carboxyl deuterons in solid [8]. The IR spectra of the BA crystal were simulated using the molecular dynamics method. In this simulation, frequency shifts were observed and it was noted that these shifts were due to OH stretching and OH out of plane bending modes [9]. The infrared spectra of BA (monomers and dimers) were studied in rare gases with matrix isolation technique in low temperature by Reva et al. They observed only one conformer of BA with the lowest energy in the argon matrix. [10-11].

The crystal structure of 2-amino-3-methylbenzoicacid was investigated in 1963 using the three-dimensional least squares technique. Since it was a very old study, perhaps one of the first studies done with the 2-amino-3-methylbenzoicacid molecule [12]. Samsonowicz et al. studied the IR, Raman and NMR spectra of 2, 3 and 4 aminobenzoic acids theoretically and experimentally [13]. Theoretically infrared and Raman spectra of 2-amino-3-methylbenzoic acid were studied by Yıldırım [14]. The calculations of this molecule were carried out with the B3LYP/6-311G+(2d,p) level of the density functional theory (DFT) method.

In this study, structure and conformers of 2-amino-5-methylbenzoic acid (AMBA) were investigated with computationally using DFT, time dependent DFT (TD-DFT), natural bond orbital (NBO) methods. All calculations were done with B3LYP/6-311++G(d,p) level. The normal coordinate analysis of the molecule was determined and the calculated frequencies and densities were found by performing the potential energy distribution (PED). Donor-acceptor interactions were investigated with the second order equation of the Fock matrix using the NBO method. Stabilization energies for selected NBO pairs were calculated by second order perturbation theory analysis obtained from the B3LYP/6-311++G(d,p) calculations of the Fock matrix in the NBO basis for AMBA. Excited singlet states and their energies were calculated by TD-DFT method based on second order perturbation theory. High occupied molecular orbital–low unoccupied molecular orbital (HOMO-LUMO) energy gaps were calculated and plotted. Global stability and chemical reactivity were calculated based on HOMO-LUMO energy values. Molecular electrostatic potential (MEP) surfaces were determined according to negative and positive values.

2. Materials and Methods

The calculations of the studied molecule were analyzed using Gaussian 09 program [15] including the 6-311++G(d,p) basis set of the DFT method. Gradient change corrections and three parameter hybrid density function were used in calculations (B3LYP-Becke3LeeYangParr) [16, 17]. In order to determine the conformer of AMBA, the orientations of the C–C and C–O bonds belonging to the carboxylic group were taken into consideration and the potential energy profiles were calculated. The symmetry coordinates of AMBA were determined using normal coordinate analysis as defined by Schachtshneider and Mortimer [18]. In this case, Cartesian force constants were modified into spaces of symmetry coordinates, so that the normal vibration modes and potential energy distributions (PED) [19] were calculated. These calculations were performed using the BALGA program [20].

The calculations regarding the natural bond orbital (NBO) interactions of AMBA were performed in Gaussian 09 program using the NBO 3.1 method [21-22]. Calculations of single excited states at low energy were performed with time dependent-DFT (TD-DFT) method [23-24]. The orbital interactions and stabilization energies of the AMBA molecule were determined by taking into account the Fock matrix equation accordingly the second order perturbation theory analysis [22].

3. Results and Discussion

3.1. Optimization of AMBA and Calculated Energies

Four different possible conformers of AMBA were determined theoretically according to the standard conformer definition. Fig. 1 shows these optimized conformers. From the calculated results, it was found that all conformers of AMBA belong to C1 symmetry point group. Their relative energies "(Δ[E(RB+HF-LYP)] were calculated and found to be about 11.5, 27.0 and 33.7 kJ mol^{-1}, respectively, explained in terms of prevalence in each form of different intramolecular interactions. As seen in Table 1, AMBA-I is most stable form according to relative electronic energies and also relative electronic zero point vibrational energy (Δ[E(RB+HF-LYP)+(ZPV)]; $\Delta E_{(0)}$). The relative Gibbs energies of the conformers were also calculated. As seen in Table 1, it is as in the relative electronic energy order.

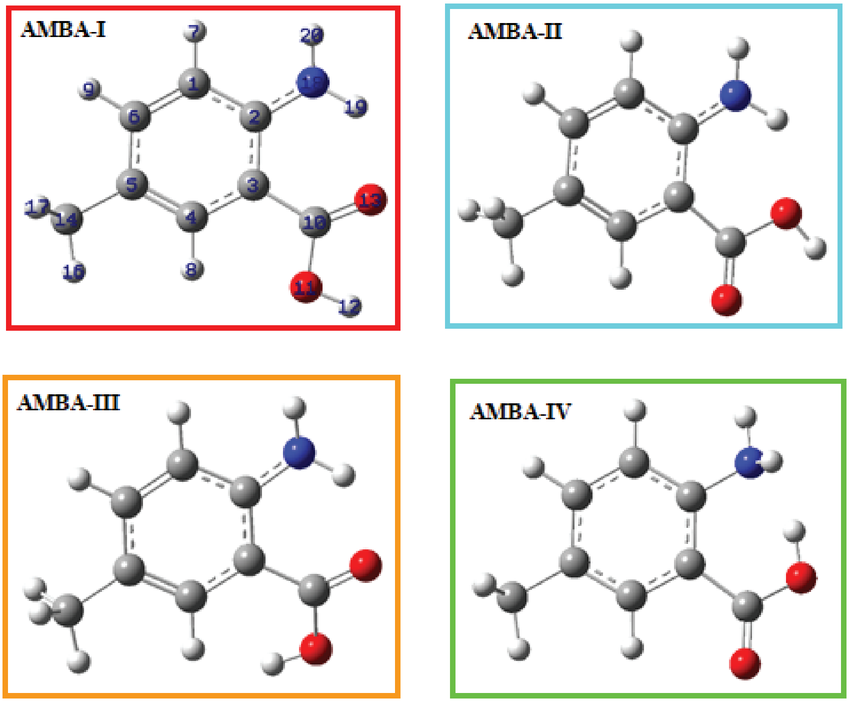

Figure 1. *Optimized conformers scheme of AMBA calculated using DFT-B3LYP/6-311++G(d,p). Atomic numbers have been adapted to AMBA-I.*

The 2nd stable conformer AMBA-II was obtained by 180 degrees rotation of the C–C bond in the carboxyl group attached to the ring of AMBA. AMBA-III was obtained by rotating the C–O bond of the second conformer by 180 degrees. The formation of all possible conformers was found by 180 degrees rotation of the C–C or C–O bonds of the carboxyl group attached to the ring. Considering the differences between ΔE and $\Delta E_{(0)}$, the energy differences (ΔE-$\Delta E_{(0)}$) of the 2nd and 3rd conformers were found to be +0.023 and +0.496 kJ mol^{-1} respectively. However, the energy difference of the 4th conformer was found to be -1.438 kJ mol^{-1}. This negative value is related to the geometry of the AMBA-IV form.

Table 1. *Calculated relative and Gibbs energies calculated from DFT method using B3LYP/6-311++G(d,p) level.*

	AMBA-I	AMBA-II	AMBA-III	AMBA-IV
ΔE(RB+HF-LYP) (kJ mol^{-1})	0	11.525	27.463	32.308
D[E(RB+HF-LYP)+(ZPV)] (kJ mol^{-1})	0	11.502	26.967	33.746
ΔG (kJ mol^{-1})	0	10.977	26.599	30.752

3.2. Potential Energy Profiles

The potential energy profile obtained by rotating the C–C and C–O bonds of the carboxylic acid group attached to the ring with angles in 15 degree steps is presented in Figure 2.

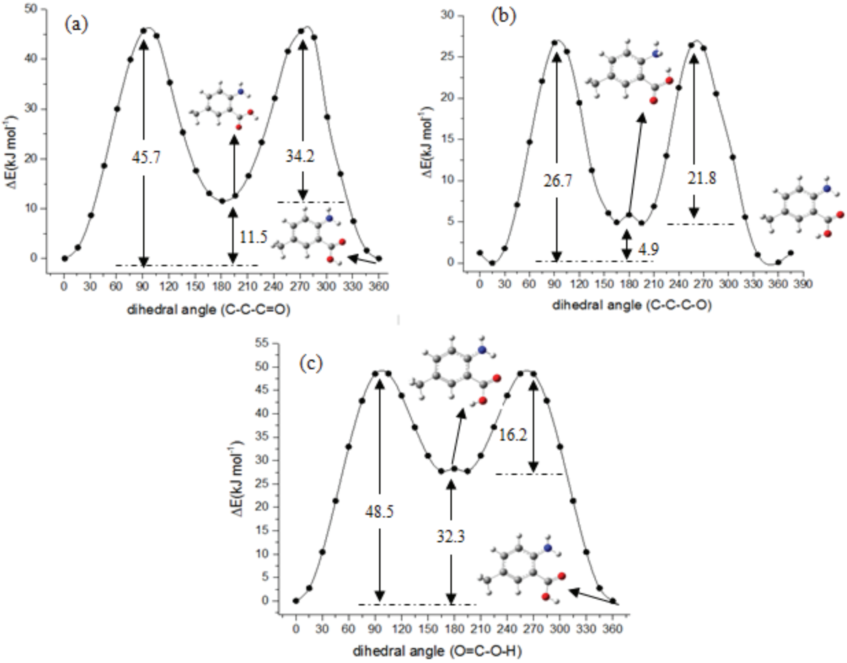

Figure 2. *Potential energy profiles calculated by B3LYP/6-311++G(d,p) level for rotation about (a, b) C–C and (c) C–O bonds in AMBA.*

The predicted barrier energy of 1st and 2nd conformers, taken from the bottom of the 1st conformer potential well, is ~45.7 kJ mol^{-1}, being only 34.2 kJmol^{-1} in the reverse direction (Fig. 2.a). Barrier energy of 3rd and 4th conformers is ~26.7 kJ mol^{-1}, being only ~21.8 kJ mol^{-1} in the reverse direction (Fig. 2.b). For 1st and 3rd conformers, barrier energy is ~48.5 kJ mol^{-1}, being only 16.2 kJ mol^{-1} in the reverse direction (Fig.

2.c). The minimum relative energies were calculated by rotating the C - C and C - O bonds belonging to the carboxylic group in 15 degree steps. Therefore, the barrier energy points were not calculated according to the exact rotation value, but according to the locations of the angle values taken. In this case, the barrier energy values may be a few kJ mol^{-1} values below or above.

3.3. Calculated IR Spectra

The vibrational frequencies of AMBA-I were calculated with B3LYP/6-311++G(d,p) level. 0.978 was used as a scale factor. 2cm^{-1} was taken as a full-width at half-maximum (fwhm) and it was calculated using the Lorentzian functions. Normal coordinate analysis (Table 2) is given by the transformation of Cartesian force constants into internal coordinates adjusted according to symmetry. In Table 2, $r_{i,j}$ is the distance between two atoms (A_i and A_j); $\beta_{i,j,k}$ is the triple angle between the vectors, A_k and A_i. $t_{i,j,k,l}$ is the dihedral angle in the plane defined by A_i, A_j and A_k. This dihedral angle is determined by the atoms A_j, A_k, A_l. $g_{i,j,k,l}$ is the angle between the vectors A_k and A_i, and this plane is defined by the atoms A_j, A_k, A_l.

The symmetry was done as defined by the internal coordinates Pulay et al. [25]. PED for values greater than 10% was calculated by using internal coordinates and is tabulated in Table 3.

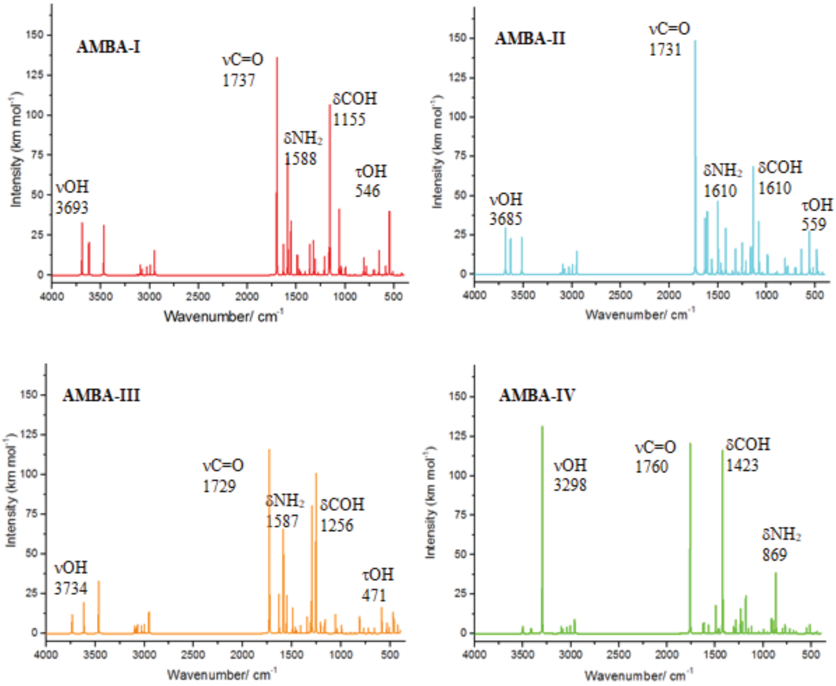

Figure 3. *Calculated infrared spectra for AMBA-I using B3LYP/6-311++G(d,p)*

level.

The vibrational spectra calculated at B3LYP/6-311++G(d,p) level for all minimum conformers were plotted (Fig. 3). The vibrations that are important and have high intensity are written on the spectrum. Note that the intensity of the OH stretching frequency of the 4th conformer at the highest minimum energy (AMBA-IV) is very strong compared to the other three conformers. It is about 419 km mol^{-1} (The intensity values plotted on the graph are relative). The reason for the high intensity can be explained as follows: The coordinates of the molecule form independent variable sets. These sets also define the intensities that vary with vibrational motion. These intensities are qualitatively associated with the bond polarities. This change in intensities can be caused by differences in electrical charges of the bound atoms and charge flows depending on the distance between atoms [26].

Table 2. *Definition of symmetry coordinates for AMBA-I (normal coordinate analysis is used)*[a].

Coordinate	**Definition** [b]	**Approximate description**
S_1	$r_{11,12}$	νOH
S_2	$r_{10,11}$	νCO
S_3	$r_{3,10}$	$\nu C\text{-}C(ac)$
S_4	$r_{2,18}$	νCN
S_5	$r_{18,20}-r_{18,19}$	$\nu NH2_{as}$
S_6	$r_{18,20}+r_{18,19}$	$\nu NH2_{s}$
S_7	$r_{4,8}$	νCH
S_8	$r_{1,7}+r_{6,9}$	$\nu CH(7/9)_{s}$
S_9	$r_{1,7}-r_{6,9}$	$\nu CH(7/9)_{as}$
S_{10}	$r_{14,15}+r_{14,16}+r_{14,17}$	$\nu CH3_{s}$
S_{11}	$2r_{14,15}-r_{14,16}-r_{14,17}$	$\nu CH3_{as'}$
S_{12}	$r_{14,15}-r_{14,17}$	$\nu CH3_{as''}$
S_{13}	$r_{10,13}$	$\nu C=O$
S_{14}	$r_{1,2}+r_{2,3}+r_{4,5+r5,}6$	νring1
S_{15}	$r_{1,2}+r_{2,3}-r_{4,5}-r_{5,6}$	νring2
S_{16}	$r_{1,2}-r_{2,3}+r_{4,5}-r_{5,6}$	νring3
S_{17}	$r_{1,2}-r_{3,4}+r_{4,5-r5,}6$	νring4
S_{18}	$r_{1,6}-_{r3,}4$	νring5
S_{19}	$r_{1,6}+r_{3,4}$	νring6
S_{20}	$r_{14,5}$	$\nu C\text{-}C(met)$

S_{21}	$\beta_{15,16,14}+\beta_{16,17,14}+\beta_{17,15,14}-\beta_{17,5,4}-\beta_{15,5,14}-\beta_{16,5,14}$	$\delta CH3_{s}$
S_{22}	$2\beta_{15,17,14}-\beta_{16,17,14}-\beta_{16,15,14}$	$\delta CH3_{as'}$
S_{23}	$\beta_{16,17,14}-\beta_{16,15,14}$	$\delta CH3_{as''}$
S_{24}	$\beta_{6,2,1}-\beta_{1,3,2}+\beta_{2,4,3}-\beta_{3,5,4}+\beta_{4,6,5}-\beta_{5,1,6}$	δring1
S_{25}	$2\beta_{6,2,1}-\beta_{1,3,2}-\beta_{2,4,3}-2\beta_{3,5,4}-\beta_{4,6,5}-\beta_{5,1,6}$	δring2
S_{26}	$\beta_{1,3,2}-\beta_{2,4,3}+\beta_{4,6,5}-\beta_{5,1,6}$	dring3
S_{27}	$\beta_{9,5,6}-\beta_{9,1,6}$	δCH9
S_{28}	$\beta_{7,6,1}-\beta_{7,2,1}$	δCH7
S_{29}	$\beta_{8,5,4}-\beta_{8,3,4}$	δCH8
S_{30}	$\beta_{20,2,18}-\beta_{19,2,18}$	wNH2
S_{31}	$\beta_{12,10,11}$	δCOH
S_{32}	$\beta_{18,1,2}-\beta_{18,3,2}$	wN-C
S_{33}	$(2\beta_{19,20,18}-\beta_{20,2,18}-\beta_{19,2,18})$	dNH2
S_{34}	$\beta_{10,2,3}-\beta_{10,4,3}$	ωC(ac)-C
S_{35}	$\beta_{14,6,5}-\beta_{14,4,5}$	ωC(met)-C
S_{36}	$\beta_{13,3,10}-\beta_{13,11,10}$	δCC=O
S_{37}	$(2\beta_{16,5,14}-\beta_{15,5,14}-\beta_{17,5,14})$	γCH3’
S_{38}	$\beta_{15,5,14}-\beta_{17,5,14}$	γCH3”
S_{39}	$(2\beta_{11,3,10}-\beta_{11,13,10}-\beta_{3,13,10})$	δ(OCO)
S_{40}	$\tau_{6,1,2,3}-\tau_{1,2,3,4}+\tau_{2,3,4,5}-\tau_{3,4,5,6}+\tau_{4,5,6,1}-\tau_{5,6,1,2}$	τCC=O
S_{41}	$\tau_{6,1,2,3}-\tau_{2,3,4,5}+\tau_{3,4,5,6}-\tau_{5,6,1,2}$	τCH3’
S_{42}	$-\tau_{6,1,2,3}+\tau_{2,3,4,5}+_{2}\tau_{1,2,3,4}-\tau_{5,6,1,2}-\tau_{3,4,5,6}+2\tau_{4,5,6,1}$	τCH3”
S_{43}	$\tau_{20,18,2,1}-\tau_{20,18,2,3}+\tau_{19,18,2,1}+\tau_{19,18,2,3}$	τC-N
S_{44}	$(\tau_{13,10,3,2}-\tau_{13,10,3,4}+\tau_{11,10,3,2}-\tau_{11,10,3,4})$	τC-C(ac)
S_{45}	$\tau_{3,10,11,12}-\tau_{13,10,11,12}$	τOH
S_{46}	$\tau_{6,5,14,15}-\tau_{6,5,14,16}+\tau_{6,5,14,17}-\tau_{4,5,14,15}+\tau_{4,5,14,16}-\tau_{4,5,14,17}$	τC-C(met)
S_{47}	$\gamma_{13,3,10,11}$	γC=O
S_{48}	$\gamma_{7,6,1,2}$	γCH7
S_{49}	$\gamma_{9,5,6,1}$	γCH9
S_{50}	$\gamma_{8,5,4,3}$	γCH8
S_{51}	$\gamma_{18,1,2,3}$	γN-C
S_{52}	$\gamma_{14,6,5,4}$	γC(met)-C
S_{53}	$\gamma_{10,2,3,4}$	γC(ac)-C
S_{54}	$\gamma_{2,20,18,19}$	γNH2

[a] *v, stretching; δ, in-plane bending;* τ, *torsion;* ω, *wagging; γ, out-of-plane; met, methyl;*

ac, acid; s, symmetric; as, asymmetric.

[b] *Normalization factors are not written; atomic numbers are given as a subscript for vibration symbols.*

Table 3. *Calculated frequencies, intensities and potential energy distribution (PED) of AMBA-I at B3LYP/6-311++G(d,p) level (normal coordinate analysis is used for PED)*[a].

Coord.[b]	Calc. Frequency[c]	Intensity	PED[d]
1	3693.5	105.5	νO-H (100)
2	3622.2	65.7	νNH2 as (92)
3	3470.8	100.6	νNH2 s (91)
4	3128.8	2.2	νCN (100)
5	3097.8	19.8	νCH (7/9)s (98)
6	3079.9	11.3	νCH (7/9)as (98)
7	3031.4	16.0	νCH3 as’ (96)
8	2996.0	20.7	νCH3 as” (100)
9	2951.9	48.3	νCH3 s (96)
10	1699.0	431.0	νC=O (70)
11	1631.1	61.6	νring6 (30) + νring1 (20)
12	1588.0	232.4	dNH2 (61) + νring3 (16)
13	1555.2	107.8	νring3 (42) + dNH2 (12) + δCH9 (10)
14	1489.9	40.3	νring2 (28) + δCH7 (23) + νCH3as” (12)
15	1468.1	11.4	δCH3 as' (75)
16	1454.8	6.9	δCH3 as'' (93)
17	1410.4	7.9	νring5 (33) + δCH3 as' (13)
18	1388.2	0.9	δCH3 s (95)
19	1361.3	60.3	νring4 (26) + νC-C (ac) (15) + δCOH (10)
20	1324.3	69.4	νring4 (19) + δCOH (15) + νCN (13)
21	1307.1	31.8	δCH9 (20) + δCH8 (17) + δCH7 (17) + wNH2 (12) + νCN (10)
22	1274.8	5.5	δCH8 (25) + νCN (18) + νring6 (15) + νring5 (10)
23	1211.6	36.6	νC-C (met) (30) + νring1 (12) + νring6 (10)
24	1165.0	50.9	νring4 (31) + νring5 (21) + δCH3s (11)
25	1155.8	339.1	δCOH (27) + δCH7 (17) + νring5 (13) + νC-C (ac) (11) + δCH8 (11)
26	1060.5	129.5	νCO (33) + wNH2 (26)
27	1043.6	2.6	γCH3” (77) + γC(met)-C (11)
28	1039.8	18.2	wNH2 (28) + dring1 (18) + νring2 (18)
29	996.4	16.6	γCH3’ (65) + νring4 (10)
30	949.4	0.4	γCH9 (70) + γCH7 (31) + γCH8 (14)
31	904.1	0.4	νring1 (24) + νC-C (met) (14) + dring3 (10)
32	900.2	2.1	γCH8 (83)

33	809.1	34.6	γCH7 (54) + γCH9 (24) + γN-C (21)
34	787.3	5.2	dring1 (21) +νCN (19) + νring2 (14) + νC-C (met) (11)
35	783.7	16.6	γC=O (60) + γC(ac)-C (14)
36	710.0	9.4	dring2 (22) + dring1 (13) + νring1 (12) + δCC=O (11) + νCO (10)
37	702.7	10.9	τCC=O (59) + γN-C (19) + γC=O (18)
38	652.0	48.8	δCC=O (40) + dring2 (25)
39	584.0	18.2	τC-N (78) + γNH2 (15)
40	546.6	129.8	τOH (75)
41	526.4	1.6	γNC(32) + τCC=O (12) + τOH (12)
42	512.2	7.4	dOCO (34) + wNC (16) + ωC(ac)-C (13)
43	466.7	0.7	dring3 (30) + dring2 (28) + νC-C(met) (14) + νring6 (12)
44	421.0	5.0	τCH3’ (70) + γC(ac)-C (15)
45	408.3	1.4	wNC (28) + δCC=O (22) + dring3 (14) + νC-C(ac) (13)
46	371.0	6.4	dring3 (22) + dOCO (21) + ωC(met)-C (15) + wNC (14) + νC-C(ac) (12)
47	323.9	12.8	ωC(met)-C (36) + wNC (18) + ωC(ac)-C (17)
48	317.9	0.3	γC(met)-C (45) + γN-C(18) + τCH3’ (11)
49	262.1	172.9	γNH2 (79) + τCN (13) + δ(OCO) (15)
50	204.8	2.4	ωC(ac)-C (51) + ωC(met)-C (22) + δ(OCO) (15)
51	156.4	11.1	γC(ac)-C (32) + γC(met)-C (19) + τCH3’ (18) + τCH3” (11)
52	116.9	6.9	τCH3” (61) + γC(ac)-C (23) + τCC=O (10)
53	74.4	0.2	τC-C(ac) (79) + τC-C(met) (17)
54	68.3	0.1	τC-C(met) (79) + τC-C(ac) (12)

[a] *Frequencies unit in cm^{-1}; calculated intensities unit in km mol^{-1};* ν, *bond stretching;* τ, *torsion;* γ *rocking;* ω, *wagging;* δ, *bending; met, methyl; ac, acid. See Table 2 for definition of symmetry coordinates.*

[b] *These numbers correspond to the definitions in Table 2.*

[c] *A scale factor of 0.978 was used for the theoretically calculated absorption bands..*

[d] *PED’s higher than 10% are included.*

3.4. Hydrogen Bonds of Conformers

In solid or liquid molecules, the vibrations of the OH or NH bonds are significantly affected by the weak hydrogen bonds formed [27]. In the conformers of AMBA, two types of hydrogen bonds are formed depending on the ring structure: C=O···H–N (AMBA-I and III), H–O···H–N (AMBA-II) or H–N···H–O (AMBA-IV) shows in Fig. 4. The hydrogen atom of the NH group and the oxygen atom of the carboxyl group were bonded with weak hydrogen bonds for AMBA-I, II and III. However, the hydrogen bond of AMBA-IV was formed between the nitrogen atom of the NH group and the hydrogen atom of the carboxyl group. Taylor et al. analyzed 1509 crystallographically independent N–H···O–C hydrogen bonds statistically. According to this analysis, the lengths of intermolecular O···H hydrogen bonds depends on the environment and nature of donors and acceptors [28]. According to this explanation, hydrogen bond lengths in the 1st and 3rd conformers were found to be almost the same (1.955 and 1.950 Å).

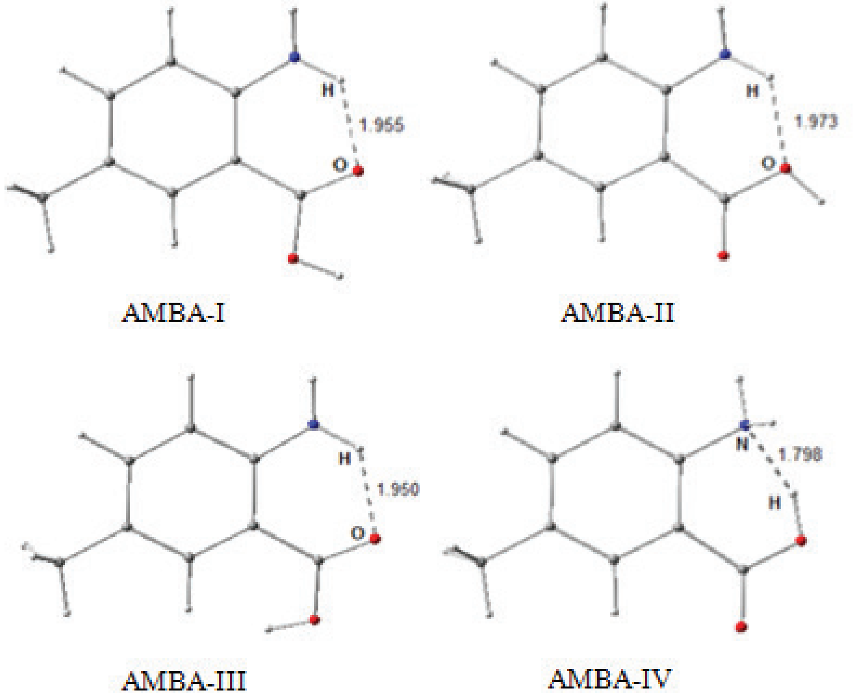

AMBA-I AMBA-II

AMBA-III AMBA-IV

Figure 4. *Hydrogen bond lengths calculated at B3LYP/311++G(d,p) level for four conformers. The unit of hydrogen bond lengths are given as Å.*

Yıldırım reported that the hydrogen bond length of dimeric 2-amino-3-methylbenzoic acid for the same atoms was found to be 2.05 Å using the DFT/B3LYP/6-311G++(2d, p) level [14]. According to the results of the calculation, the hydrogen bond lengths longer than the result we found in our current study may be due to i) the methyl group is bound to the 3rd carbon of the ring, ii) due to the dimeric structure, iii) the different DFT levels.

3.5. HOMO-LUMO Gaps

Energy difference between the highest occupied molecular orbital and the lowest unoccupied molecular orbital (HOMO-LUMO) were calculated at B3LYP/6-311++G(d,p) level for all the conformers ($\Delta E = E_{LUMO} - E_{HOMO}$) (Fig. 5). ΔE values were calculated about 4.269, 4.339, 4.331 and 5.324 eV for AMBA-I, AMBA-II, AMBA-III and AMBA-IV by DFT method with B3LYP/611++G(d,p) level, respectively.

This energy gap, also known as the electrical band gap, corresponds to the π-π* transition. It is seen that Fig. 5, HOMO spread over the ring and NH2, except for the carboxyl group, while LUMO spread all over the AMBA.

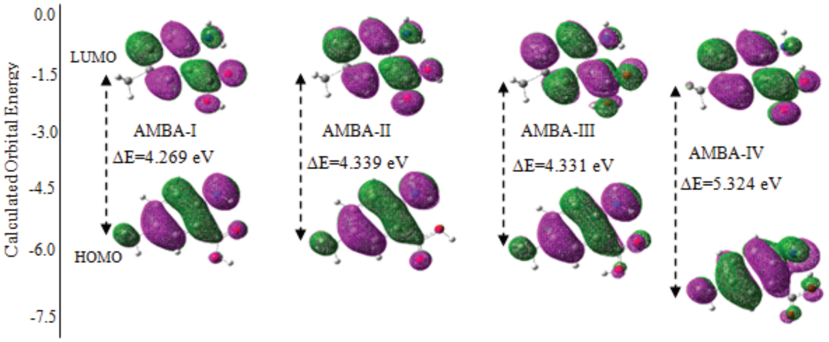

Figure 5. *HOMO-LUMO orbitals and superimposed for conformers of AMBA calculated using B3LYP/6-311++G(d,p) level.*

3.6. NBO Calculations

The orbital energies of the NBO pairs for four minimum energy conformers were calculated using the Fock matrix equation (Eq.1) and are given in Table 4.

Table 4. *The stabilization energies calculated for AMBA-I and AMBA-II using the NBO method and the Fock matrix equation derived from second order perturbation theory at the B3LYP/6-311++G(d,p) level* [a].

Conformer	***Pair Letter***	***Donor NBO (i)***	***Acceptor NBO (j)***	***E(2) (kJ mol^{-1})***	e_j-e_i	$F_{i,j}$
AMBA-I	**A**	π(C1-C6)	π*(C2-C3)	91.71	0.28	0.074
	B	π(C1-C6)	π*(C4-C5)	61.15	0.30	0.060
	C	π(C2-C3)	π*(C1-C6)	54.88	0.28	0.056
	D	π(C2-C3)	π*(C4-C5)	94.84	0.30	0.075
	E	π(C2-C3)	π*(C10-O13)	122.18	0.25	0.078
	F	π(C4-C5)	π*(C1-C6)	95.76	0.28	0.072
	G	π(C4-C5)	π*(C2-C3)	61.95	0.27	0.059
	H	LP2 O11	π*(C10-O13)	176.10	0.34	0.110
	I	LP1 O13	Ry*1 C10	61.40	1.82	0.146
	J	LP2 O13	σ*(C3-C10)	59.61	0.73	0.093
	K	LP2 O13	σ*(C10-O11)	132.80	0.61	0.126
	L	LP1 N18	π*(C2-C3)	189.23	0.28	0.107
AMBA-II	**A**	π(C1-C6)	π*(C2-C3)	91.17	0.28	0.073
	B	π(C1-C6)	π*(C4-C5)	61.32	0.31	0.060
	C	π(C2-C3)	π*(C1-C6)	56.35	0.28	0.056
	D	π(C2-C3)	π*(C4-C5)	91.79	0.30	0.074
	E	π(C2-C3)	π*(C10-O13)	109.31	0.26	0.076
	F	π(C4-C5)	π*(C1-C6)	96.85	0.28	0.072
	G	π(C4-C5)	π*(C2-C3)	63.41	0.27	0.059
	H	LP2 O11	π*(C10-O13)	157.29	0.36	0.106
	I	LP1 O13	Ry* C10	68.09	1.85	0.155
	J	LP2 O13	σ*(C3-C10)	69.43	0.71	0.099
	K	LP2 O13	σ*(C10-O11)	146.05	0.58	0.129
	L	LP1 N18	π*(C2-C3)	166.41	0.30	0.103

[a] *The atomic numbers are given in Figure 1. LP, lone-pair orbital; Ry, Rydberg orbital.*

The stabilization energy between donor and acceptor was obtained by the quadratic perturbation theory approach derived by Weinhold and Landis [22].

$$E(2) = \Delta E_{ij} = q_i \frac{F_{ij}^2}{\varepsilon_j - \varepsilon_i} \tag{1}$$

In Eq. 1, q_i represents the occupied donor orbital, e_i and e_j are the diagonal elements, and F_{ij} represents the NBO Fock matrix element. As can be seen from the Table 4, the highest stabilization energy was observed at LP1(N18)→π*(C2–C3) transitions in both conformer (AMBA-I and II) and energy values were calculated ca. 189 and 166 kJ mol^{-1}, respectively. The lowest energy transitions were observed for two conformers in the π(C2–C3)→π*(C1–C6) orbital interaction, they are about 55 and 56 kJ mol^{-1}. From the NBO calculations, if we look at the analysis of the carbonyl bond, we see that the πC=O and πC=O bond orbitals exhibit a strong polarization towards the oxygen atom. On the other hand, π*C=O and π*C=O anti-bond orbitals were found to have a strong polarization towards the carbon atom (C3) as in the acrylic acid molecule having the carboxylic group studied previously. [29].

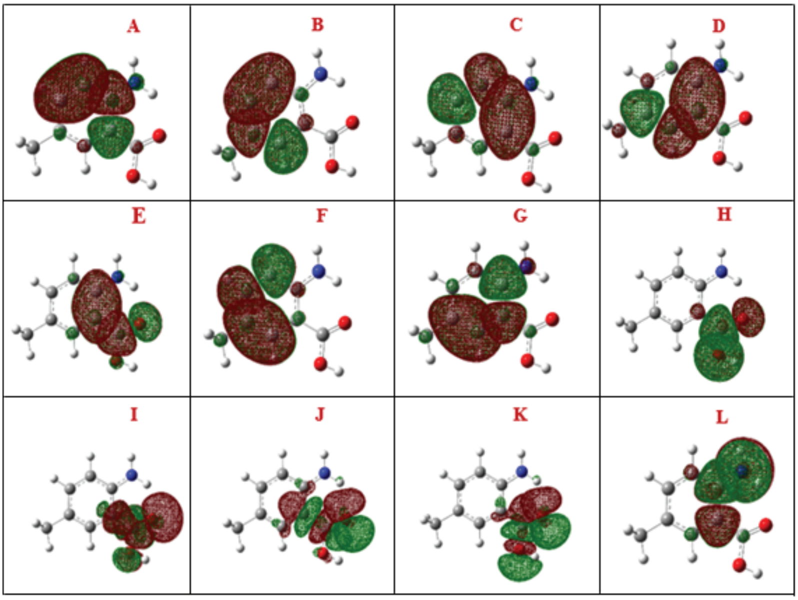

Figure 6. *Electron density surfaces for dominant orbital interactions for selected NBOs for AMBA-I calculated by B3LYP/6-311++G(d,p) level. The iso-values of electron densities are equal to 0.02e. Dark red and green colors indicate negative and positive wavefunction signs.*

The difference between the total stabilization energy of both low energy conformers (AMBA-I and II) was calculated as 24.14 kJ mol^{-1} (without zero-point correction). This result indicates that orbital interactions and other balance effects are more importance in AMBA-I in the evaluation of NBO analysis. Orbital diagrams of donor and acceptor

NBO interactions are shown with letters in Fig. 6 (AMBA-I) and Fig. 7 (AMBA-II). In these figures, orbital interactions with high stabilization energies of both conformers were determined on the same atoms. The interactions involving p orbitals are seven, including Figure 6-G. The interactions of sigma orbitals with high energies were observed in the carboxyl group. This interaction shows the ring delocalization over the carbon atom [30].

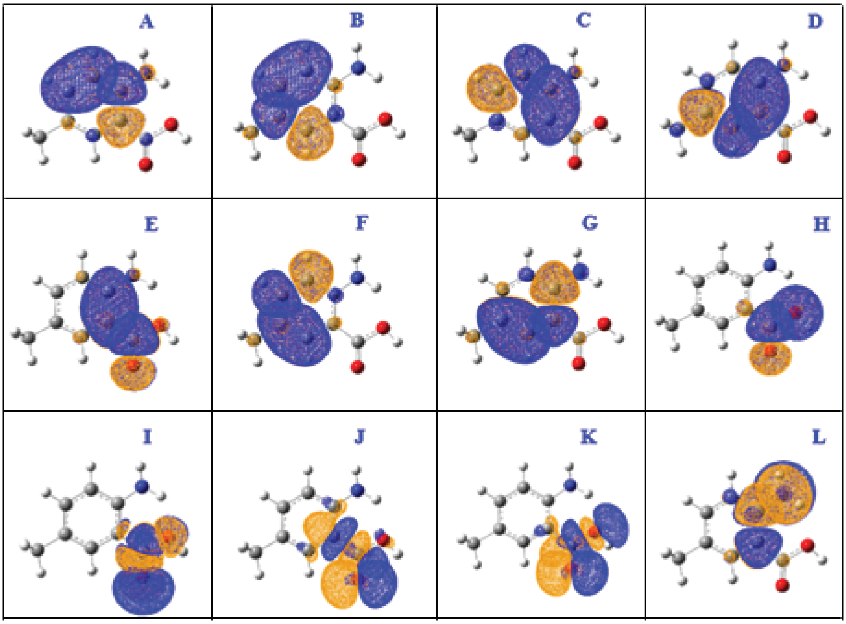

Figure 7. *Electron density surfaces for dominant orbital interactions for selected NBOs for AMBA-II calculated by B3LYP/6-311++G(d,p) level. The iso-values of electron densities are equal to 0.02e. Orange and blue colors indicate negative and positive wavefunction signs.*

3.7. Mulliken and NBO Charges

Mulliken charges calculated for all conformers in DFT/B3LYP/6-311++G(d,p) level are given in the Table 5 and Fig.8. As can be seen from the Table 5, the polarity of the O and H atoms (AMBA-I: O13···H19; AMBA-II: O11···H19; AMBA-III: O13···H19) of the first three conformers with minimum energy is lower than the polarity of the N and H12 atoms of the AMBA-IV and also because the force constant for N-H stretching is stronger [27]. Besides, the distances between the atoms are calculated as 1.955 Å (O13···H19), 1.973 Å (O11···H19), 1.950 Å (O13···H19) and 1.798 Å (N···H12). According to these calculated distances, the inter-atomic interaction of the first three conformers is less than the 4th conformer. Therefore, the intensity of the vOH stretching of the 4th conformer is higher than the others. Also, the shift of the OH vibration frequency towards the lower wavelength in the 4th conformer is due to the hypsochromic effect and is interpreted as a blue shift in the spectrum.

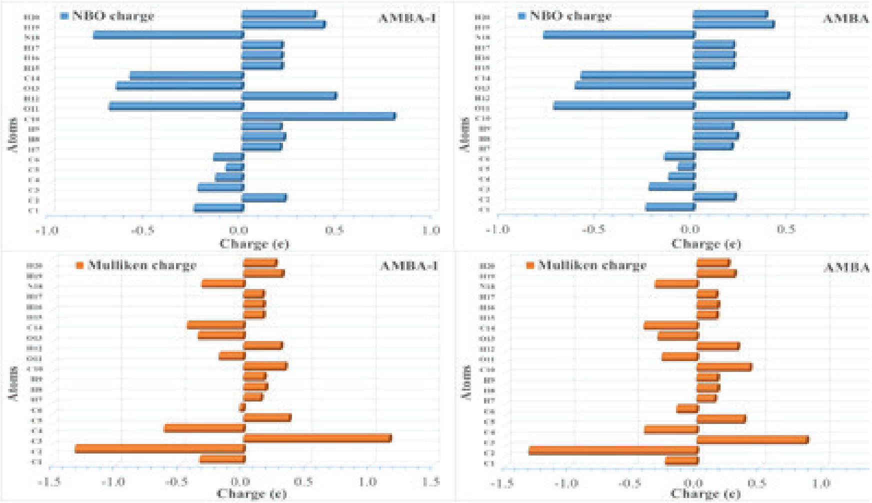

Figure 8. *The histogram of calculated natural charge and Mulliken charge for conformers of AMBA-I and AMBA-II.*

Table 5. *The calculated values of NBO and Mulliken charges for the conformers of AMBA*[a].

ATOMS	AMBA-I		AMBA-II		AMBA-III		AMBA-IV	
	NBO	Mulliken	NBO	Mulliken	NBO	Mulliken	NBO	Mulliken
C1	-0.248390	-0.342169	-0.245980	-0.245111	-0.239370	-0.432088	-0.223030	-0.457310
C2	0.223570	-1.323049	0.213680	-1.316548	0.220370	-1.186482	0.154190	-0.820744
C3	-0.228390	1.149373	-0.229720	0.861376	-0.227540	1.232466	-0.171360	1.085567
C4	-0.136180	-0.621566	-0.127850	-0.409065	-0.166520	-0.387228	-0.146030	-0.556618
C5	-0.083050	0.360865	-0.079530	0.371034	-0.077090	0.350932	-0.035230	0.326988
C6	-0.147200	-0.027933	-0.148300	-0.155924	-0.151840	0.018216	-0.169250	-0.008512
H7	0.199450	0.137876	0.198270	0.140226	0.201380	0.139320	0.204040	0.140331
H8	0.220160	0.174964	0.225310	0.163400	0.187090	0.069585	0.232070	0.181534
H9	0.201140	0.163033	0.201340	0.161104	0.203640	0.167166	0.204580	0.170240
C10	0.790580	0.328388	0.790180	0.417091	0.790090	-0.038372	0.786500	-0.031832
O11	-0.690090	-0.190807	-0.725200	-0.273700	-0.672280	-0.136673	-0.697060	-0.237681

H12	0.484140	0.294526	0.490690	0.320779	0.471900	0.230441	0.495940	0.388843
O13	-0.653320	-0.354852	-0.612790	-0.304127	-0.610890	-0.324621	-0.586530	-0.269338
C14	-0.582670	-0.440032	-0.583210	-0.412633	-0.583030	-0.417251	-0.588690	-0.442974
H15	0.206800	0.155212	0.206980	0.154404	0.209440	0.157948	0.212300	0.158262
H16	0.206360	0.156935	0.208250	0.163773	0.203850	0.156502	0.211790	0.167781
H17	0.206450	0.151501	0.206540	0.151216	0.209730	0.157410	0.212010	0.158595
N18	-0.772060	-0.327096	-0.776240	-0.327133	-0.772030	-0.307349	-0.858710	-0.525992
H19	0.424620	0.304954	0.411690	0.294931	0.425500	0.302337	0.382970	0.307846
H20	0.378090	0.249877	0.375880	0.244908	0.377580	0.247741	0.379500	0.265012

[a] *In units of e=1.60217646 × 10^{-19} C.*

3.8. TD-DFT Calculations of Electronic States

Vertical transition energies of excited singlet states were calculated in TD-DFT/B3LYP/311++G(d,p) method. These transitions include from the ground state energy state S0 to the excited energy states S1- S6 (Fig. 9). The results of AMBA-I and II calculations given in Table 6. It has been observed that S_1 has a significant oscillator strenght for all the calculated excited singlet states. In a previous study [31], we found the highest oscillator strength of 5-fluoropyrimidine-2-carboxylic acid in S_5 state and the excitation energy was around 255 nm depending on the structure of the molecule. The S_5 state corresponds to the HOMO-2→LUMO orbital interaction. In our current study, the S_5 state is calculated as the HOMO→LUMO+3 transition for both conformer (Table 6). It was found from NBO results that these excitations corresponds to the HOMO-LUMO orbital interactions. The highest oscillator power indicates a very high probability of absorption. It is also an indication that the quantum mechanical quantity, also known as the transition dipole moment, has the greatest value. Also, this means that the quantum mechanical amount, also known as the transition dipole moment, is large [32].

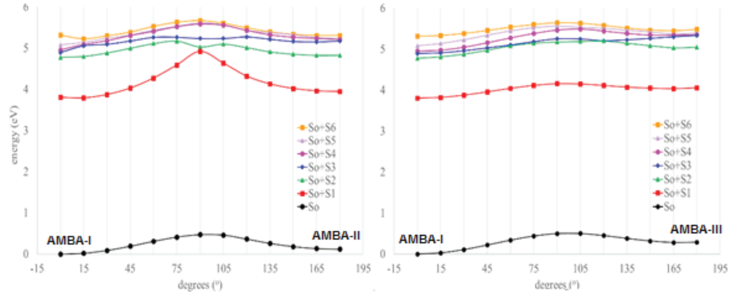

Figure 9. *TD-DFT profiles of singlets (So to S6) states of AMBA conformer I to II (left - Internal rotation about C–C) and conformer I to III (right - Internal rotation about C–O) calculated at the B3LYP/6-311++G(d,p) level of theory.*

Table 6. *Calculated wavelength of the vertical absorption (λ), oscillator strength (f) and and percentage contribution of orbital localization of the AMBA-I and AMBA-II using the TD-DFT method at B3LYP/311++G(d,p) level.*

Conformer	***State***	***Orbital localization***	***Percentage contribution***	***Oscillator strength***	***Absorption* λ (nm)**
AMBA-I	S_o				
	S_1	HOMO→LUMO	64	0.097	329.2
	S_2	HOMO→LUMO+1	68	0.002	260.6
	S_3	HOMO-2→LUMO	60	0.005	245.9
	S_4	HOMO→LUMO+2	45	0.014	245.0
	S_5	HOMO→LUMO+3	53	0.019	243.2
	S_6	HOMO→LUMO+4	65	0.003	238.8
AMBA-II	S_o				
	S_1	HOMO→LUMO	64	0.098	324.0
	S_2	HOMO→LUMO+1	69	0.003	263.5
	S_3	HOMO-2→LUMO	68	0.000	245.3
	S_4	HOMO→LUMO+2	53	0.048	243.8
	S_5	HOMO→LUMO+3	69	0.002	242.4
	S_6	HOMO→LUMO+4	67	0.005	239.0

3.9. Frontier Molecular Orbitals (FMOs)

By using the calculated HOMO and LUMO energy values, ionization potential ($IP=-E_{HOMO}$) and electron affinity ($EA=-E_{LUMO}$) were calculated. In this calculation, the equations given by Koopmans' theorem [33] are used. There isn't formal proof of this theorem in DFT, but these equations are valid.

The frontier molecular orbitals (FMOs) for AMBA were obtained using B3LYP/6-311++G(d,p) level and the equations are given below (Eqs. 2-6). These equations express the global stability and chemical reactivity of the molecule. The global reactivity descriptors such as, The *IP*, *EA*, electronegativity (χ), electronic potential (μ), hardness (η), softness (σ) and global electrophilicity index (ω) are given following equations:

$$\chi = -\frac{(E_{LUMO}+E_{HOMO})}{2} \tag{2}$$

$$\mu = \frac{(E_{LUMO}+E_{HOMO})}{2} \tag{3}$$

$$\eta = \frac{(E_{LUMO}-E_{HOMO})}{2} \tag{4}$$

$$\sigma = \frac{2}{(E_{LUMO}-E_{HOMO})} \tag{5}$$

$$\omega = \frac{(E_{LUMO}+E_{HOMO})^2}{4\,(E_{LUMO}-E_{HOMO})} \tag{6}$$

The results obtained using Eqs. 2-6 are tabulated in the Table 7.

Table 7. *IP, EA, χ, μ, η, S and ω of the conformers of AMBA calculated at DFT method using B3LYP/6-311++G(d,p).*

Conformer	*IP* (eV)	*EA* (eV)	χ (eV)	μ (eV)	η (eV)	σ (eV^{-1})	ω (eV)
AMBA-I	5.792	1.523	3.658	-3.658	2.135	0.468	3.134
AMBA-II	5.854	1.515	3.684	-3.684	2.169	0.461	3.129
AMBA-III	5.981	1.650	3.816	-3.816	2.165	0.462	3.362
AMBA-IV	6.990	1.666	4.328	-4.328	2.662	0.376	3.519

3.10. Molecular Electrostatic Potential (MEP) Surfaces

MEP is a physical property of the molecule and gives the electrical effects of the electrons and nuclei in the atom. Electrophilic and nucleophilic reactions of molecules are investigated by MEP. It is also used in the study of biologic activities [34]. MEP surfaces are indicated by color codes. The electrostatic potential equates to the total electron density. Electron-rich regions are represented by the color red and the electron-deficient regions by the color blue.

In present study, MEP onto the molecular surface was demonstrated using B3LYP/6-311++G(d,p) level. The MEP for AMBA-I on colour range from -4.1e-2 (maximum point of red) to 4.1e-2 (maximum point of blue) and for AMBA-II on colour range from -5.0e-2 (maximum point of red) to 5.0e-2 (maximum point of blue) are shown in Fig.10. The maps of two conformers showed that the positive potentials are most concentrated around the NH2 and H12 atoms while the negative potentials are most concentrated on O13 and O12 [35]. These are an expected results.

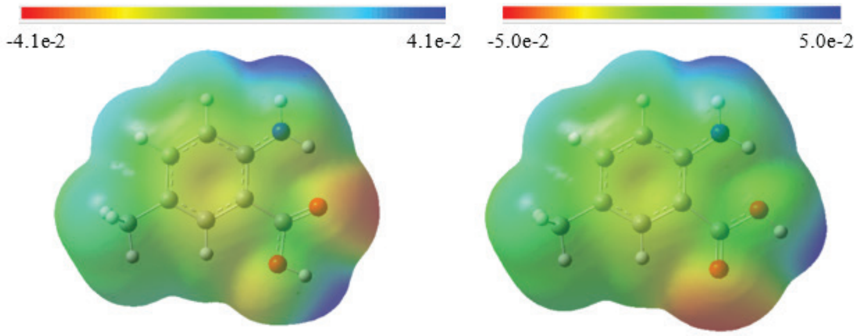

Figure 10. *Molecular electrostatic potential (MEP) surfaces for the conformers of AMBA-I and AMBA-II.*

4. Conclusion

The electronic structure of 2-Amino-5-Methylbenzoic Acid (AMBA) and its conformers are studied computationally using DFT method with B3LYP/6-311++G(d,p) level of approximation. The calculations show that AMBA has four optimized conformers as indicated from the dihedral angles. The optimized structures of the four conformers of the compound were obtained, and their zero-point corrected relative energies were found to be about 11.5, 27.0 and 33.7 kJ mol^{-1}, respectively. TD-DFT profiles of singlet and triplet states of AMBA conformer I to III and conformer I to II were calculated and plotted. As a result of the TD-DFT calculations, for HOMO-LUMO electronic absorption was predicted for AMBA-I at 329.2 nm and for AMBA-II at 324.0 nm. Stabilization energies for selected NBO (including non-Lewis extra-valence Rydberg orbitals) pairs were calculated by second order perturbation theory analysis obtained from the B3LYP/6-311++G(d,p) calculations of the Fock matrix in the NBO basis for AMBA. From the NBO calculations, the atoms with the most orbital interactions were determined and it was found that the high stabilization energy was LP1 (N18)→π*(C2–C3) transition. In order to analyse the donor-acceptor interactions in the NBO basis for AMBA, the second-order Fock matrix was used. Mapping of the electrostatic potential onto the AMBA-I and II surface indicated. The global reactivity descriptors were calculated for all conformers.

REFERENCES

[1] Olmo, A., Calzada, J., Nuñez, M. (2015). Benzoic Acid and Its Derivatives as Naturally Occurring Compounds in Foods and as Additives: Uses, Exposure and Controversy. *Crit. Rev. Food Sci. Nutr.* 57, 3084–3103.

[2] Widhalm, J.R., Dudareva, N. (2015). A Familiar Ring to It: Biosynthesis of Plant Benzoic Acids. *Mol. Plant* 8, 83–97.

[3] Joye, I.J. (2019). *Acids and Bases in Food.* In P. Varelis, L. Melton, F. Shahidi (Eds.) Encyclopedia of Food Chemistry (1–9). doi:10.1016/B978-0-08-100596-5.21582-5.

[4] Green, B.G., Lawless, H.T. (1991). *The psychophysics of somatosensory chemoreception in the nose and mouth.* In Getchell, T.V., Bartoshuk, L., Doty, R.L., Snow, J.B. (Eds.) Smell and Taste in Health and Disease (235–253). New York: Raven Press.

[5] Peleg, H., Noble, A.C. (1995). Perceptual properties of benzoic acid derivatives. *Chem. Senses* 20, 393–400.

[6] Nagaoka, S., Terao, T., Imashiro, F., Saika, A., Hirota, N., Hayashi, S. (1981). A study on the proton transfer in the benzoic acid dimer by 13C high-resolution solid-state NMR and proton T1 measurements. *Chem. Phys. Let.* 80, 580–584.

[7] Kim, Y, Machida, K. (1986). Vibrational spectra, normal vibrations and infrared intensities of six isotopic benzoic acids. *Spectrochim. Acta A* 42, 881–889.

[8] Stöckli, A., Meier, B.H., Kreis, R., Meyer, R., Ernst, R.R. (1990). Hydrogen bond dynamics in isotopically substituted benzoic acid dimers. *J. Chem. Phys.* 93, 1502–1520.

[9] Nakamura, R., Machida, K., Oobatake, M., Hayashi, S. (1988). Molecular dynamics simulation of infrared spectra and average structure of benzoic acid crystal. *Mol. Phys*. 64, 215–227.

[10] Reva, I.D., Stepanian, S.G. (1995). An infrared study on matrix-isolated benzoic acid, *J. Mol. Struct.* 349, 337–340.

[11] Stepanian, S.G., Reva, I.D., Radchenko, E.D., Sheina, G.G. (1996). Infrared spectra of benzoic acid monomers and dimers in argon matrix. *Vib. Spectrosc*. 11, 123–133.

[12] Brown, G.M., Marsh, R.E. (1963). The crystal and molecular structure of 2-amino-3-methylbenzoic acid. *Acta Cryst.* 16, 191–202

[13] Samsonowicz, M., Hrynaszkiewicz, T., Świsłocka, R., Regulska, E., Lewandowski, W. (2005). Experimental and theoretical IR, Raman, NMR spectra of 2-, 3- and 4-aminobenzoic acids. *J. Mol. Struct.* 744, 345–352.

[14] Yıldırım, M.H. (2018). Infrared and NMR Spectral Analyses and Computational Studies of 2-amino-3-methylbenzoic Acid. *Bilge Int. J. Sci. Technol. Res.* 2, 74–82.

[15] Frisch, M.J., et al. (2009). Gaussian 09, Revision A.0.2, Gaussian, Inc., Wallingford CT.

[16] Becke, A.D. (1988). Density-functional exchange-energy approximation with correct asymptotic behavior. *Phys. Rev. A* 38, 3098–3100.

[17] Lee, C.T., Yang, W.T., Parr, R.G. (1988). Development of the Colic-Salvetti correlation-energy formula into a functional of the electron density. *Phys. Rev. B* 37, 785–789.

[18] Schachtschneider, J.H., Mortimer, F.S. (1965). *Vibrational analysis of polyatomic molecules. VI: FORTRAN IV programs for solving the vibrational secular equation and for the least-squares refinement of force constants.* Houston, USA: Shell Development Co.

[19] Keresztury, G., G. Jalsovszky, (1971), An alternative calculation of vibrational potential energy distribution. *J. Mol. Struct.* 10, 304–305.

[20] Lapinski, L., Nowak, M.J. (1970). *BALGA–Computer Program for PED Calculations*, Warsaw, Poland: Institute of Physics, Polish Academy of Sciences.

[21] Reed, A.E., Curtiss, L.A., Weinhold, F. (1988). Intermolecular interactions from a natural bond orbital, donor-acceptor viewpoint. *Chem. Rev.* 88, 899–926.

[22] Weinhold, F., Landis, C.R. (2005). *Valency and Bonding. A Natural Bond Orbital Donor-Acceptor Perspective*, New York: Cambridge University Press.

[23] Bauernschmitt, R., Ahlrichs, R. (1996). Treatment of Electronic Excitations Within the Adiabatic Approximation of Time Dependent Density Functional Theory. *Chem. Phys. Lett.* 256, 454−464.

[24] Stratmann, R.E., Scuseria, G.E., Frisch, M.J. (1998). An Efficient Implementation of Time-Dependent Density-Functional Theory for the Calculation of Excitation Energies of Large Molecules. *J. Chem. Phys.* 109, 8218−8224.

[25] Pulay, P., Fogarasi, G., Pang, F., Boggs, J.E. (1979). Systematic ab initio gradient calculation of molecular geometries, force constants, and dipole moment derivatives. *J. Am. Chem. Soc.* 101, 2550–2560.

[26] Galabov, B., Dudev, T. (1988). Bond Properties and Molecular Conformation from Vibrational Intensity Analysis, *Croat. Chem. Acta*, 61, 569–587.

[27] Richards, R.E. (1948). The force constants of some OH and NH links, *Trans. Faraday Soc.* 44, 40–44.

[28] Taylor, R., Kennard, O., Versichel, W. (1984). The Geometry of the N-H...O--C Hydrogen Bond. 3. Hydrogen-Bond Distances and Angles, *Acta Cryst. B* 40, 280–288.

[29] Kuş, N. Ai, Y.-J., Fang, W.-H., Fausto, R. (2011). Photorotamerization of matrix-isolated acrylic acid revisited, *J. Chem. Phys.* 134, 154306.

[30] Kus, N., Reva, I., Fausto, R. (2010). Photoisomerization and Photochemistry of Matrix-Isolated 3-Furaldehyde. *J. Phys. Chem. A* 114, 12427–12436.

[31] Kuş, N., Ilican, S. (2020). Cis ve Trans Formundaki 5-Floropirimidin-2-Karboksilik Asit Molekülünün DFT/TD-DFT ve NBO Analizleri, *BEÜ Fen Bilimleri Dergisi* 9, 120–129.

[32] Hilborn, R.C. (1982). Einstein coefficients, cross sections, f values, dipole moments, and all that. *Am. J. Phys.* 50, 982–986.

[33] Koopmans, T. (1934). Über die Zuordnung von Wellenfunktionen und Eigenwerten zu den Einzelnen Elektronen Eines Atoms. *Physica* 1, 104–113.

[34] Fleming I. (1976). *Frontier Orbitals and Organic Chemical Reactions*, New York: John Wiley and Sons.

[35] Sheeraz A.B., Shabbir A. (2016). Quantum chemical and spectroscopic investigations of4-Hydroxy-7-metFhyl-1,8-naphthyridine-3-carboxylic acid, *J. Theor. Comput. Chem.* 15, 1650042.

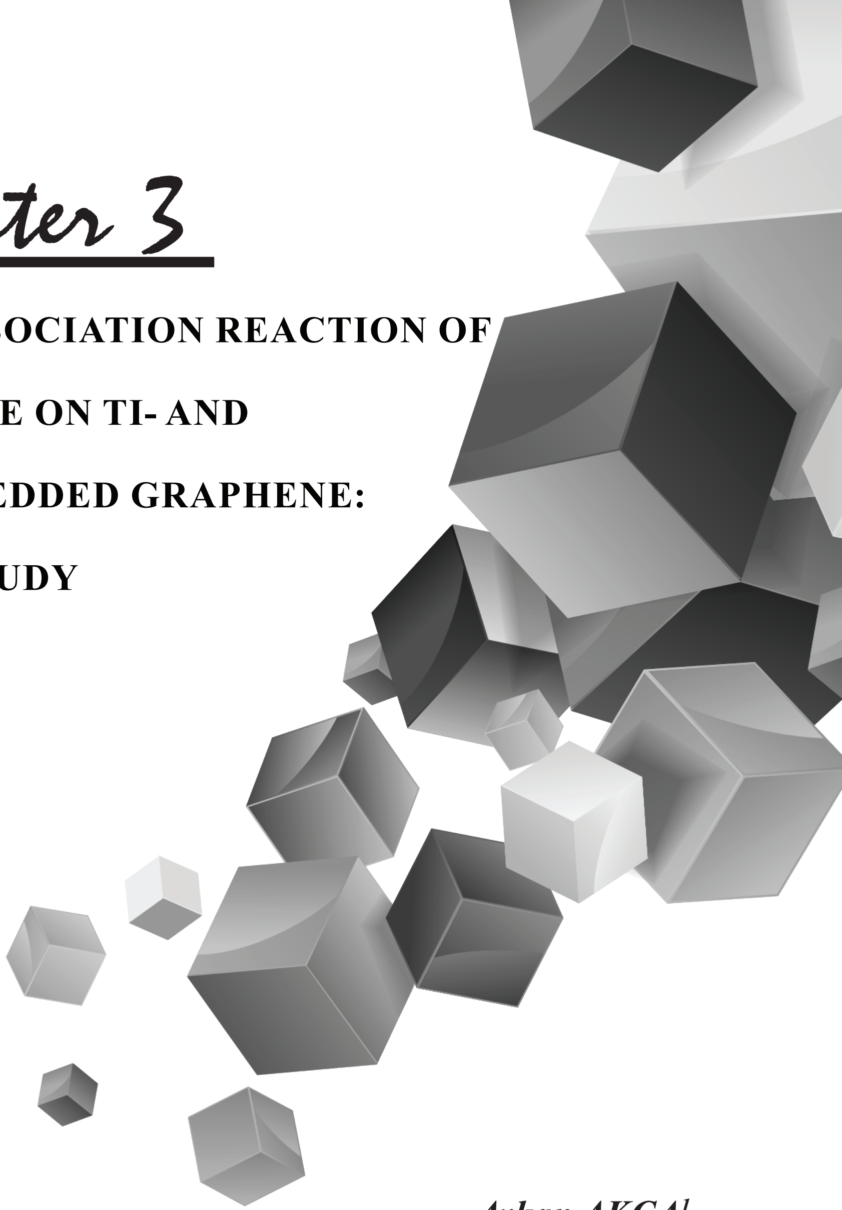

Chapter 3

THE DISSOCIATION REACTION OF METHANE ON TI- AND CO-EMBEDDED GRAPHENE: A DFT STUDY

Aykan AKÇA[1]
İrem ÖNER ALP[2]

---

[1] Department of Physics, Sabire Yazıcı Faculty of Science and Letters, Aksaray University, Aksaray, TURKEY (ORCID: 0000-0002-2517-765X)

[2] Department of Physics, Sciences Faculty, Gazi University, Ankara, TURKEY (ORCID: 0000-0002-6937-7864)

1. INTRODUCTION

Methane (CH_4) has been frequently used in hydrogen production and chemical synthesis processes (Zhang et al., 2012; He et al., 2014; Pucker et al., 2012). It is quite stable at room temperature which makes decomposition of CH_4 rather difficult. Therefore, the number of studies on hydrogen production from methane molecules by the help of a catalyzer have grown rapidly in recent years. Catalyzers have drawn attention due to their large catalytic activities and structural stabilities. However, CHx (x=0-4) type carbon structures arising during a chemical reaction cause a loss of catalyzer activity due to binding onto the active regions on the catalyzer surface. Thus, catalyzers composed of two other transition metals have been used to overcome this difficulty. The NiCu, NiCo, NiPt, NiAu, NiSn, and NiPd alloys have been synthesized experimentally up to date and the NiCo and NiRh catalyzers exhibits high catalytic activity on the role of decomposing carbon structures among these alloys (Li et al., 2013).

Many different catalysts have been used for the CH_4 decomposition reaction theoretically besides experimental studies. Some of them can be listed as Ni/γ-Al2O3 (Li et al., 2013), pure and gold-alloyed Ni(111) (Kratzer et al., 1996), NiPd (Li et al., 2012), NiM(111) (M=Co,Rh,Ir) (Li et al.,2013), NiCu (Li et al., 2012), NiCo (Li et al., 2011), Ni, Pd, Pt, and Cu (Liao et al., 1997), Ni (111) and Ru (0001) (Egeberg et al., 2002). The CH_4 decompositions on Cu(111) and Ni (111) surfaces were investigated along with oxygen doped catalyzer on these days and it has been revealed that Cu(111) exhibits higher catalytic activity compared to the other surfaces (Balbuena et al., 2020). In an other study, the effect of Pd-Pt / γ-Al2O3 catalyzer on CH_4 decomposition reaction was analyzed. It has been shown that the reaction activity increases depending on the Pd-Pt ratio of the catalyst (Cehn et al.2020).

The graphene-based materials have superior thermal, electrical and mechanical capabilities and are also used extensively in chemical sensor and catalyzer research (Wang et al., 2014). On the other hand, there have been only a few studies about the effect of graphene-based catalyzers on CH_4 decomposition reaction up to now. In the present paper, the CH_4 decomposition reactions on Ti- and Co-embedded graphene surfaces have been presented and the catalytic activity of the surfaces was addressed. Initially, the reaction mechanism of CH_x (x = 0-4) type compounds and the binding energies of the H atom on Ti- and Co-embedded graphene were calculated. Later on, the required activation and reaction energies for each reaction step were calculated using the climbing image nudged elastic band method (CINEB). Finally, the relative energy diagrams of the reaction steps were obtained on both surfaces and the results were compared with each other.

2. MATERIALS and METHODS

2.1. Computational Method

All the computations were performed via density functional theory (DFT) based Quantum Espresso 6.3 software package (Giannozzi et al., 2009; Giannozzi et al., 2017). The projector augmented wave (PAW) potential was utilized for electronic structure interaction calculations (Kresse et al., 1999) and GGA-PBE was chosen as the exchange correlation functional (Monkhorst et al., 1976). The plane wave expansions and kinetic cut-off energy terms were chosen as 70 Ry and 700 Ry, respectively, during the whole computation stage. The term Grimme-D2 was defined within the system to be able to observe van der Waals and other relatively weaker interactions (Grimme et al., 2010). The force and energy convergence criteria were accepted as $1x10^{-5}$ Ry/atom and $1x10^{-6}$ Ry/atom, respectively. 4×4×1 k-points were used for surface calculations and a cubic frame with a lattice parameter of 20 Å was chosen for gas phase optimizations of atomic and molecular structures.

2.2. Surface Modelling

A 4×4 graphene layer consisting of 32 carbon (C) atoms was constructed for Ti (Titanium) and Co (Cobalt) embedded graphene surface modelling. The distance between the nearest C atoms was found to be 1.42 Å after the optimization of this layer and this value is exactly compatible with that of the literature (Yang et al., 2009). Both surface models are given in Figure 1.

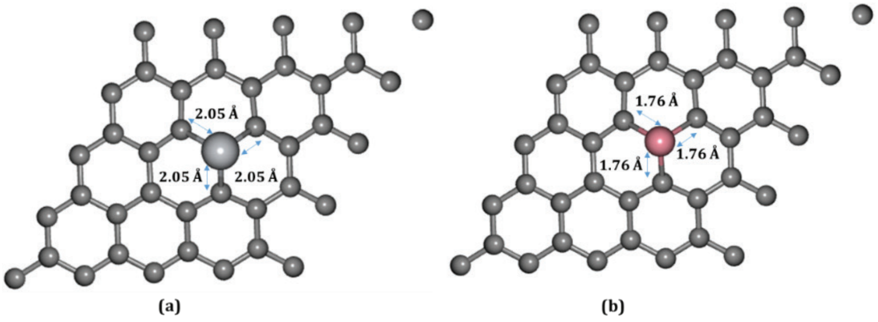

Figure 1. Top view of the (a) Ti-embedded and (b) Co-embedded graphene surfaces (the colors dark grey, light grey and pink represent carbon, titanium and cobalt atoms, respectively).

A vacuum spacing of 16 Å was constructed to prevent undesired interactions between intermediate layers since the supercell has a geometrical structure such that it repeats itself through all the three dimensions. Later on, one of the carbon atoms located in the center of the supercell was removed and replaced by Ti (Co for the other surface model).

The bond lengths between Ti/Co and the nearest C atom after the surface modelling optimizations were found to be 2.05 Å and 1.76 Å, respectively. In addition, the total magnetic moment values of Ti and Co embedded graphene surfaces were computed as 0 and 0.93 μB, respectively. These values are so close to the data computed by Krasheninnikov et al. (Krasheninnikov et al., 2009). The binding energies (E_b) of atomic and molecular structures on the graphene surface were calculated via Equation 1;

$$E_b = E_{\text{graphene+Ti/Co+atom/molecule}} - E_{\text{graphene+Ti/Co}} - E_{\text{atom/molecule}} \tag{1}$$

where, $E_{graphene+Ti/Co+atom/molecule}$ denotes the total energy of atomic or molecular structures interacting with the Ti- or Co-embedded graphene. $E_{graphene+Ti/Co}$ is the total energy of the Ti/Co embedded graphene and $E_{atom/molecule}$ represents the gas phase of the atomic or molecular structures.

3. RESULTS and DISCUSSION

3.1. The Binding Mechanism of CH_4 Molecule

CH_4 molecule is generally bonded to the transition metal and metal embedded graphene surfaces through van der Waals interactions since its structural stability. Such interactions, also called physical interactions, have a low binding energy (Roy et al., 2018). The most stable geometries of CH_4 molecule binding onto Ti- and Co-embedded graphene surface are shown in Figure 2. The H atoms in the figure are labeled as Hn (n = 1 → 4).

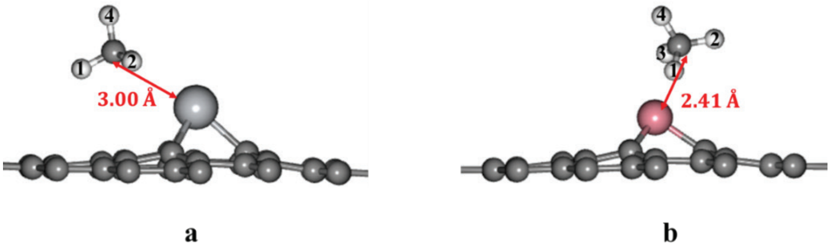

Figure 2. The optimized geometries of CH_4 molecule binding onto the (a) Ti-embedded and (b) Co-embedded graphene surface (The light grey ball: titanium atom, the dark grey balls: carbon atoms, the white balls: hydrogen atoms, and the pink ball: cobalt atom).

The binding energies of CH_4 molecule onto Ti- and Co-embedded graphene surfaces were calculated as -0.03 eV and +0.08 eV, respectively. This result obtained for the Co-Embedded graphene surface is very close to the value found in the previous study of Tang et al. [29]. The optimized bond lengths of CH_4 on Ti- and Co- embedded graphene surfaces and in the gas phase are given in Table 1.

Table1. The optimized bond lengths of the CH_4 molecule on both surfaces and in the gas phase (All the bond lengths given are written using the Angstrom (Å) measurement unit).

Bond type	Ti-embedded graphene	Co-embedded graphene	Gas phase
C-H1	1.09	1.11	1.10
C-H2	1.10	1.10	1.10
C-H3	1.10	1.12	1.10
C-H4	1.09	1.10	1.10

As can be clearly seen in Table 1, the C-H1 and C-H4 bonds have been shortened, the C-H2 and C-H3 bond lengths have been unchanged for the Ti-embedded graphene surface. Otherwise, the Co-embedded graphene surface caused elongation of the C-H1 bond by 0.01 Å and the C-H3 bond by 0.02 Å, whereas C-H2 and C-H4 bonds have remained the same.

3.2. The Binding Mechanism of CH_3 Molecule

The CH_3 molecule is held by the both metal atoms and surfaces. The optimized bonding geometries on both surfaces are presented in Figure 3. The CH_3 molecule has stable geometries at a distance of 2.24 Å from the Ti atom and 1.99 Å from the Co atom.

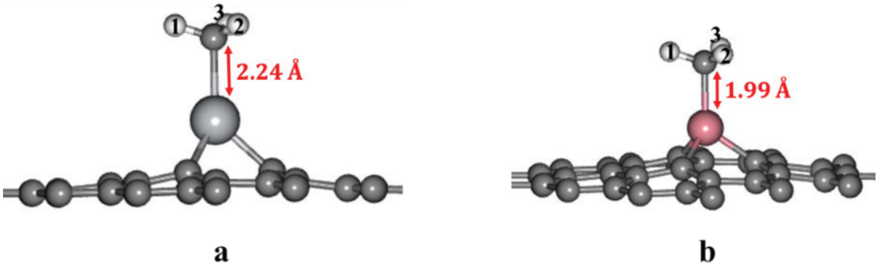

Figure 3. The optimized geometries of CH_3 molecule binding onto the (a) Ti-embedded and (b) Co-embedded graphene surface (The light grey ball: titanium atom, the dark grey balls: carbon atoms, the white balls: hydrogen atoms, and the pink ball: cobalt atom).

According to our calculations, the binding energy of the CH_3 molecule onto Ti- and Co-embedded graphene surfaces was obtained as -1.31 eV and -1.53 eV. The optimized bond lengths on both surfaces and in the gas phase are given in Table 2.

Table2. The optimized bond lengths of the CH_3 molecule on both surfaces and in the gas phase (All the bond lengths given are written using the Angstrom (Å) measurement unit).

Bond type	Ti-embedded graphene	Co-embedded graphene	Gas phase
C-H1	1.10	1.10	1.08
C-H2	1.10	1.10	1.08
C-H3	1.10	1.10	1.08

It can be seen that all bonds are elongated by 0.02 Å on both surfaces compared to the gas phase.

3.3. The Binding Mechanism of CH_2 Molecule

The optimized bonding geometries of CH_2 molecule on Ti- and Co-embedded graphene surfaces are shown in Figure 4. Considering these geometries, CH_2 interacts with the metal atoms more strongly compared to the CH_3 molecule due to the shorter bond lengths.

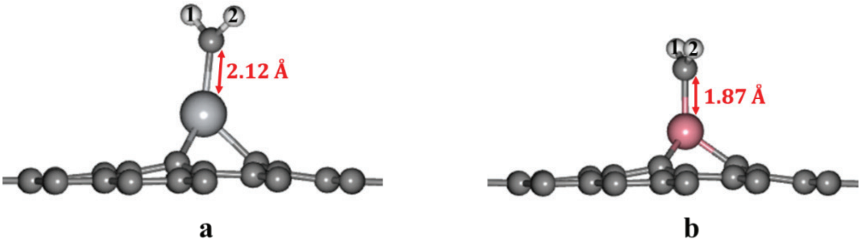

Figure 4. The optimized geometries of CH_2 molecule binding onto the (a) Ti-embedded and (b) Co-embedded graphene surface (The light grey ball: titanium atom, the dark grey balls: carbon atoms, the white balls: hydrogen atoms, and the pink ball: cobalt atom).

The binding energies of the CH_2 molecule were found to be -2.13 eV and -2.44 eV, respectively, onto Ti- and Co-embedded graphene surfaces. The optimized bond lengths between CH_2-Ti and CH_2-Co were 2.12 Å and 1.87 Å, respectively. The optimized bond lengths of CH_2 on both these surfaces and in the gas phase are given in Table 3.

Table 3. The optimized bond lengths of the CH_2 molecule on both surfaces and in the gas phase (All the bond lengths given are written using the Angstrom (Å) measurement unit).

Bond type	Ti-embedded graphene	Co-embedded graphene	Gas phase
C-H1	1.097	1.098	1.08
C-H2	1.097	1.098	1.08

As it is seen from Table 3, the C-H1 ve C-H2 bond lengths increase on the both surfaces compared to the gas phase.

3.4. The Binding Mechanism of CH Molecule

The optimized bonding geometries of the CH molecule on both surfaces are shown in Figure 5. In this geometry, CH prefers to be bonded to the Ti and Co transition metals in an almost upright position.

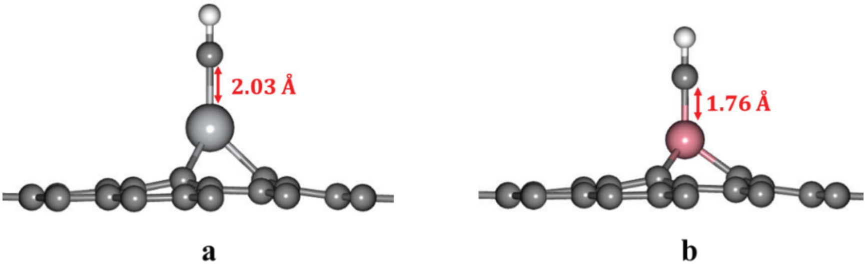

Figure 5. The optimized geometries of CH molecule binding onto the (a) Ti-embedded and (b) Co-embedded graphene surface (The light grey ball: titanium atom, the dark grey balls: carbon atoms, the white balls: hydrogen atoms, and the pink ball: cobalt atom).

The binding energies of the CH molecule to Ti and Co embedded graphene surfaces were calculated as -2.53 eV -2.83 eV, respectively through Eq. 1. The optimized bond lengths of the CH molecule on both surfaces and in the gas phase are given in Table 4.

Table 4. The optimized bond lengths of the CH molecule on both surfaces and in the gas phase (All the bond lengths given are written using the Angstrom (Å) measurement unit).

Bond type	Ti-embedded graphene	Co-embedded graphene	Gas phase
C-H	1.097	1.098	1.08

Table 4 reveals that C-H bonds are elongated on both surfaces according to the gas phase.

3.5. The Binding Mechanism of C and H atoms

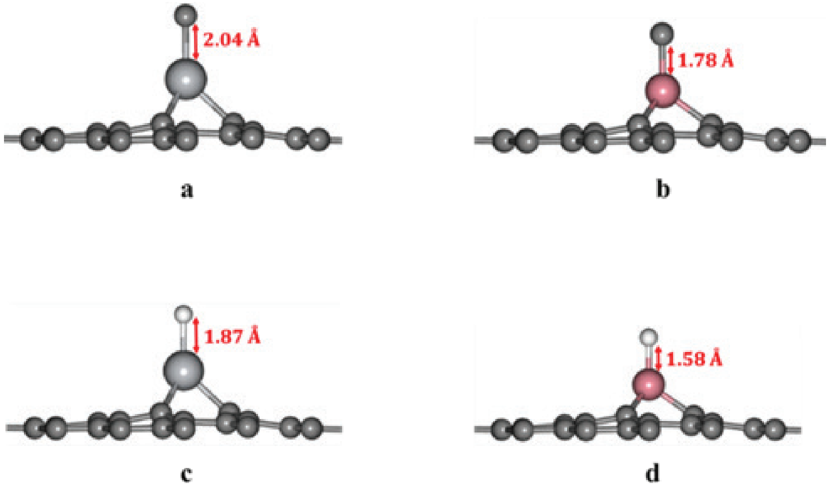

Figure 6. The optimized geometries of the C atom binding onto the (a) Ti-embedded and (b) Co-embedded graphene surface and H atom binding onto the (c) Ti-embedded and (d) Co-embedded graphene surface (The light grey ball: titanium atom, the dark grey balls: carbon atoms, the white balls: hydrogen atoms, and the pink ball: cobalt atom).

The optimized bonding geometries of the C and H atoms on both surfaces are shown in Figure 6. According to our calculations, the binding energies onto Ti- and Co-embedded graphene surfaces were found to be -1.89 eV and 2.02 eV, respectively, fort he C atom and

-2.15 eV and -2.20 eV, respectively, fort he H atom.

As seen in Figure 6, the bond lengths between C-Ti and C-Co were found to be 2.04 Å and 1.78 Å, respectively, and between H-Ti and H-Co were found to be 1.87 Å and 1.58 Å, respectively.

3.6. Double Bonding Mechanisms of CH_x (x = 0-3) + H types on Ti- and Co-embedded Graphene Surfaces

It is very important to know the double bonding mechanisms in order to examine the catalytic processes in a reaction. The double bonding geometries actually show the final state geometries for a reaction step. The optimized bonding geometries of double bonding types obtained by sequential hydrogen dissociation of CH_4 molecule on Ti- and Co-embedded graphene surfaces are presented in Figure 7.

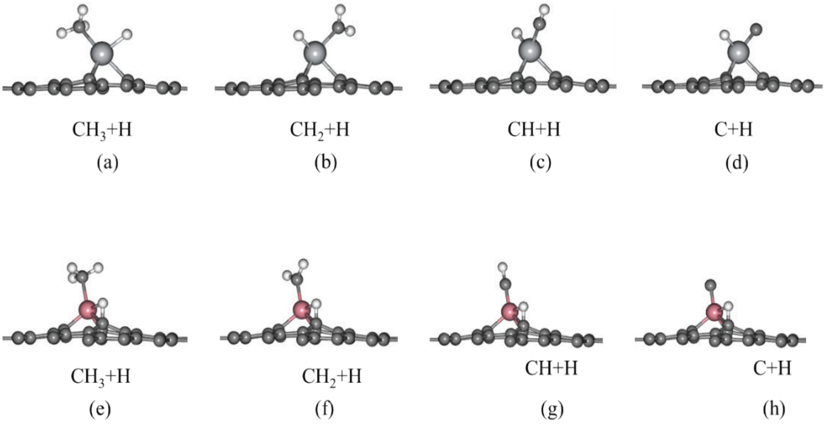

Figure 7. The optimized double bonding geometries on the (a-d) Ti-embedded and (e-h) Co-embedded graphene surfaces.

It can be stated considering Figure 7(a-d) that CH_x (x = 0-3) types and H atoms prefer to bond to Ti metal atoms. In Figure (e-h), similarly CH_x (x = 0-3) types tend to bond to Co atoms, while H atoms are bonded to the carbon atoms closest to Co atoms.

3.7. Analysis of Transition States for the CH_4 Dissosiation Reaction

The most common expectation for the CH_4 dissociation reaction is sequential breaking of C-H bonds. (Wang et al., 2006; Zuo et al., 2010). In this study, the transition states for the CH_4 sequential dissociation reaction were investigated by using the climbing image nudged elastic band (CINEB) method, which is an algorithm program that calculates the activation barrier for a reaction. Activation barrier refers to the energy needed for a reaction to occur. For example, the CINEB method for the AB → A + B reaction allows the required activation barrier to be calculated and the transition state geometry to be obtained. For te CH_4 dissociation, all the initial and final state geometries are shown in Figure 2-5 and Figure 7, respectively. For example, the final state geometries for the initial states given in Figure 2a and 2b are presented in Figure 7a and 7e. For all reaction intermediate steps, activation barrier (Ea) and reaction energy (E_r) were calculated using Eq. (2) and (3), respectively.

$$E_a = E_{GD} - E_{BD} \tag{2}$$

$$E_r = E_{BD} - E_{SD} \tag{3}$$

where, E_{BD} is the total energy of the CHx (x = 1 → 4), E_{SD} is the total energy of CH_{x-1}+H (x= 0→3), and E_{GD} is the transition state (TS) energy between CH_x (x= 1→4) and CH_{x-1} +H (x= 0→3) attached to the Ti- and Co-embedded graphene surfaces.

3.7.1. Analysis of transition states for $CH_4 \rightarrow CH_3 + H$ reaction intermediate step

The initial and final state geometries for CH_4 dissociation were determined utilizing the geometric optimizations described in the previous sections. When one of the four C-H bonds breaks in the CH_4 molecule, which is attached to Co and Ti embedded graphene surfaces through van der Waals interaction, the CH_3 + H is formed. The optimized CH_3 + H geometries on both surfaces give the final state geometry of the first reaction intermediate step. Thus, a single hydrogen atom was moved away from the CH_4 at the first reaction intermediate step and the first transition state geometries (TS1) obtained on both surfaces are shown in Figure 8.

In the transition state, the single hydrogen atoms (H4) splitted from CH_4 on Ti- and Co embedded graphene surfaces are 3.19 Å and 2.24 Å, respectively, above the closest carbon atom. The activation barriers and reaction energies calculated for CH_4 dissociation on both surfaces are given in Table 5.

Table 5. The possible reaction path, calculated activation barriers, and reaction energies for the CH_4 sequential dissociation reaction.

The possible reaction path for the CH_4 dissociation		Activation energy (E_a, eV)		Reaction energy (E_r, eV)	
		Ti-embedded graphene	Co-embedded graphene	Ti-embedded graphene	Co-embedded graphene
CH_4 → CH_3+H	CH_4 →TS1 → CH_3+H	1.29	1.01	0.01	0.37
CH_3 → CH_2+H	CH_3 →TS2 → CH_2+H	2.22	2.02	0.06	0.41
CH_2 → CH+H	CH_2 →TS3 → CH+H	2.11	1.89	0.12	0.35
CH → C+H	CH →TS4 → C+H	2.32	1.86	0.03	0.31

It can be seen that the first steps have the lowest barrier energy for the both surfaces. The activation energies of the intermediate steps for the

Ti-embedded graphene are higher than that of the Co-embedded graphene as well. The computed activation energy barriers for the CH_4 dissociation reaction steps on Ti- and Co-embedded graphene are lower than that on pristine graphene (Li et al., 2018).

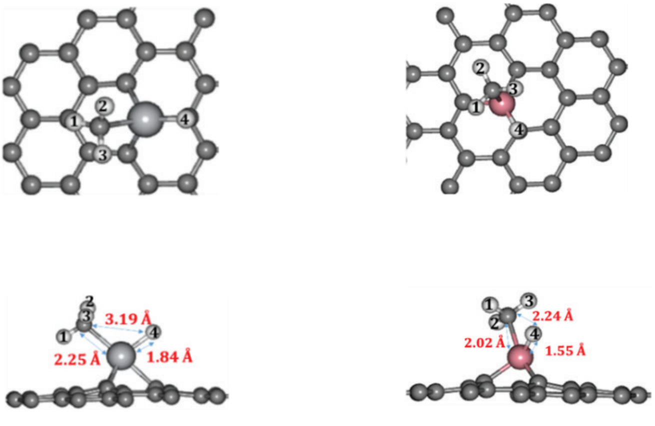

(a) **(b)**

Figure 8. The transition state (TS1) geometries of $CH_4 \rightarrow CH_3 + H$ dissociation on (a) Ti-embedded and (b) Co-embedded graphene surface.

The reaction energies of 0.01 eV and 0.37 eV were obtained, respectively, for the $CH_4 \rightarrow CH_3 + H$ dissociation on the Ti- and Co-embedded graphene surface. According to the reaction energies, this reaction takes place endothermically on both surfaces. The activation barriers calculated on Ti- and Co-embedded graphene surfaces are shown in Figure 9.

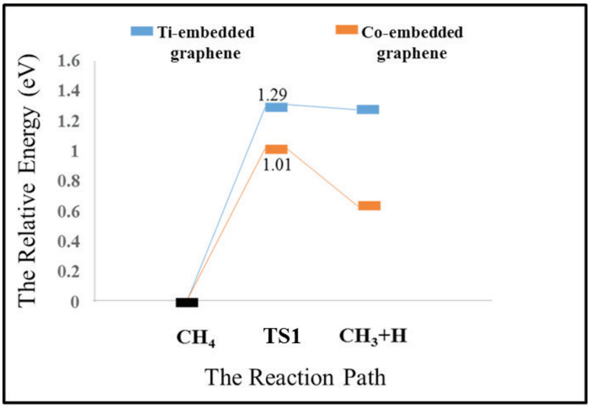

Figure 9. The activation barriers calculated through the relative energy diagram for the $CH_4 \rightarrow CH_3 + H$ reaction.

3.7.2. Analysis of transition states for $CH_3 \rightarrow CH_2 + H$ reaction intermediate step

For the second intermediate step, the initial state geometries were selected as CH_3 molecule bonding geometries onto the both metal embedded graphene surfaces presented in Figure 3a and Figure 3b.

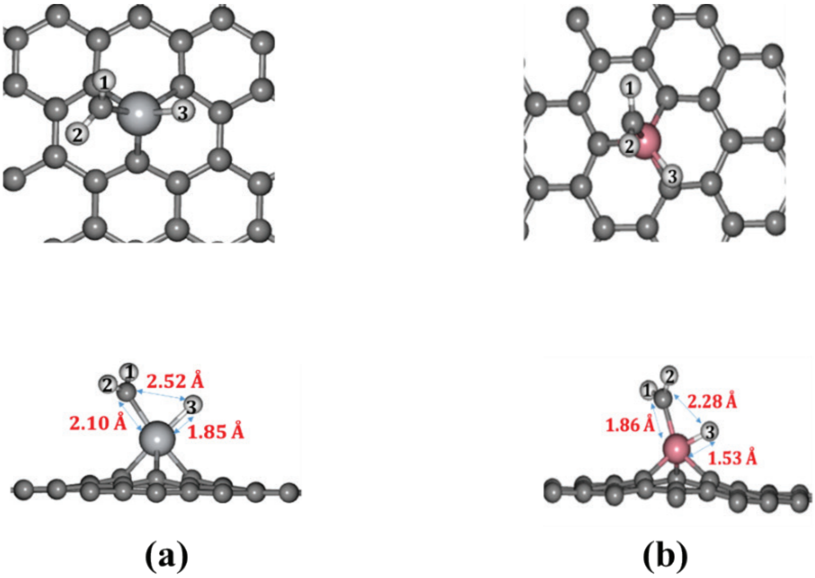

Figure 10. The transition state (TS1) geometries of $CH_3 \rightarrow CH_2 + H$ *dissociation on (a) Ti-embedded and (b) Co-embedded graphene surface.*

Final state geometries for CH_2+H are given in Figure 7b and Figure 7f according to the geometric optimization results. The transition state geometries (TS2) obtained for the determined initial and final state geometries are shown in Figure 10. In this dissociation step, a single hydrogen atom was removed from the CH_3 molecule attached to both surfaces. This hydrogen atom (H3) is bonded to the transition metal Ti and Co, respectively, on the both surfaces.

In this transition state (TS2), the single hydrogen atoms (H3) splitted from CH_3 on Co and Ti embedded graphene surfaces are at a distance of 2.52 Å and 2.28 Å, respectively, from the closest carbon atom. Other bond lengths CH_2-Ti, CH_2-Co, H3-Ti and H3-Co were found to be 2.10 Å, 2.28 Å, 1.85 Å, and 1.53 Å, respectively. Our calculations yield in reaction energies of 0.06 eV and 0.41 eV, respectively, for $CH_3 \rightarrow CH_2 + H$ and activation barriers calculated on both surfaces are shown in Figure 11.

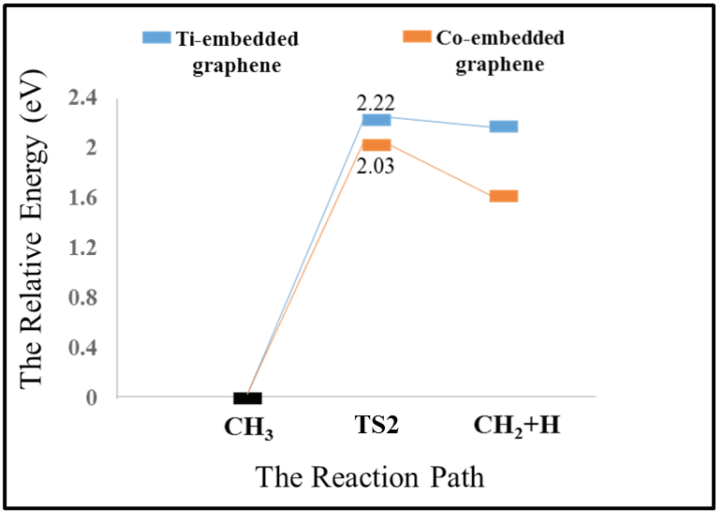

Figure 11. The activation barriers calculated through the relative energy diagram for CH_3 → CH_2 + H reaction.

3.7.3. Analysis of transition state for $CH_2 \rightarrow CH + H$ reaction intermediate step

In the third reaction step, a single hydrogen atom was removed from the CH_2 molecule optimized on Ti- and Co-embedded graphene surfaces as shown in Figure 4a and Figure 4b.

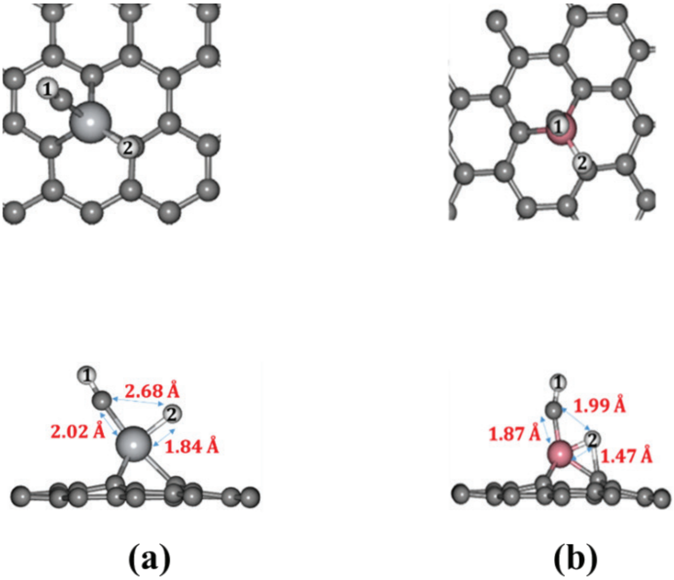

Figure 12. Transition state (GD3) geometries for CH2 → CH + H decomposition on (a) Ti and (b) Co embedded graphene surfaces.

In the transition state and on the Ti and Co embedded graphene surfaces, the H_2 atom attached to the CH_2 detaches from the molecule at a distance of 2.68 Å and 1.99 Å, respectively. The bond distances between the resulting new bond formations CH-Ti and CH-Co were 2.02 Å and 1.87 Å, respectively.

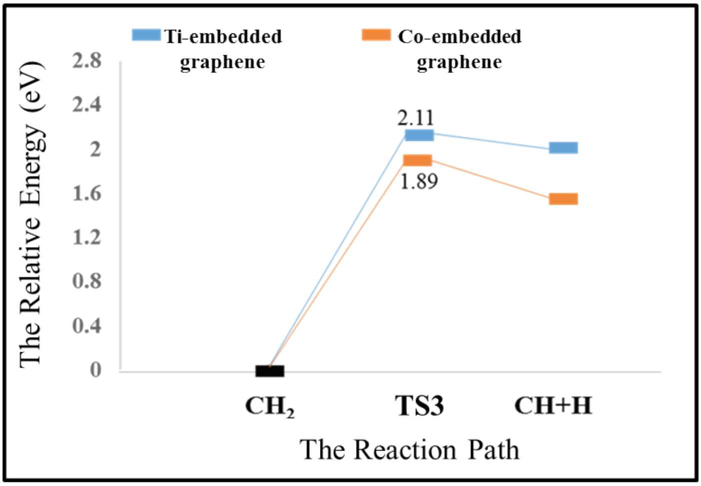

Figure 13. The activation energy barriers computed by relative energy diagram for $CH_2 \rightarrow CH + H$ reaction.

The bond lengths between the detached H_2 atom and the Ti and Co atoms on the graphene surface were found to be 1.84 Å and 1.47 Å, respectively. According to our calculations, the reaction energies of 0.12 eV and 0.35 eV, respectively, were obtained for $CH_2 \rightarrow CH + H$. This reaction is therefore endothermic on both surfaces. Activation barriers calculated on Ti and Co embedded graphene surfaces are shown in Figure 13.

3.7.4. Analysis of transition state for CH → C + H reaction intermediate step

The last step of CH_4 sequential dissociation reaction is the decomposition of CH molecules into C+H atoms. The optimized bonding geometries of the CH molecule on both surfaces are shown in Figure 5a and 5b and the most stable final state geometries of the C + H formed at the end of the reaction on the both surfaces are shown in Figure 7d and Figure 7h similar to the other reaction steps. The transition state geometries on the both surfaces are given in Figure 14.

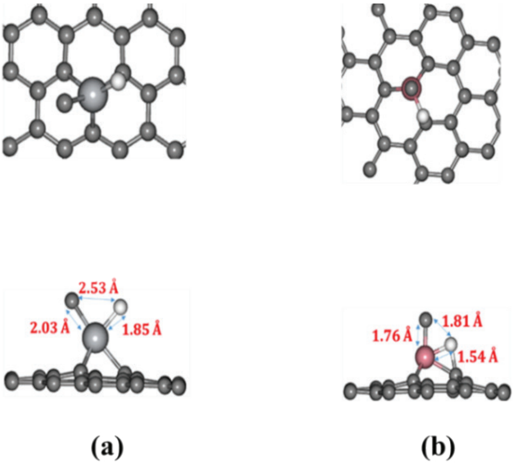

Figure 14. CH → C + H decomposition transition state (TS4) structures of (a) Ti- and (b) Co-embedded graphene surfaces.

The H atoms bonded to the CH molecule are detached from CH on Ti/Co embedded graphene surfaces on transition state by a distance of 2.53 Å and 1.81 Å, respectively. Bond distances between the new arising bond formations C-Ti and C-Co were found to be 2.03 Å and 1.85 Å, respectively. The bond lengths between the detached H atom and Ti and Co atoms were found to be 1.85 Å and 1.54 Å, respectively. According to our calculations, reaction energies on the Ti- and Co-embedded graphene surfaces for CH → C + H were 0.03 eV and 0.31 eV, respectively. Therefore, this reaction is endothermic on both surfaces. Activation barriers computed on the Ti and Co-embedded graphene surfaces are shown in Figure 15.

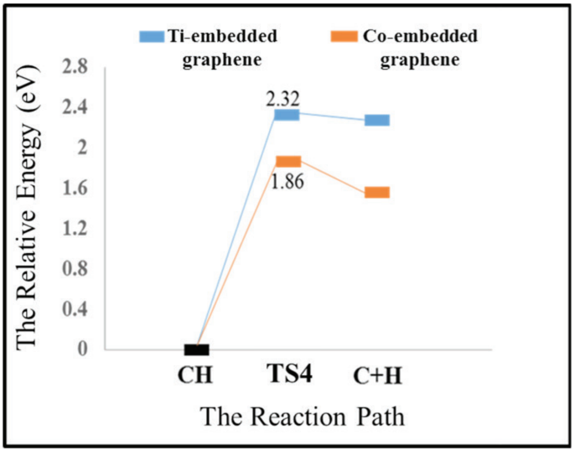

Figure 15. The relative energy diagram of the CH → C + H reaction.

CONCLUSION

The CH_4 sequential dissociation reaction was analyzed on the Ti- and Co-embedded graphene surfaces via density functional theory. Firstly, the binding energies of the CH_x (x=0-4) structures and the H atom on the both surfaces were computed and a comparison of the gas phase has been performed. Then, the final state geometries of the reaction mechanisms CH_x+H (x=0-3) and the most stable bonding geometries of CH_x+H (x=0→3) were obtained. The transition state geometries between the initial and final states were determined by the CINEB method for all the reaction steps and the reaction/activation energies were calculated. The results reveal that the CH_x (x=0-4) and H atom on the Co- embedded graphene bond to the surface by relatively lower binding energies compared to that of Ti-embedded graphene. In other words, the CH_x (x=0-4) and H atom on the Co-embedded graphene shows more stable behavior in terms of binding. The relative energy diagram that the activation energies obtained on Co-embedded graphene are lower than that of Ti-embedded graphene. This indicates that Co-embedded graphene is a more promising host surface for the CH_4 dissociation. So far, in the literature, there has been no report about the CH_4 dissociation reaction on metal-embedded graphene surfaces including the reaction steps considered. Otherwise, the results of this study yields in lower activation barriers than that of all the steps for pristine graphene.

ACKNOWLEDGEMENT

All computations given in this manuscript were performed by TÜBİTAK ULAKBİM, High Performance and Grid Computing Center (TRUBA).

.

REFERENCES

Akça A, Genç AE, Kutlu B, 2019. BH_4 Dissociation on Various Metal (111) Surfaces: A DFT Study. Applied Surface Science, 473: 681-692.

Egeberg RC, Ullmann S, Alstrup I, Mullins CB, Chorkendorff I, 2002. Dissociation of CH_4 on Ni (111) and Ru (0001). Surface Science, 497(1-3): 183-193.

Giannozzi P, Baroni S, Bonini N, Calandra M, Car R, Cavazzoni, C, Dal Corso A, 2009. Quantum Espresso: A Modular and Open-Source Software Project For Quantum Simulations of Materials. Journal of Physics: Condensed Matter, 21(39): 395502.

Giannozzi P, Andreussi O, Brumme T, Bunau O, Nardelli MB, Calandra M, Colonna N, 2017. Advanced Capabilities For Materials Modelling with Quantum Espresso. Journal of Physics: Condensed Matter, 29(46): 465901.

Grimme S, Antony J, Ehrlich S, Krieg H, 2010. A Consistent and Accurate ab Initio Parametrization of Density Functional Dispersion Correction (DFT-D) For The 94 Elements H-Pu. The Journal of Chemical Physics, 132(15): 154104.

He Y, Zhou W, Qian G, Chen B, 2014. Methane Storage in Metal–Organic Frameworks. Chemical Society Reviews, 43(16): 5657-5678.

Hou M, Zhang X, Fu C, Cen W, Chen J, 2020. Effects of Pd/Pt Bimetal Supported By Γ-Al_2O_3 Surface on Methane Activation. Physical Chemistry Chemical Physics, 22(8): 4692-4698.

Krasheninnikov AV, Lehtinen PO, Foster AS, Pyykkö P, Nieminen RM, 2009. Embedding Transition-Metal Atoms in Graphene: Structure, Bonding, and Magnetism. Physical Review Letters, 102(12): 126807.

Kratzer P, Hammer B, Norskov JK, 1996. A Theoretical Study of CH_4 Dissociation on Pure and Gold-Alloyed Ni (111) Surfaces. The Journal of Chemical Physics, 105(13): 5595-5604.

Kresse G, Joubert D, 1999. From Ultrasoft Pseudopotentials to The Projector Augmented-Wave Method. Physical Review B, 59(3): 1758.

Li J, Croiset E, Ricardez-Sandoval L, 2013. Effect of Metal–Support Interface During CH_4 and H_2 Dissociation on Ni/Γ-Al_2O_3: A Density Functional Theory Study. The Journal of Physical Chemistry C, 117(33): 16907-16920.

Li K, Li H, Yan N, Wang T, Zhao Z, 2018. Adsorption and Dissociation of CH_4 on Graphene: A Density Functional Theory Study. Applied Surface Science, 459: 693-699.

Li K, He C, Jiao M, Wang Y, Wu Z, 2014. A First-Principles Study on the Role of Hydrogen in Early Stage of Graphene Growth During The CH_4 Dissociation on Cu (111) and Ni (111) Surfaces. Carbon, 74: 255-265.

Li K, Jiao M, Wang Y, Wu Z, 2013. CH_4 Dissociation on NiM (111)(M= Co, Rh, Ir) Surface: A First-Principles Study. Surface Science, 617: 149-155.

Li K, Zhou Z, Wang Y, Wu Z, 2013. A Theoretical Study of CH_4 Dissociation NiPd (111) Surface. Surface Science, 612: 63-68.

Liao MS, Au CT, Ng CF, 1997. Methane Dissociation on Ni, Pd, Pt And Cu Metal (111) Surfaces A Theoretical Comparative Study. Chemical Physics Letters, 272(5-6): 445-452.

Liu H, Zhang R, Yan R, Li J, Wang B, Xie K, 2012. Insight into CH_4 Dissociation on NiCu Catalyst: A First-Principles Study. Applied Surface Science, 258(20): 8177-8184.

Liu H, Zhang R, Yan R, Wang B, Xie K, 2011. CH_4 Dissociation on NiCo (111) Surface: A First-Principles Study. Applied Surface Science, 257(21): 8955-8964.

Monkhorst HJ, Pack JD, 1976. Special Points For Brillouin-Zone Integrations. Physical Review B, 13(12): 5188.

Pucker J, Zwart R, Jungmeier G, 2012. Greenhouse Gas and Energy Analysis of Substitute Natural Gas From Biomass For Space Heat. Biomass and Bioenergy, 38: 95-101.

Rahmani Didar B, Balbuena PB, 2020. Methane Dehydrogenation on Cu and Ni Surfaces with Low and Moderate Oxygen Coverage. International Journal of Quantum Chemistry, 120(2): 26065.

Roy S, Hariharan S, Tiwari AK, 2018. Pt–Ni Subsurface Alloy Catalysts: An Improved Performance Toward CH_4 Dissociation. The Journal of Physical Chemistry C, 122(20): 10857-10870.

Tang Y, Liu Z, Chen W, Ma D, Chang S, Dai X, 2016. Catalytic conversion of CH_x and CO_2 on non-noble metallic impurities in graphene. Physical Chemistry Chemical Physics, 18(25): 16998-17009.

Wang L, Luo Q, Zhang W, Yang J, 2014. Transition Metal Atom Embedded Graphene For Capturing CO: A First-Principles Study. International Journal of Hydrogen Energy, 39(35): 20190-20196.

Wang SG, Cao DB, Wang J, Jiao H, 2006. CH_4 dissociation on Ni surfaces: density functional theory study. Surface science, 600(16): 3226-3234.

Yang CK, 2009. A Metallic Graphene Layer Adsorbed with Lithium. Applied Physics Letters, 94(16): 163115.

Zhang R, Song L, Wang Y, 2012. Insight into the Adsorption and Dissociation of CH_4 on Pt (hkl) Surfaces: A Theoretical Study. Applied Surface Science, 258(18): 7154-7160.

Zuo Z, Huang W, Han P, Li Z, 2010. A Density Functional Theory Study of CH_4 Dehydrogenation On Co (1 1 1). Applied Surface Science, 256(20): 5929-5934.

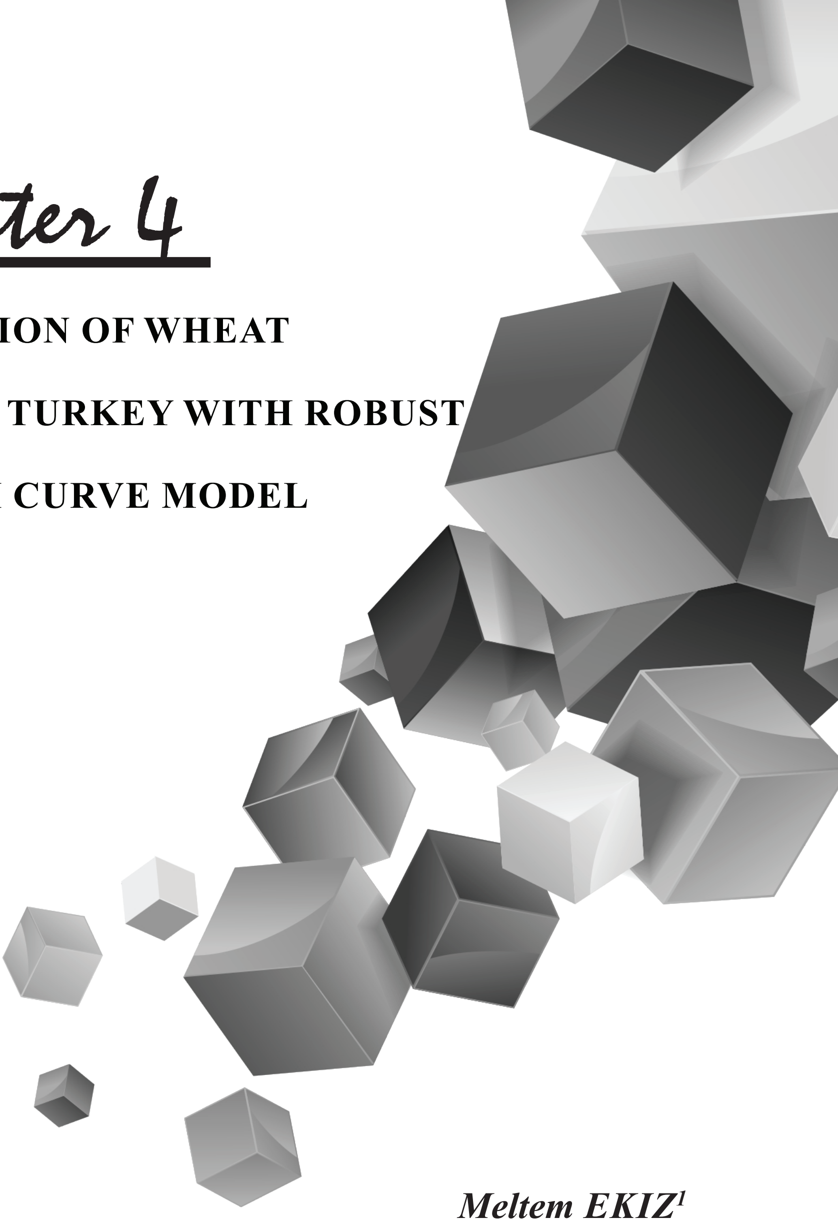

Chapter 4

PREDICTION OF WHEAT YIELD IN TURKEY WITH ROBUST GROWTH CURVE MODEL

***Meltem EKIZ*[1]**
***Osman Ufuk EKIZ*[2]**

---

[1] Assoc. Prof. Dr., Gazi University, Faculty of Science, Department of Statistics, ozmeltem@gazi.edu.tr

[2] Asst. Prof. Dr., Gazi University, Faculty of Science, Department of Statistics, ufukekiz@gazi.edu.tr

1. Introduction

Wheat is a type of cereal that is of great importance in terms of meeting the food needs of many people in the world. The consumption of wheat products in Turkey ranks first. Turkey is self-sufficient in wheat production. However, in some years' adverse climatic conditions may lead to production and quality problems. Such problems cause importation, as the wheat demands are not met.

Product monitoring and yield estimation studies are expected to contribute to the development of the country by providing benefits in many areas; for instance, efficient usage of national resources, determination of the optimal areas available for the sowing of specific crops by using risk analysis, the accuracy of production of meteorological and phenological statistical data, assistant to farmers to take immediate action if the products start to go bad, the establishment of necessary import and export connections before the harvest, identification of the vulnerable segments of the society and initiation of necessary aid activities (Şimşek, Mermer, Yıldız, Özaydın, & Çakmak, 2007). Prediction of crop yield of mainly strategic plants such as wheat, corn, rice has always been an interesting research area in the national and international economic programming. Nowadays, there are a lot of yield prediction models. Most classified into two groups, statistical models and crop simulation models (Dahikar & Rode, 2014).

In this study, the statistical growth model called the growth curve model (*GCM*) is used to make short-term predictions of the wheat yield in Turkey. The wheat yield per decare in Turkey will vary according to several factors such as, in which area the wheat seed was sown and which type of wheat was employed. Therefore, the data of wheat yield of provinces were used to make inferences about average wheat yield per decare.

To estimate the parameters of the growth curve model under a normal assumption, classical methodologies such as ordinary least square (*OLS*) and maximum likelihood (*ML*) estimation were used to solve a variety of statistical problems. However, these estimators, which have many mathematical and statistical optimal properties, lead to incorrect results in some cases. Particularly deviant observations, called outliers, could have potentially a large influence on the resulting of statistical inferences. Thus, it is important to detect and investigate the effect of these points on the proposed model.

Some statistical approaches were constructed to deal with these problems recently (Huber, 1981; Cook, 1977). In general, there are two methods for the solutions to these problems: one referred to as statistical diagnostics and the other as robust statistics. The basis of the first method is the determination of points, which does not fit the assumed model, and investigation of influential points having a large impact on the statistical inference obtained from the assumed model (Cook & Weisberg, 1982). However, these methods may consider false observations to be outliers since the statistics employed to detect outliers are influenced by these values. Therefore, the obtained estimations and predictions would be far from reality, particularly, when there exists more than one outlier in the data. Hence, a statistical method called robust analysis was developed, which provides little change in statistical inferences based on the assumed model when small or medium deviations occur. (Huber, 1981; Hampel, Ronchetti, Rousseeuw, & Stahel, 1986). The first goal of the diagnostic methods is the deletion of peculiar points after the determination. Then, the estimation of the model parameters with the clean data set by the *OLS*. Whereas, in a robust analysis first a model is fitted to the majority of the data and then observations having large residuals are detected as outliers (Rousseeuw & Leroy, 1987). Thus, GCMs based on robust estimators are suggested to use in the estimation procedure.

2. Materials and methods

In literature, there are studies on wheat yield and future predictions (Pantazi, Moshou, Alexandridis, Whetton, & Mouazen, 2016; Bell & Fischer, 1994). However, taking no account of outliers, which are points that differ from the bulk of the data or fits to a different distribution, could cause biases on these predictions (Rousseeuw & Leroy, 1987). The first part of this study is constructed to predict the wheat yield in Turkey by considering that the first-order growth curve of time could be fitted to data. In the estimation procedure of *GCM* non-robust and robust estimators, which are resistant to outliers, are used. Secondly, to show the differences between estimated *GCM*s based on *OLS* and the robust least median square (*LMS*), and robust least trimmed square (*LTS*) estimators, they are plotted on a single figure (see Figure b).

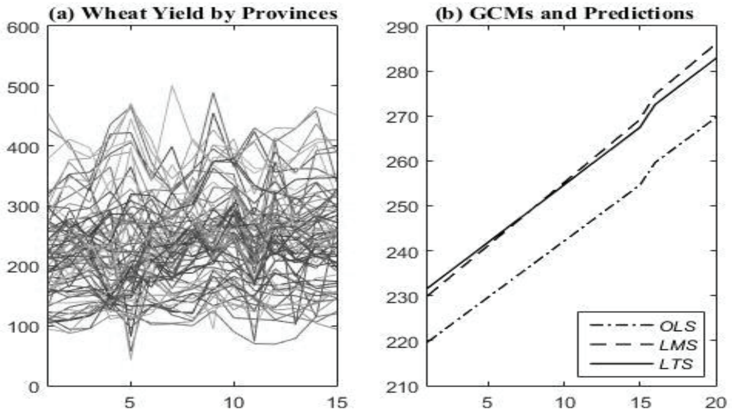

Figure a. Wheat yield by provinces for 2004-2018; **b.** First order *GCM*s for 2004-2018 and predictions for 2020-2024 based on *OLS*, *LMS*, and *LTS* estimators.

2.1. Study area and data set

To make short-term predictions of Turkey's wheat yield with GCM, the data that consists of wheat yields by provinces (kg per decare) is used. Table 1 summarizes the data of 79 provinces from 2004 to 2018 (Turkish Statistical Institute [TSI], 2018).

Table 1. Wheat yield (kg per decare) in Turkey's provinces for 2004 to 2018 $(\boldsymbol{Y}')$.

		Years														
	Provinces	2004	2005	2006	2007	2008	2009	2010	2011	2012	2013	2014	2015	2016	2017	2018
1	Adana	270	353	356	387	406	357	328	359	395	371	286	390	356	386	390
2	Adıyaman	135	225	235	236	170	255	237	318	273	285	273	295	280	297	299
3	Afyonkarahisar	242	216	230	167	199	213	315	222	241	257	204	279	224	263	261
4	Aksaray	211	217	261	242	221	292	271	275	295	319	207	374	284	322	328
5	Amasya	314	373	337	203	316	327	259	348	293	293	204	326	313	295	290
6	Ankara	201	236	229	122	162	250	231	257	245	256	179	254	256	230	235
7	Antalya	274	254	251	232	276	258	223	248	252	245	231	241	219	254	256
8	Ardahan	123	120	121	149	183	150	118	108	157	113	111	109	104	158	153
9	Artvin	153	211	210	240	236	179	145	167	218	169	146	122	114	106	124
10	Aydın	379	411	397	319	445	351	319	322	402	395	363	361	382	405	410
11	Ağrı	108	110	118	142	125	183	182	169	159	195	159	151	150	140	144
12	Balıkesir	277	304	296	256	311	255	253	261	250	249	266	241	299	309	315

		Years														
	Provinces	2004	2005	2006	2007	2008	2009	2010	2011	2012	2013	2014	2015	2016	2017	2018
13	Bartın	161	173	195	198	205	182	175	169	194	178	142	132	139	157	156
14	Batman	211	247	251	291	82	254	323	270	256	306	285	285	275	273	294
15	Bayburt	133	148	150	153	180	182	259	216	232	198	181	229	186	114	266
16	Bilecik	258	273	217	200	248	229	205	235	226	238	278	208	208	219	191
17	Bingöl	174	179	200	219	225	203	203	212	94	320	258	278	264	258	285
18	Bitlis	111	131	138	140	109	132	129	153	133	145	135	130	161	150	153
19	Bolu	214	203	219	215	243	246	202	239	239	230	271	222	258	254	229
20	Burdur	228	203	218	195	250	250	233	262	244	268	237	221	239	238	256
21	Bursa	262	278	280	293	308	294	233	271	267	263	297	270	273	294	323
22	Denizli	271	248	332	247	299	290	277	322	374	373	328	323	311	317	302
23	Diyarbakır	235	235	286	294	173	266	282	315	305	328	276	309	320	340	313
24	Düzce	244	247	266	269	271	266	258	253	303	241	229	237	231	232	262
25	Edirne	321	352	325	420	422	343	399	303	455	365	424	356	362	362	346
26	Elazığ	275	208	254	256	214	218	227	254	248	215	170	284	224	232	202
27	Erzincan	193	197	221	226	219	208	187	240	237	206	166	207	228	205	260
28	Erzurum	105	109	116	136	133	134	143	139	160	182	169	167	173	166	171
29	Eskişehir	257	259	229	186	189	243	229	269	279	294	216	272	315	279	291
30	Gaziantep	296	316	336	365	238	327	325	359	356	353	216	407	264	392	398
31	Giresun	138	138	141	143	141	126	135	141	120	166	96	164	160	167	154
32	Gümüşhane	161	156	159	161	158	139	125	120	192	166	148	208	210	220	219
33	Hakkari	112	120	130	140	142	151	151	145	165	126	148	126	129	104	94
34	Hatay	302	377	379	413	465	410	323	412	370	412	319	414	390	411	410
35	Isparta	228	242	257	161	207	210	187	188	208	205	176	188	173	176	174
36	Iğdır	225	220	235	225	237	239	187	245	262	246	243	257	247	214	216
37	Kahramanmaraş	199	198	191	197	186	218	198	256	331	328	264	289	270	288	323
38	Karabük	160	181	184	182	200	182	145	174	175	164	214	169	165	142	157
39	Karaman	229	164	213	215	195	212	162	209	219	246	169	239	182	232	231
40	Kars	105	87	95	117	115	105	104	107	148	136	128	164	136	121	146
41	Kastamonu	179	151	157	138	185	173	151	164	163	165	171	155	162	179	185
42	Kayseri	181	178	192	163	183	173	180	198	203	256	215	250	248	217	239
43	Kilis	169	264	219	234	57	187	175	247	275	251	74	322	101	281	215
44	Kocaeli	246	272	247	270	270	218	212	209	231	332	276	244	243	227	219
45	Konya	193	173	248	159	160	260	217	335	257	324	263	349	261	284	300
46	Kütahya	223	215	231	194	220	209	179	197	197	190	218	159	164	239	196
47	Kırklareli	326	333	306	383	390	308	283	324	402	378	407	346	381	437	390
48	Kırıkkale	174	206	189	111	117	238	213	237	215	277	237	262	258	235	234
49	Kırşehir-	243	241	225	149	150	276	256	252	224	285	203	282	242	272	284
50	Malatya	162	147	156	135	96	133	144	154	154	169	124	195	171	158	146

		Years														
	Provinces	2004	2005	2006	2007	2008	2009	2010	2011	2012	2013	2014	2015	2016	2017	2018
51	Manisa	195	201	213	145	209	207	196	203	277	286	258	276	260	277	264
52	Mardin	233	184	230	234	398	181	313	306	381	381	354	374	353	402	314
53	Mersin	189	199	243	223	224	221	180	204	268	267	215	241	211	246	262
54	Muğla	242	243	251	254	282	245	216	261	268	207	250	266	266	282	273
55	Muş	120	127	122	127	112	120	165	164	148	178	180	193	174	216	281
56	Nevşehir	190	216	216	145	146	207	234	272	207	255	168	265	211	200	206
57	Niğde	167	173	183	143	153	206	205	241	239	305	187	315	256	272	329
58	Ordu	117	110	134	127	121	102	103	100	125	90	70	69	79	115	120
59	Osmaniye	287	347	340	397	409	341	501	407	368	343	303	339	326	349	353
60	Sakarya	299	296	235	307	365	271	213	248	254	300	240	221	232	252	259
61	Samsun	214	237	260	301	328	291	244	286	260	273	248	301	302	291	245
62	Siirt	161	187	190	255	43	239	237	230	259	260	261	257	248	258	260
63	Sinop	157	158	166	148	197	164	224	215	231	214	203	221	205	216	206
64	Sivas	150	167	163	128	171	181	178	257	207	242	174	253	209	196	231
65	Tekirdağ	428	405	340	436	465	372	322	355	489	378	430	407	429	459	340
66	Tokat	230	220	236	183	290	254	243	271	250	248	179	279	270	241	224
67	Tunceli	113	94	95	149	132	135	123	122	183	147	151	186	187	162	166
68	Uşak	245	269	228	228	280	269	284	313	210	253	215	235	231	291	255
69	Van	94	89	124	161	153	144	131	113	130	135	123	134	135	136	158
70	Yalova	244	278	248	286	287	230	236	236	294	265	270	218	259	284	272
71	Yozgat	210	251	201	176	177	249	219	262	226	239	196	243	221	220	215
72	Zonguldak	212	204	204	196	199	188	154	161	181	176	145	110	123	139	144
73	Çanakkale	304	276	284	341	350	297	369	309	340	310	330	326	315	322	290
74	Çankırı	215	212	169	127	197	263	268	257	221	291	247	265	265	243	250
75	Çorum	247	252	206	157	215	255	294	289	229	237	201	286	285	263	248
76	İstanbul	454	396	381	394	471	390	345	378	427	385	409	430	429	465	452
77	İzmir	296	263	279	239	320	317	293	302	374	378	334	319	344	346	347
78	Şanlıurfa	220	291	296	324	279	312	248	297	363	334	304	341	301	338	296

In this research, the response variable $\boldsymbol{Y}_{15\times 79}$ represents a matrix where y_{ij} denotes the wheat yield of province i in the year j, with $i = 1,\ldots,79$ and $j = 1,\ldots,15$. $\boldsymbol{Y}'$ denotes the transpose of the response variable matrix $\boldsymbol{Y}$. Design matrix $\boldsymbol{X}_{p\times m}$ given in Equation (1) is a 15×2 dimensional matrix where the first column consists of 1's and the second column consists of the numbers 1 to 15 used for years 2004 to 2018, respectively, because the data could specify a functional form of the linear growth. To obtain wheat yield predictions for 2020 to 2024, a 5×2 dimensional $\boldsymbol{X}$ matrix is used. Hence, the two matrices are determined as

$$\boldsymbol{X}_{15\times 2}=\begin{bmatrix}1 & 1\\ 1 & 2\\ 1 & 3\\ . & .\\ . & .\\ . & .\\ 1 & 15\end{bmatrix} \quad \text{and} \quad \boldsymbol{X}_{5\times 2}=\begin{bmatrix}1 & 17\\ 1 & 18\\ 1 & 19\\ 1 & 20\\ 1 & 21\end{bmatrix},$$

respectively. By using the first manner of the design matrix, the parameters B_0 and B_1 of the *GCM* are estimated (Pan & Fang, 2002).

Three different methods including *OLS*, *LMS*, and *LTS* were used to reconstruct *GCM*, separately. This makes it possible to show that outlier observations may lead to differences in the estimation of model parameters and predictions of wheat yield.

2.2. Methodology

The GCM usually expressed as

$$\boldsymbol{Y}_{p\times n}=\boldsymbol{X}_{p\times m}\boldsymbol{B}_{m\times r}\boldsymbol{Z}_{r\times n}+\boldsymbol{e}_{p\times n} \tag{1}$$

is the change in a growth that corresponds to the response variable $\boldsymbol{Y}$. This model indicates analytically how the parameters ($B_0, B_1,$ etc.) and their standard errors ($\varepsilon_0, \varepsilon_1,$ etc.) behave in a deterministic procedure for varying points of time (Pan & Fang, 2002). $\boldsymbol{X}$ and $\boldsymbol{Z}$ are the design matrices. However, $\boldsymbol{Z}$ used for grouped repeated measures is not taken into account since only the growth of Turkey's wheat yield in the provinces on different time points is the subject to be researched ($\boldsymbol{Z}$ is a 1×79 dimensional vector consisting of 1's. At this point, the vector of unknown parameters, the error, and design matrix are denoted as $\boldsymbol{B}_{2\times 1}$, $\boldsymbol{\varepsilon}_{15\times 79}$, and $\boldsymbol{X}_{15\times 2}$, respectively). Each column of $\boldsymbol{\varepsilon}$ is assumed to be $N_p(\underline{0},\Sigma)$ where $\underline{0}$ is a mean vector and $\Sigma>0$ is the unknown covariance matrix. Hence, $\boldsymbol{Y} \sim \boldsymbol{N}_{p\times n}(\boldsymbol{XBZ},\boldsymbol{\Sigma},\boldsymbol{I}_n)$ where $\boldsymbol{XBZ}$ is the expected value, $\boldsymbol{\Sigma}$ and $\boldsymbol{I}_n$ are the covariance matrices of Y_{ij} (i fixed and $j=1,...,p$) and Y_i ($i=1,...,n$), respectively. The number of time points examined on each of n observations denoted by p and $(m-1)$ is the degree of the polynomial in time.

The *OLS* estimators of parameter $\boldsymbol{B}$ and $\boldsymbol{\Sigma}$ in Equation (1) are

$$\hat{\boldsymbol{B}}_{OLS} = (\boldsymbol{X'X})^{-1}\boldsymbol{X'YZ'}(\boldsymbol{ZZ'})^{-1}$$

and

$$\hat{\boldsymbol{\Sigma}}_{OLS} = \frac{1}{\boldsymbol{n}}\left(\boldsymbol{Y}-\boldsymbol{X}\hat{\boldsymbol{B}}\boldsymbol{Z}\right)\left(\boldsymbol{Y}-\boldsymbol{X}\hat{\boldsymbol{B}}\boldsymbol{Z}\right)'.$$

$\hat{\boldsymbol{\Sigma}}_{OLS}$ is based on $\hat{\boldsymbol{B}}_{OLS}$ (Pan & Fang, 2002). Additionally, the sum of squares of residuals of the *i*th observation, which is defined as

$$e_i^2\left(\hat{\boldsymbol{B}},\hat{\boldsymbol{\Sigma}}\right)=\left(\boldsymbol{y}_i-(\boldsymbol{X}\hat{\boldsymbol{B}}\boldsymbol{Z})_i\right)'\hat{\Sigma}^{-1}\left(\boldsymbol{y}_i-(\boldsymbol{X}\hat{\boldsymbol{B}}\boldsymbol{Z})_i\right),$$

could be used to minimize

$$\sum_{i=1}^{n} w_i e_i^2 .$$

This means that the weighted covariance matrix and weighted least square (*WLS*) estimators obtained from

$$\hat{\Sigma}_{WLS} = \frac{\boldsymbol{YHY'}}{\mathrm{tr}(\boldsymbol{H})} \tag{2}$$

and

$$\hat{\boldsymbol{B}}_{WLS} = (\boldsymbol{X}'\Sigma^{-1}\boldsymbol{X})^{-1}\boldsymbol{X}'\Sigma^{-1}\boldsymbol{YWZ'}(\boldsymbol{ZWZ'})^{-1}. \tag{3}$$

Here, "tr" denotes the trace of the corresponding matrix, $\boldsymbol{H}=\boldsymbol{W}-\boldsymbol{WZ'}(\boldsymbol{ZWZ'})^{-1}\boldsymbol{ZW}$, and $\boldsymbol{W}$ is a diagonal weight matrix consisting of weights of n observations (Pendergast & Broffitt, 1985). If $1\le t\le\binom{n}{h}$ (the combination of n with h) and $h=\lfloor n/2\rfloor+\lfloor (p+1)/2\rfloor$ (the notation $\lfloor . \rfloor$ means rounding to a lower integer), the solution of the objective function

$$\min_{\hat{\boldsymbol{B}}_t}\left(\mathrm{median}(e_i^2(\hat{\boldsymbol{B}}_\ell,\hat{\boldsymbol{\Sigma}}_\ell))\right),$$

where $\ell = 1,\dots,\binom{n}{h}$ and $i = 1,\dots,n$, using Equation (2) and (3) would lead to the *LMS* estimators $\hat{\boldsymbol{\Sigma}}_{LMS} = \hat{\boldsymbol{\Sigma}}_t$ and $\hat{\boldsymbol{B}}_{LMS} = \hat{\boldsymbol{B}}_t$ (Rousseeuw & Leroy, 1987; Maronna, Martin, & Yohai, 2006). In this case, the *i*th diagonal element of the weight matrix $\boldsymbol{W}_t$ defined as

$$w_i\left(e_i^2\right) = \begin{cases} 1, & \text{if } i\text{th observation is in the } \ell\text{th combination} \\ 0, & \text{if } i\text{th observation is in the } \ell\text{th combination} \end{cases}.$$

Similarly, minimization of the objective function

$$\min_{\hat{\boldsymbol{B}}_t}\left(\sum_{i=1}^{h} e_{(i)}^2\left(\hat{\boldsymbol{B}}_\ell, \hat{\boldsymbol{\Sigma}}_\ell\right)\right),$$

where $\ell = 1,\dots,\binom{n}{h}$, $i = 1,\dots,n$, and $e_{(i)}^2$ defines the *i*th rank statistics, enables the solutions of *LTS* estimators, which are denoted by $\hat{\boldsymbol{B}}_{LTS} = \hat{\boldsymbol{B}}_t$ and $\hat{\boldsymbol{\Sigma}}_{LTS} = \hat{\boldsymbol{\Sigma}}_t$. Note that, short-term predictions are obtained from models expressed as $\hat{\boldsymbol{Y}} = \boldsymbol{X}_{5\times 2}\hat{\boldsymbol{B}}\boldsymbol{Z},$ in which $\hat{\boldsymbol{B}}$ is any estimator of $\boldsymbol{B}$.

3. Results

The first-order *GCM* is used since Turkey's wheat yield data between 2004 to 2018 by provinces are increasing in a linear form (see Figure a). Initially in this model, it should be tested that the dependent variables in Table 1 are normally distributed (hypothesis H_0). Therefore, chi-square goodness of fit test statistic

$$\sum_{t=1}^{k} \frac{(G_t - E_t)^2}{E_t^2}$$

is used to test the hypothesis H_0, which defines that *j*th $(j = 1, 2, \dots, 15)$ dependent variable is distributed normal (McCulloch, 1984). This statistic is distributed as chi-square with $(k-3)$ degrees of freedom. Where k is the number of subintervals in the domain of the random variable; G_t and E_t are the observed and expected frequencies of the *t*th class, respectively. The results of the tests carried out at type I error $\alpha = 0.05$ are summarized in Table 2.

Table 2. Chi-square goodness of fit test for dependent variables (Y_{ij}). When H_0 is rejected, the test result is set to 0, otherwise 1. $\hat{p}=P\left(\sum_{t=1}^{k}\frac{(G_t-E_t)^2}{E_t^2}>\chi_h^2\right)$ is the significance level.

Y_{ij}	Test result	$\hat{p}$	χ_h^2	$k-3$
Y_{i1}	0	0.9370	0.8108	4
Y_{i2}	0	0.5138	4.2519	5
Y_{i3}	0	0.7258	2.8323	5
Y_{i4}	0	0.1411	8.2877	5
Y_{i5}	0	0.2235	6.9620	5
Y_{i6}	0	0.9135	1.4959	5
Y_{i7}	0	0.3203	3.5035	3
Y_{i8}	0	0.8413	2.0561	5
Y_{i9}	0	0.0978	9.2977	5
Y_{i10}	0	0.7794	2.4808	4
Y_{i11}	0	0.3014	4.8657	4
Y_{i12}	0	0.3280	5.7822	5
Y_{i13}	0	0.3307	4.6014	4
Y_{i14}	0	0.0899	9.5229	5
Y_{i15}	0	0.4541	3.6593	4

The hypothesis that all dependent variables are normally distributed could not be rejected as it is demonstrated in the table. Thus, the next stage of the analyzing procedure is conducted by which the estimates of model parameters are calculated according to estimators summarized in the previous section. Hence, it is possible to make inferences about the average wheat yield in Turkey. As can be seen from Table 3 and Figure b, the estimates produce first-degree growth curve linear models that could be considered quite different from each other.

Table 3. Parameter estimations with first order *GCM*s based on *OLS*, *LMS*, and *LTS* estimators.

Model	Method	$\hat{B}_0$	$\hat{B}_1$
First order *GCM*	*OLS*	217.2182	2.4953
	LMS	227.1913	2.8008
	LTS	229.1379	2.5540

To test the significance of the model in Equation (1), i.e. testing hypothesis $H_0 : \boldsymbol{ABC} = \boldsymbol{K}$ against the alternative hypothesis $H_1 : \boldsymbol{ABC} \neq \boldsymbol{K}$, the *OLS* and robust estimators are used. For the testing procedure with *OLS* and robust estimators,

$$\frac{S_h}{S_e} \sim \left(n - r - p + m\right)^{-1} F_{1,(n-r-p+m)}$$

and

$$\frac{S_{nh}}{S_{ne}} \sim \left(n - r - p + m\right)^{-1} F_{1,(n-r-p+m)}$$

are used as test statistics, respectively. $F_{1,(n-r-p+m)}$ denotes the F distribution with $\left(1,\ n - r - p + m\right)$ degrees of freedom (Pendergast & Broffitt, 1985). Additionally,

$$S_h = (\boldsymbol{A}\hat{\boldsymbol{B}}'\boldsymbol{C} - \boldsymbol{K})'\left\{\boldsymbol{A}(\boldsymbol{ZZ}')^{-1}\boldsymbol{Z}\Delta\boldsymbol{Z}'(\boldsymbol{ZZ}')^{-1}\boldsymbol{A}'\right\}^{-1}(\boldsymbol{A}\hat{\boldsymbol{B}}'\boldsymbol{C} - \boldsymbol{K}),$$

$$S_e = \boldsymbol{C}'\left(\boldsymbol{X}'\boldsymbol{S}^{-1}\boldsymbol{X}\right)^{-1}\boldsymbol{C},\ \Delta = \boldsymbol{I} + \boldsymbol{Y}'\boldsymbol{S}^{-1}\boldsymbol{Y} - \boldsymbol{Y}'\boldsymbol{S}\boldsymbol{X}\left(\boldsymbol{X}'\boldsymbol{S}^{-1}\boldsymbol{X}\right)^{-1}\boldsymbol{X}'\boldsymbol{S}^{-1}\boldsymbol{Y},$$

$$\boldsymbol{S} = \boldsymbol{Y}(\boldsymbol{I} - \boldsymbol{Z}'(\boldsymbol{ZZ}')^{-1}\boldsymbol{Z})\boldsymbol{Y}',\ S_{nh} = (\boldsymbol{A}\hat{\boldsymbol{B}}'\boldsymbol{C} - \boldsymbol{K})'\left\{\boldsymbol{A}(\boldsymbol{ZZ}')^{-1}\boldsymbol{A}'\right\}^{-1}(\boldsymbol{A}\hat{\boldsymbol{B}}'\boldsymbol{C} - \boldsymbol{K}),$$

$$S_{ne} = \tilde{a}_0\tilde{b}_0^{-2}\boldsymbol{C}'\left(\boldsymbol{X}'\hat{\boldsymbol{\Sigma}}^{-1}\boldsymbol{X}\right)^{-1}\boldsymbol{C},\ \tilde{a}_0 = n^{-1}\sum_{i=1}^{n} w_i^2(e_i^2)e_i,$$

$$\tilde{b}_0 = n^{-1}\sum_{i=1}^{n}\left\{w_i\left(e_i^2\right)e_i + w_i\left(e_i^2\right)\right\},$$

where $\boldsymbol{I}$ denotes the $n \times n$ identity matrix, $i = 1, 2, \dots n$, and $j = 1, 2, \dots, p$. In the application $n = 79$, the number of years examined is $p = 15$, the number of classes is $r = 1$, the number of parameters in $\boldsymbol{B}$ is $m \times r = 2$. Furthermore, $\boldsymbol{C} = \begin{bmatrix} 1 \\ 0 \end{bmatrix}$ and $\boldsymbol{C} = \begin{bmatrix} 0 \\ 1 \end{bmatrix}$ is used to test $H_0 : B_0 = 0$ against the alternative hypothesis $H_1 : B_0 \neq 0$ and $H_0 : B_1 = 0$, against the alternative hypothesis $H_1 : B_1 \neq 0$, respectively. During the testing procedure $\boldsymbol{A} = 1$ and $\boldsymbol{K} = 0$.

The results, regarding the significance test of models based on *OLS*, *LMS*, and *LTS* estimators are listed in Table 4. In the tests, the critical value is $(n - r - p + m)^{-1} F_{1,(n-r-p+m)} = 0.0811$. When the hypothesis H_0 is rejected, the test results are set to '1'.

Table 4. Hypothesis tests for the model parameters. When H_0 is rejected, the test result is set to 0, otherwise 1.

Hypothesis	Method	F_h	Test result
$H_0 : B_0 = 0$	*OLS*	6.7899	1
$H_1 : B_0 \neq 0$	*LMS*	8.7083	1
	LTS	10.3387	1
$H_0 : B_1 = 0$	*OLS*	0.3167	1
$H_1 : B_1 \neq 0$	*LMS*	0.3378	1
	LTS	0.3219	1

Note that all the models seem significant. However, the estimated model based on the *OLS* estimator differs considerably from the estimated models based on robust *LMS* and *LTS* estimators. This is due to the exclusion of provinces with extremely high or extremely low wheat yields (outliers) when calculating robust estimators. The *OLS* estimator is highly influenced by the presence of such observations; therefore, the estimated models based on this estimator may not reflect the reality. Furthermore, short-term predictions with first-order *GCM*s based on this estimator vary as well. However, predictions with models based on robust *LMS* and *LTS* estimators, provide acceptable results that are closer to reality, since they are not affected by the possible effects of outlier observations.

It can be seen from the results given in Table 5 and Figure b that prediction of Turkey's wheat yield in 2024 with *OLS*, *LMS*, and *LTS* is 269.6195, 286.0077, and 282.7722, respectively. Thus, accurately determining the average wheat yield per decare would play an important role in producing better general policies to the fulfillment of needs in Turkey. For this reason, using robust estimators for making general inferences about average wheat yield provides good results, since it is not affected by outlier observations.

Table 5. Predictions of wealth yield by using first order *GCM*s based on *OLS*, *LMS*, and *LTS* estimators.

Year	*OLS*	*LMS*	*LTS*
2020	259.6383	274.8046	272.5562
2021	262.1336	277.6054	275.1102
2022	264.6289	280.4061	277.6642
2023	267.1242	283.2069	280.2182
2024	269.6195	286.0077	282.7722

If $e_i^2(\hat{\boldsymbol{B}},\hat{\Sigma}) > \chi^2_{(p-1),1-\alpha/2}$ then the ith observation is evaluated as an outlier. Here, $e_i^2(\hat{\boldsymbol{B}},\hat{\boldsymbol{S}}) = \left(\boldsymbol{y}_i - (\boldsymbol{X}\hat{\boldsymbol{B}}\boldsymbol{Z})_i\right)'\hat{\Sigma}^{-1}\left(\boldsymbol{y}_i - (\boldsymbol{X}\hat{\boldsymbol{B}}\boldsymbol{Z})_i\right)$ denotes the sum of the squared residual of the ith observation and is computed for *OLS, LMS*, and *LTS* estimators, separately (Rousseeuw & Leroy, 1987). The results regarding with the detected outliers are given in Table 6.

Table 6. Detected outliers

Estimators	Outlier observation (province) number									
OLS	15	17	43	52	59	65				
LMS	15	17	25	29	30	34	43	44	52	59
LTS	10	15	17	22	43	44	52	59		

Among the outliers determined through robust *LMS* and *LTS* estimators, there are observations with low and high wheat yield. Some observations vary widely (in terms of increase or decrease) over the years as well. Thus, by excluding the outliers from the process of calculating these estimators, their possible negative effects were avoided.

Otherwise, as in *OLS*, since all observations are given equal weight, the average yield will be underestimated due to the provinces with low wheat yield (see Figure b). The *OLS* estimator has been heavily influenced by provinces with low wheat yield. Although high wheat yield provinces masked the effect of these provinces on the *OLS* estimations, this masking did not prevent them from being detected as outliers.

4. Discussion

In this study, Turkey's average wheat yield has been analyzed with linear first-order GCMs. The models are obtained by applying robust *LMS* and *LTS* estimators and a non-robust *OLS* estimator. Using disparate estimators allowed remarking the differences in parameter estimations and short-term predictions for average wheat yield per decare, (see Table 5 and Figure b, respectively). A legitimate clarification for them seems to be the existence of outliers in the data. Outliers, usually impact the analysis procedures. The predictions that are least affected by the outliers were obtained from the *LMS* and *LTS* estimators. These predictions demonstrated that the values of average wheat yield in Turkey will continue to increase, and at the end of 2024 it will be exceeding 280 kg per decare.

REFERENCES

Bell, M. A., & Fischer, R.A. (1994). Using yield prediction models to assess yield gains: a case study for wheat. *Field Crops Research, 36*(2), 161-166. doi:10.1016/0378-4290(94)90064-7.

Cook, R. D. (1977). Detection of influential observation in linear regression. *Technometrics, 19*(1), 15-18. doi: 10.1080/00401706.1977.10489493.

Cook, R. D., & Weisberg, S. (1982). *Residuals and influence in regression*. New York, USA: Chapman & Hall.

Dahikar, S. S., & Rode, S. V. (2014). Agricultural crop yield prediction using artificial neural network approach. *International Journal of Innovative Research in Electrical, Electronics, Instrumentation and Control Engineering, 2*(1), 683-686. doi: 10.1.1.429.1195&rep=rep1&type=pdf.

Hampel, F. R., Ronchetti, E. M., Rousseeuw, P. J., & Stahel, W. A. (1986). *Robust statistics: The approach based on influence functions*. New York, USA: John Wiley & Sons.

Huber, P. J. (1981). *Robust statistics*. New York, USA: Wiley Series in Probability & Statistics.

Maronna, R. A., Martin, D. R., & Yohai, V. J. (2006). *Robust statistics theory and methods*. New York, USA: John Wiley & Sons.

McCulloch, C. E. (1984). Relationships among some chi-square goodness of fit statistics. *Communications in StatisticsTheory and Methods, 14*(3), 593-603. doi: 10.1080/03610928508828936.

Pan, J. X., & Fang, K. T. (2002). *Growth curve models and statistical diagnostics.* New York, USA: Springer-Verlag.

Pantazi, X. E., Moshou, D., Alexandridis, T., Whetton, R. L., & Mouazen, A. M. (2016). Wheat yield prediction using machine learning and advanced sensing techniques. *Computers and Electronics in Agriculture, 121*, 57-65. doi: 10.1016/j.compag.2015.11.018.

Pendergast, J. F., & Broffitt, J. D. (1985). Robust estimation in growth curve models. *Communications in StatisticsTheory and Methods 14*(8), 1919-1939. doi: 10.1080/03610928508829021.

Rousseeuw, P. J., & Leroy, A. M. (1987). *Robust regression and outlier detection*. New York, USA: Wiley.

Şimşek, O., Mermer, A., Yıldız, H., Özaydın, K. A., & Çakmak, B. (2007). Agrometshell modeli kullanılarak Türkiye'de buğdayın verim tahmini. *Tarım Bilimleri Dergisi*, *13*(3), 299-307.

Turkish Statistical Institute. (2018). Statistics by Theme, Databases, Retrieved from https://biruni.tuik.gov.tr/medas/?kn=92&locale=tr

Chapter 5

DIURNAL, TEMPORAL, ANNUAL AND GEOGRAPHICAL VARIATIONS AND CORRELATIONS IN CARBON MONOXIDE AND BENZENE EMISSIONS IN NORTH CYPRUS

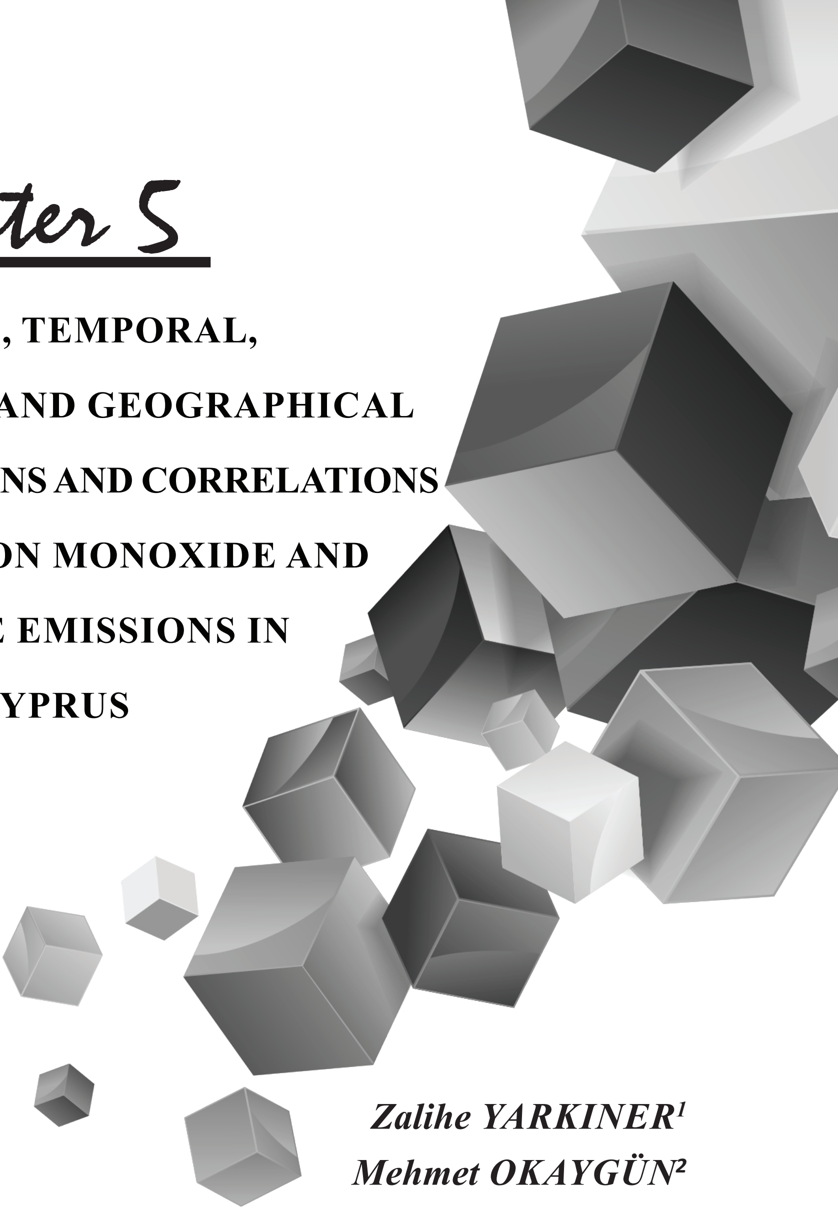

Zalihe YARKINER[1]
Mehmet OKAYGÜN[2]

---

[1] Assist. Prof. Dr. Faculty of Engineering, Department of Software Engineering, Cyprus Science University, Cyprus, zaliheyarkiner@csu.edu.tr, 0000-0002-4766-6454

[2] Assist. Prof. Dr. Levent College, Nicosia, mehmetokaygun14@gmail.com, 0000-0001-9313-358X

1. INTRODUCTION

Carbon monoxide (CO) and benzene are two of the most common and widely distributed air pollutants. CO emission sources can be both natural and anthropogenic. Natural emissions of CO are mainly due to oxidation of methane gas produced from decaying vegetation whereas anthropogenic emissions include transportation, fuel combustion in stationary and mobile sources, industrial processes, solid waste disposal activities, forest fires and agricultural burning. Exhaust gases discharged from diesel and gasoline internal combustion engines represent the highest fraction of anthropogenic emissions (Peavy et al., 1985). Natural levels of CO range in the atmosphere between 0.06-0.14 mg/m^3. However, in closed public areas like car parks and road tunnels where combustion engines are used without enough ventilation, CO concentrations may peak up to above 115 mg/m^3 . In homes with gas appliances in use, peak CO concentrations may go up to 60-115 mg/m^3. In residential areas, offices, restaurants and vehicles, tobacco smoke may raise the 8-hr average CO concentration to 23-46 mg/m^3 (World Health Organisation, 2000a). Carbon monoxide at natural atmospheric levels has negligible effect, but at higher concentrations, can seriously affect human aerobic metabolism since the affinity of haemoglobin (Hb) is 200-250 times higher for CO than that for oxygen gas, as in cases of occupational exposure to indoor exhaust emissions (Topacoglu et al., 2016). Higher CO concentrations can also cause asthma in young people who reside at close proximity to a main road as detected in Nicosia (Middleton et al., 2010). CO reacts readily with Hb in the blood to produce carboxyhaemoglobin (COHb) and reduces the blood's capacity to carry oxygen (Sheps et al., 1987). Based on medical studies, during exposure to a fixed concentration of CO, the COHb in the blood increases rapidly at the start, starts to level off after three hours and reaches a steady concentration after 6-8 hours of exposure: at levels less than 1% COHb no physilogical changes are observed, at levels between 1-5% central nervous system and behavioral performance are affected, at levels above 5% cardiac and pulmonary functional changes take place, and at levels above 10% headaches, fatigue, drowsiness, coma, respiratory failure and death may result (Wolf, 1971; Adams et al., 1988). A person trapped in traffic at a street-crossing site where the CO concentration can reach to 48 mg/m^3, with one hour exposure, may develop changes in central nervous system such as impairment in time-interval and brightness discrimination (US Environmental Protection Agency, 1991; Peavy et al., 1985; Wolf, 1971). The maximum limit exposure value set for the eight-hour rolling average CO concentration in air is 10 mg/m^3 as given in the Directive of the Europoean Parliment for Air Quality, whereas the upper and lower assessment threshold values are 7 mg/m^3 and 5 mg/m^3, respectively (Directive 2008/50/EC of the European Parliament and of the Council, 2008) .

Benzene (C_6H_6) is one of the most important air-polluting chemicals belonging to the main group Volatile Organic Compounds (VOCs). VOCs are chemical substances that either exist as gases or may be easily transferred from the liquid to the gaseous state due to their low boiling points. Benzene is volatile and it can quickly evaporate into air in which its vapor is heavier than air allowing it to sink into low-lying areas. Benzene presents a dangerous fire hazard when exposed to heat or flame due to its flammability (CRC Handbook of Chemistry, 2005) and is primarily used as a reagent in the production of various substances and is found in crude oil at levels up to 4 g/l (International Program on Chemical Safety, 1993). At ground level VOCs including benzene react with other air pollutants and contribute to the formation of potentially harmful ozone gas in the lower atmosphere. Benzene is used as a gasoline additive so it is released to the environment from vehicle emissions, evaporation of petrol during vehicle fueling, fuel tanks, processes where it is used as a chemical reagent or intermediate and from other fossil fuel combustion processes (World Health Organisation, 2000b). Benzene, which also exists in cigarette smoke, is a known human carcinogen and its inhalation is the dominant pathway for exposure in humans. The in-vivo data collected for benzene indicates that it is mutagenic (Paxton et al.,1994). Mean ambient air concentrations of benzene in rural and urban areas are about 1 $\mu g/m^3$ and 5-20 $\mu g/m^3$, respectively. Indoor and outdoor benzene emission levels are higher near sources such as fuel filling stations (World Health Organisation, 2000b). The maximum limit exposure value set for the annual average benzene concentration in air is 5 $\mu g/m^3$ as given by the Directive of the Europoean Parliment for air quality, whereas the upper and lower assessment threshold values are 3.5 $\mu g/m^3$ and 2 $\mu g/m^3$, respectively (Directive 2008/50/EC of the European Parliament and of the Council, 2008).

Atmospheric observations of CO and fossil fuel carbon dioxide (CO_2) emissions were made in East Asia (Turnbull et al., 2011) and the results indicated a 63% increase in Chinese emissions from 2004 to 2010. Revokatova proposed a method of operational forecast of CO distribution in Moscow based on the concentration and distribution of its sources by using a chemistry transport model (Revokatova, 2013). Global estimates of the monthly nation-level CO emissions were made from 79 major sources in China from 1960 to 2013 and an inventory with high spatial resolution was built up (Zhong et al., 2017). Seasonal, diurnal and weekend trends in black carbon emissions and CO pollutants were studied and determined for Mexico City (Retama et al., 2015) and it was concluded that their maximum concentration values were significantly less in the rainy seasons compared to the dry seasons; the weekend effects were also observed and linked to the changes in traffic patterns and type of fuels burned. Another study showed that a rough increase of 10% is expected in surface CO levels by 2050 over the Eastern Mediterrenean indicating future temporal variations in CO emissions (Myriokefalitakis et al., 2015). It was reported that the oxidation of methane and non-methane hydrocarbons and direct emissions from burning biomass and human activities involving fossil fuel and biofuel were the major sources of CO in the atmosphere (Duncan et al., 2007). Another source characterization study of tropospheric CO and O_3 over the Northwestern Pacific was performed in summer 2012 (Park and Rhee, 2012) and positive correlations between CO and O_3 were observed. The emissions in Turkey were determined to be lower than the average European emissions including CO and VOCs on the basis of unit geographic land area or per capita (Elbir et al., 2000). A spatially allocated emissions inventory was developed for the Southern Cyprus and it was determined that the road transport had a share of 48% in total non-methane VOC emissions and 78% in total CO emissions (Tsilingiridis et al., 2010). The origin and variability of sixty C2-C16 VOCs were observed at the Cyprus Atmospheric Observatory site in 2015; it was determined that the biogenic VOCs were emitted from local origins whereas the anthropogenic and oxygenated VOC emissions were attributed to long range transport from Western Asia displaying higher mixing ratios under the influence of continental air masses (Debevec et al., 2017). Efforts were continued to model the atmospheric composition over Cyprus; in such a study, Kushta et al. used a meteorological and chemical transport model and obtained reasonable results when the boundary conditions were cautiously adjusted and they concluded that there was a further need to pursue a high-resolution local emission inventory for Cyprus (Kushta et al., 2016). The relation of particulate matter emissions with CO pollution was also studied: the highest ratio of particulate matter with size 2.5 µm ($PM_{2.5}$) to 10 µm (PM_{10}) was shown to coincide with the highest concentrations of CO and NO_x indicating predominant emissions from anthropogenic sources (Yadav et al., 2017) in India. The observed reduction in ozone peak concentrations in some Mediterranean cities were attributed to a decrase in the NO_x and VOC concentrations (Sicard et al., 2013). It was shown that there were seasonal variations in VOC emissions in Paris with largest contribution of 25% coming from the traffic related activities and the significant contribution from wood-burning, especially in winter, could represent up to approximately 50% of the total mass of VOCs emitted (Baudic et al., 2016). On the other hand, Salameh et al. studied and concluded that there was generally no significant seasonality in emission ratios of VOCs in the Eastern Mediterranean basin unlike the seasonality observed in other cities, and the transport sector was the major source of 80% of VOC emissions (Salameh et al., 2016). In another study, the occupational VOC exposures in a petrol station were studied. Kountouriotis et al. numerically simulated the spatial distribution of various VOCs leaking to the atmosphere in the working area of a petrol station and showed that there will be always spaces in the station, above the source of the leak, where the concentration of VOC vapor is much higher than the recommended exposure limit (Kountouriotis et al., 2014).

Based on the previous studies, it can be observed that the amount of CO and VOCs emissions depend on geographical location, population estimates, surface emission inventories, geographical air mass movements and technologies currently used at urban sites. It can also be concluded that these emissions are showing diurnal, seasonal and temporal variations, neglecting exceptional cases. Under conditions of growing population and industry, and increasing traffic, people living in North Cyprus are currently more likely to be exposed to higher concentrations of CO and VOCs emissions. Therefore it is necessary to use the ground measurements of CO and VOCs emission levels in North Cyprus to determine whether there are any diurnal, seasonal and temporal variations within and between the years and the locations, assessing if there are any health risks of exposure to the observed levels of pollutant gas emissions.

2. MATERIALS AND METHODS

2.1. Geographical locations

North Cyprus is an island with an area 3355 km^2. Out of many regions in North Cyprus, the three major cities with high urban populations are Nicosia, Famagusta and Kyrenia as shown in Fig.1. Nicosia is the capital of Cyprus and is located in the Mesoria plain, which lies in the centre of the island, between the Kyrenia Mountains in the north and the Troodos Mountains in the south. The most prominent feature of North Cyprus is the northern range of mountains, known as the Kyrenia Mountains or Five Finger Mountains. This range of mountains is narrow, approximately 130 km long, running parallel to the north coastline. Kyrenia is located at the north coast and is separated from Nicosia by the Five Finger Mountains, with a planar distance of 19 km from Nicosia. On the other hand, Famagusta is located on the east coast of the Mesoria plain, with a planar distance of 52 km from Nicosia. The highest planar distance between any two cities in the north part of the island, 61 km, lies between Kyrenia and Famagusta. These two cities are located in opposite directions and are separated by the Five Finger Mountains. Table 1 shows the altitudes of these cities above the sea level and the defacto population census results of 2011 with the projected population counts for 2013 and 2016 (TRNC State Planning Organisation, 2011). Geographical locations of these cities, with other major urban populated areas in Cyprus are displayed in Fig.1.

Fig. 1. *Major urban population areas in Cyprus.*

Table 1. *Altitudes and populations of three major cities in North Cyprus.*

City	Altitude (Km)	Population (2011)	Population Projected (2013)	Population Projected (2016)
Nicosia	149	97,293	101,485	112,454
Famagusta	14	69838	74,640	82,707
Kyrenia	42	73577	74,021	82,022

Nicosia is an inland city whereas Famagusta and Kyrenia are both coastal cities, as shown in Fig. 1. Nicosia, as a capital, keeps growing both in population and terrestial area, with increasing number of administrative and industrial activities, and opening of new universities. Kyrenia and Famagusta both, having all the same developments, are hosting many touristic resort places that cause the population to grow even more compared to Nicosia. So, as a result, it is very usual to observe increasing traffic in all three cities with higher consumption of gasoline and diesel in car engines, higher use of solvents in industry and, increasing number of burning activities of fuels like kerosene and wood for household heating in winter period. In order to measure the existing air pollution levels emitted from all these activities, data were collected from the air qulity measuring stations at the centre of these three cities, especially located in areas with heavy traffic loads.

2.2. Measurement Devices and Methods

Latitude and longitude values of the meteorological stations used for air pollution measurements in Nicosia, Famagusta and Kyrenia are shown in Table 2. Data measurements for CO and benzene on an hourly basis were performed through the years 2011-2016 in these cities. CO concentrations were calculated and reported as eight-hour running averages using the hourly data, updating the eight-hour running average for each hour (Directive 2008/50/EC of the European Parliament and of the Council, 2008). The monthly and annual arithmetic mean emission CO concentrations were calculated by using the daily values that were obtained from the eight-hour running average values. On the other hand, the daily, monthly and annual benzene concentrations were directly determined by using the arithmetic averages obtained from hourly benzene measurements, as described in the European Directive (Directive 2008/50/EC of the European Parliament and of the Council, 2008). The analytical instruments used for CO and benzene measurements are listed in Table 2. Benzene and CO values were measured in units of µg/m^3 and mg/m^3, respectively.

Table 2. Geographical location of the meteorological stations and the analytical instruments used in each station.

Location	Latitude	Longitude	CO Measurement Device	Benzene Measurement Device
Nicosia	35,19416	33,34854	Ecotech Model 9830	Syntech Spectras GC955
Famagusta	35,13031	33,92765	Environment S.A. Model CO12M	Syntech Spectras GC955
Kyrenia	35,33251	33,31500	Environment S.A. Model CO12M	Syntech Spectras GC955

Benzene measurements in all stations were obtained by using the Syntech Spectras GC955-600 BTX gas chromatograph analyzer. This instrument is especially designed and used for the measurement of benzene, toluene and xylene isomers in ambient air. It has a built-in pre-concentration system: the hydrocarbons are pre-concentrated on Tenax GR adsorbent resin, then desorbed in a thermic manner and separated on an EPA624 equivalent column. The final analysis is performed by using a photo ionization detector that has the lowest detection level 0.1µg/m^3 (0.03 pbb) for benzene and a measurement range of 300 ppb benzene in ambient air. CO measurements in Famagusta and Kyrenia were reported by using the Infra-Red Gas Filter Correlation Carbon Monoxide Analyzer CO12M, based on absorption photometry combined with gas filter correlation. This instrument has a range of 200 ppm for CO and the lowest detectable limit 40 ppb CO with the noise level 20 ppb. CO measurements in Nicosia were conducted by using the Ecotech Model 9830 CO analyzer that uses the gas filter correlation technology with infra-red photometric detection. Even though this instrument is an older model of CO12M analyzer it uses a microprocessor control to measure CO in the range 0-200 ppm with the lowest detection limit 50 ppb.

3. ANALYSES AND RESULTS

3.1. Daily CO and Benzene Fluctuations

The daily mean emission concentrations of CO were calculated by using the eight-hour running average values (obtained from the hourly base emission values) and the daily average emission concentrations of benzene were calculated by using the hourly base emission values. These daily average emissions of CO and benzene were plotted versus time between 2011 and 2016 in Fig. 2 by using a dual-axis plot. This plot showed the scattering of data values for both CO and benzene emissions within given time period; a close observation of Fig. 2 reveals the temporal variations in benzene emissions with seasonal cycles. To gain more insight into both data sets, the same daily average emissions of CO and benzene were separately plotted versus time for each year between 2011-2016 in Figures 3 and 4, respectively. In these plots, day 1 indicates the first measurement value reported as of 1st of January and day 365 indicates the last measurement value reported as of 31st of December for that given year. Fig.3 clearly shows that when CO emissions are compared between the years within the specific station, in stations such as Kyrenia and Famagusta, they were higher in the early years (2011 and 2012) and were lower in the following years (2013-2016). Even though there were temporal variations in CO emissions for both Kyrenia and Famagusta, with a decreasing trend, it was very difficult to conclude about any seasonal trends during the period 2011-2016 in both cities. The data set for CO emissions in Nicosia was not complete; emissions for 2014 and 2015 had missing values and in 2016 emission values could not be measured due to problems experienced with the analytical instrument. However, the investigation of available CO emissions data in Nicosia throughout the years 2011-2016, in Fig.3, showed that there were temporal variations but with no trends and Nicosia was the most polluted among the three cities. The decreasing trends observed in Kyrenia and Famagusta CO emissions, after 2012, could be attributed to improved exhaust technologies used in automobile designs since Table 2 shows that the populations of both cities were expected to have increased in between 2011-2016. Until now, no emission inventories have been prepared for North Cyprus, but due to the increasing industrial activities, heavy traffic and fuel burning for household heating, the inventories of emissions from air pollutants are expected to increase and hence the emissions of CO are expected to rise as well. Nonetheless, the observed decreasing trends in CO emissions in Kyrenia and Famagusta were attributed to the use of newer exhaust technologies. One major observation that needs to be well underlined is that in all measurements made throughout the whole period in all cities, the CO emissions were under the limit value set for the eight hour running average, 10 mg/m^3 set for CO exposure, as outlined in the European Directives (Directive 2008/50/EC of the European Parliament and of the Council, 2008) .

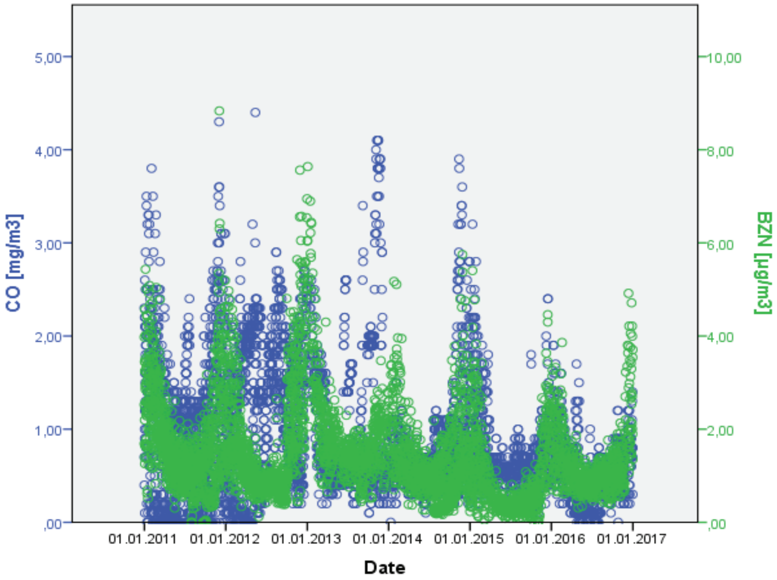

Fig. 2. Dual y axes with scale x axis of CO and benzene emission levels by date for the years in between 2011-2016.

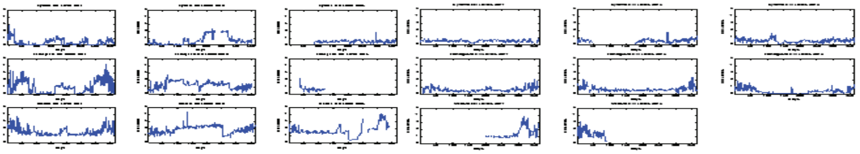

Fig. 3. Daily fluctuations in CO emissions in between 2011-2016 for each station.

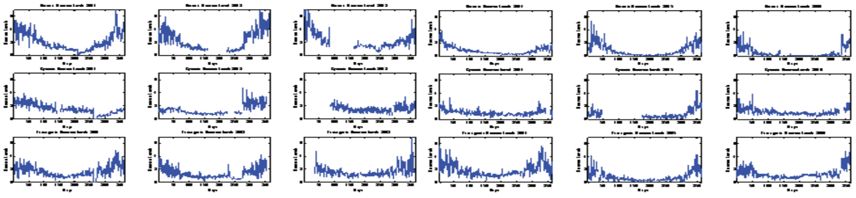

Fig. 4. Daily fluctuations in benzene emissions in between 2011-2016 for each station.

Fig. 4 shows the daily fluctuations of benzene in between 2011-2016. This figure depicts the presence of temporal variations in benzene emissions with seasonal trends in all stations. Throughout the whole years, the benzene emissions tend to be lower in spring and summer seasons than fall and winter periods. The major reason explaining this is having more burning activities for household heating in winter time in North Cyprus resulting in higher benzene emissions than in spring and summer seasons. All of the calculated daily benzene emission levels in Famagusta and Kyrenia, in between 2011-2016 (Fig. 4), were determined to be less than 5 μg/m^3 (the exposure limit set for the annual average benzene concentration in air by the European guidelines). Though, some of the daily benzene emission levels in Nicosia, observed in some winter months in between 2011-2013 (Fig. 4), were determined to be close or above the 5 μg/m^3 limit, indicating possible threats to human health and making necessary to more closely investigate the hourly diurnal benzene emissions, as outlined in section 3.3. In overall, it was concluded that we had temporal variations in CO and benzene emissions in all cities in North Cyprus in between 2011-2016, with seasonal cycles for benzene emissions.

3.2. Annual Changes in CO and Benzene Emission Levels in North Cyprus

3.2.1. Descriptive Analyses

Figures 3 and 4 depicted that there were temporal fluctuations in the daily average values of CO and benzene emissions in between 2011-2016 with respect to years and location. These observations urged us to perform further statistical analyses, both descriptive and inferential, in order to determine any annual and geographical variations and trends in CO and benzene emissions in North Cyprus. The annual averages were estimated for both CO and benzene emissions as described in section 2.2. The descriptive statistical analyses were performed to summarize and provide information about the data, and describe basic features in the research dataset. Descriptive information for annual CO and benzene emission levels for each year in between 2011-2016 for each city Kyrenia, Famagusta and Nicosia are provided in Table 3. Graphical representations of the mean CO and mean benzene emission levels at each year for each station are displaced in Figures 5 and 6, respectively.

Table 3. Descriptive statistics of annual CO and benzene emission levels in each year from 2011 to 2016 for each city

	2011		**2012**		**2013**		**2014**		**2015**		**2016**	
	CO	BNZ	CO	BNZ	CO	BNZ	CO	BNZ	CO	BNZ	CO	BNZ
Kyrenia												
Mean	0.3948	1.512904	0.6527	1.370689	0.5250	1.547899	0.5591	1.029727	0.5922	0.812796	0.5723	1.151791
Mode	0.00	0.00	0.10	0.8542	0.50	1.6833	0.60	0.5	0.60	0.3583	0.50	0.9542
Median	0.3	1.447917	0.5	1.091667	0.50	1.481250	0.60	0.937500	0.60	0.583333	0.60	1.033333
St.Deviation	0.43740	0.7604241	0.65070	0.7512979	0.18466	0.4870180	0.15648	0.4252362	0.23564	0.6697016	0.25718	0.5039668
Variance	0.191	0.578	0.423	0.564	0.034	0.237	0.024	0.181	0.056	0.449	0.066	0.254
Minumum	0.00	0.00	0.00	0.4958	0.10	0.5167	0.10	0.2625	0.10	0.00	0.10	0.4167
Maximum	2.90	3.9250	2.30	4.8067	1.90	3.4708	1.00	3.3583	1.80	4.4583	1.70	3.8615
Famagusta												
Mean	0.9742	1.597634	1.3324	1.313753	0.7078	1.583485	0.6610	1.818215	0.7222	0.823250	0.4373	1.346188
Mode	0.00	0.00	1.50	0.6458	0.60	1.5375	0.50	1.3375	0.60	0.5250	0.10	0.5958
Median	0.80	1.383333	1.40	1.056250	0.70	1.385417	0.60	1.537500	0.60	0.5250	0.40	1.112500
St.Deviation	0.87225	0.8551183	0.48950	0.7884044	0.26658	0.7965937	0.29989	0.9492773	0.32217	0.7416728	0.37972	0.8033269
Variance	0.761	0.731	0.240	0.622	0.071	0.635	0.090	0.901	0.104	0.550	0.144	0.645
Minumum	0.00	0.00	0.20	0.1208	0.20	0.4708	0.00	0.2625	0.10	0.00	0.00	0.3083
Maximum	4.30	4.9375	2.80	4.2583	2.20	7.6625	2.10	5.75	2.40	4.30	1.90	4.9167
Nicosia												
Mean	1.5613	2.040120	1.9044	2.380532	1.7174	2.180920	1.4981	0.850913	1.4310	0.86140	N/A	0.503874
Mode	1.10	0.00	2.30	0.6417	1.40	1.3542	1.00	0.2583	1.40	0.1375	N/A	0.00
Median	1.40	1.637500	2.00	1.812500	1.60	1.733333	1.10	0.662500	1.40	0.479167	N/A	0.152174
St.Deviation	0.55928	1.3233671	0.50918	1.545289	0.78031	1.2233849	0.75669	0.6083864	0.57161	0.9156533	N/A	0.7453068
Variance	0.313	1.751	0.259	2.388	0.609	1.497	0.573	0.370	0.327	0.857	N/A	0.555
Minumum	0.90	0.00	0.70	0.4083	0.30	0.4458	0.80	0.1667	0.30	0.0083	N/A	0.00
Maximum	3.80	8.8333	4.40	7.5625	4.10	7.6375	3.90	3.9583	3.20	5.4042	N/A	3.7875

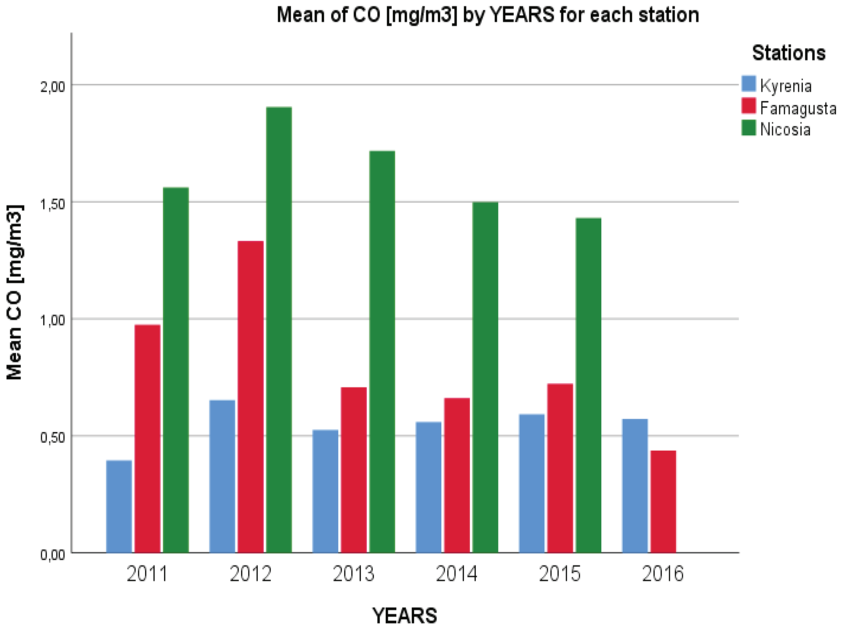

Fig. 5. Mean CO emission levels by years for each station from 2011-2016

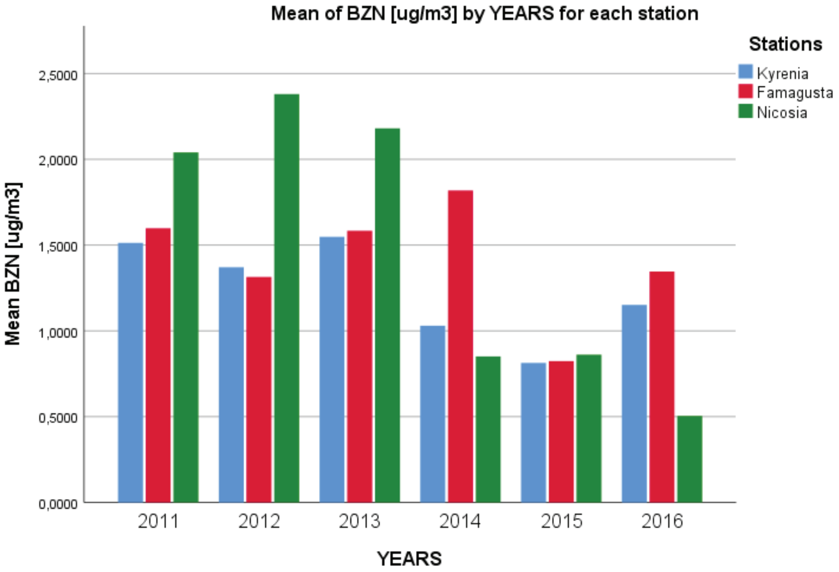

Fig. 6. Mean benzene emission levels by years for each station from 2011-2016

From Table 3 and Figure 5 it can be seen that numerically the highest CO emission levels were measured in all stations at 2012 throughout the years from 2011 to 2016. Comparing the mean CO emission levels in 2012 between the stations indicates that the lowest mean value was achieved in Kyrenia whereas the highest standard deviation, showing the highest variability between the CO measurements, was also obtained in Kyrenia. Figure 5 and Table 3 show that the highest mean CO emission levels throughout all the years from 2011 to 2016 were observed in Nicosia. Kyrenia station at 2012, having a population sample (N) 332, was associated with a mean (M) CO emission level of 0.6527 mg/m^3 and a standard deviation (SD) of 0.65070 mg/m^3. While Famagusta station at 2012 (N=349) was associated with CO emission level M=1.3324 mg/m^3 (SD=0.48950 mg/m^3), Nicosia station at 2012 (N=362) was associated with CO emission level M=1.9044 mg/m^3 (SD=0.50918 mg/m^3). Through investigation of data from Table 3 and Figure 6 for the mean benzene emission levels for each station for each year, numerically the highest benzene emission levels were observed in Nicosia at 2012, in Kyrenia at 2013 and in Famagusta at 2014, respectively.

3.2.2. Inferential Analyses on Temporal Variations In Annual Mean CO And Benzene Emissions

From Figures 5 and 6, after observing that the mean CO and benzene emission levels for each station were numerically different throughout the six years between 2011 and 2016, it was necessary to test the hypothesis whether or not within each station two consecutive years were associated with statistically significant different mean CO and benzene emission levels. Accordingly, the independent samples t-tests were performed for the data and the results were given in Table 4.

Table 4. Independent samples t-test for the equality of variances and equality of means of CO and benzene emission levels between the years within each station

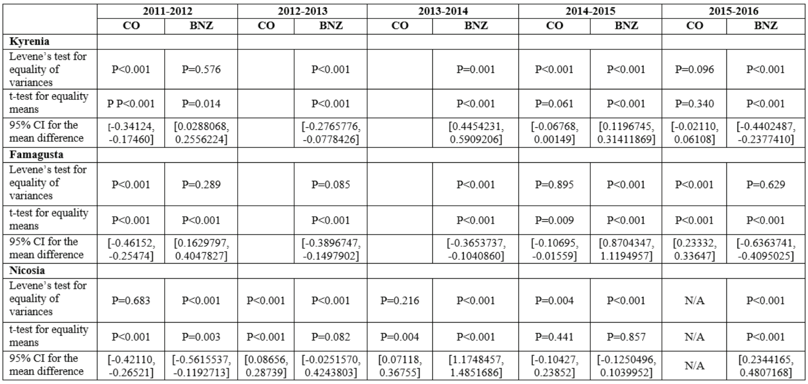

	2011-2012		2012-2013		2013-2014		2014-2015		2015-2016	
	CO	BNZ	CO	BNZ	CO	BNZ	CO	BNZ	CO	BNZ
Kyrenia										
Levene's test for equality of variances	P<0.001	P=0.576		P<0.001		P=0.001	P<0.001	P<0.001	P=0.096	P<0.001
t-test for equality means	P P<0.001	P=0.014		P<0.001		P<0.001	P=0.061	P<0.001	P=0.340	P<0.001
95% CI for the mean difference	[-0.34124, -0.17460]	[0.0288068, 0.2556224]		[-0.2765776, -0.0778426]		[0.4454231, 0.5909206]	[-0.06768, 0.00149]	[0.1196745, 0.31411869]	[-0.02110, 0.06108]	[-0.4402487, -0.2377410]
Famagusta										
Levene's test for equality of variances	P<0.001	P=0.289		P=0.085		P<0.001	P=0.895	P<0.001	P<0.001	P=0.629
t-test for equality means	P<0.001	P<0.001		P<0.001		P<0.001	P=0.009	P<0.001	P<0.001	P<0.001
95% CI for the mean difference	[-0.46152, -0.25474]	[0.1629797, 0.4047827]		[-0.3896747, -0.1497902]		[-0.3653737, -0.1040860]	[-0.10695, -0.01559]	[0.8704347, 1.1194957]	[0.23332, 0.33647]	[-0.6363741, -0.4095025]
Nicosia										
Levene's test for equality of variances	P=0.683	P<0.001	P<0.001	P<0.001	P=0.216	P<0.001	P=0.004	P<0.001	N/A	P<0.001
t-test for equality means	P<0.001	P=0.003	P<0.001	P=0.082	P=0.004	P<0.001	P=0.441	P=0.857	N/A	P<0.001
95% CI for the mean difference	[-0.42110, -0.26521]	[-0.5615537, -0.1192713]	[0.08656, 0.28739]	[-0.0251570, 0.4243803]	[0.07118, 0.36755]	[1.1748457, 1.4851686]	[-0.10427, 0.23852]	[-0.1250496, 0.1039952]	N/A	[0.2344165, 0.4807168]

3.2.2.1. Kyrenia Station

In Kyrenia station, since numerically the highest CO emission level was observed in 2012 over the six years from 2011 to 2016, only those comparisons from 2011 to 2012 and from 2012 to 2013 were discussed in detail below among all the results of independent samples t-test given in Table 4. In Kyrenia station, at 2011 and 2012, the CO emission level distributions were sufficiently normal for the purpose of conducting a t-test (skewness<|2.0| and kurtosis<|9.0|; (Schmider et al., 2010). Additionally, the assumption of homogeneity of variances was tested and found that variances between CO emission levels in Kyrenia station at 2011 and at 2012 were not assumed to be equal via Levene's F-test, F(695)=44.50, p<0.001. The independent samples t-test was associated with a statistically significant effect, t (571.249) =-6.080, p<0.001. Thus, in Kyrenia, the CO emission levels in 2011 were associated with a statistically significant different mean than 2012. Cohen's d was estimated at -0.51, indicating a medium effect based on Cohen's guidelines (Cohen J. 1988; Cohen J., 1992). In Kyrenia station at 2013 even the skewness<|2|, the kurtosis was calculated to be greater than 9.0, therefore CO emission levels were determined not to be normally distributed and hence t-test could not be conducted for Kyrenia at 2013 to check any changes between 2012-13 and between 2013-14. It can be verified from Table 4, that in Kyrenia, in the last three years from 2014 to 2016, the mean differences of CO emissions were not statistically significant (p=0.061 for 2014-2015 test and p=0.340 for 2015-2016).

In Kyrenia, since numerically the highest benzene emissions were reported in 2013 over the six years from 2011 to 2016, from the results of independent samples t-test given in Table 4, only the comparisons from 2012 to 2013 and from 2013 to 2014 were elaborated below in detail. In Kyrenia at 2012 and at 2013 benzene emissions were sufficiently normal for the purpose of conducting a t-test and the variances between benzene emission levels in Kyrenia station at 2012 and at 2013 were not assumed to be equal via Levene's F-test, F(606)=26.227, p<0.001. The independent samples t-test was associated with a statistically significant effect, t (573.747) =-3.503, p<0.001. Thus, in Kyrenia station, benzene emission levels for 2012 were associated with a statistically significant different mean than 2013. Cohen's d was estimated at -0.29, which corresponded to a small effect. In Kyrenia station at 2013 and at 2014 benzene emissions were also found to be normally distributed and that variances between benzene emission levels in Kyrenia station at 2013 and at 2014 were not assumed to be equal via Levene's F-test, F(627)=12.038, p=0.001. The independent samples t-test was associated with a statistically significant effect, t (548.342) =13.991, p<0.001. Thus, in Kyrenia station, benzene emission levels for 2013 were associated with a statistically significant different mean than for 2014. Cohen's d was estimated at 1.19 which indicated a very large effect. From the results of Table 4, starting from 2011, in the first three years, changes in the mean benzene emissions in both directions were observed; decreasing (Cohen's d=0.19) change from 2011 to 2012 and increasing change (Cohen's d=-0.29) from 2012 to 2013, in the mean benzene concentrations were estimated to be small effects, respectively. However, in Kyrenia the peak benzene emissions were obtained in 2013 and a very large decreasing effect was found when observing the difference of mean benzene emissions between 2013 and 2014. After this large effect, in the last 3 years from 2014 to 2016, fluctuations in benzene emission levels (decreasing effect from 2014 to 2015 with Cohen's d=0.47 and increasing effect from 2015 to 2016 with Cohen's d=-0.66) were observed with medium effect in both directions.

3.2.2.2. Famagusta Station

In Famagusta, the highest emission levels were observed in 2012 over the 6 years as like in Kyrenia. Therefore, inferences about the CO emissions are discussed in detail from 2011 to 2012 and from 2012 to 2013 while the information about the other years is summarized in Table 4. In Famagusta, at 2011 and at 2012, the CO emission distributions were sufficiently normal for the purpose of conducting a t-test. The assumption of homogeneity of variances was tested and was found that the variances between the CO emission levels in Famagusta station at 2011 and 2012 were not assumed to be equal via Levene's F-test, $F(712)=120.134$, $p<0.001$. The independent samples t-test was associated with a statistically significant effect, $t\ (577.718) = -6.803$, $p<0.001$. Thus, in Famagusta, the mean CO emission levels for 2011 were found to be significantly different than the mean values in 2012 with estimated Cohen's d at -0.57, showing a medium increasing effect from 2011 to 2012. In Famagusta station, at 2013 even the skewness<|2|, the kurtosis was found to be greater than 9.0, therefore CO emission levels were found not to be normal and hence t-test could not be conducted for Famagusta station between 2012-2013 and 2013-2014. From these results, it was concluded that the mean differences of CO emission levels between the years in Famagusta station were statistically significant, initiating a medium amount of increase in the CO emission levels in 2012 compared to 2011 in the earlier years (i.e. Cohen's d=-0.57 for 2011-2012), causing a small increase in the amount of CO emission levels in 2015 compared to 2014 (i.e. Cohen's d=-0.20 for 2014-2015) and having a large amount of reduction in CO emission level in 2016 compared to 2015 (i.e. Cohen's d=0.82 for 2015-2016), indicating that there were temporal fluctuations in the CO emission levels.

When benzene emission levels for Famagusta station were analyzed using Figure 6, numerically the highest benzene emission level was observed in 2014 and therefore deductions from independent samples t-test between 2013 to 2014 and between 2014 to 2015 were discussed below in detail whereas relevant results about the other years were also included in Table 4. In Famagusta station at 2013 even the skewness<|2|, the kurtosis was found to be greater than |9.0|, therefore benzene emissions were found not to be normally distributed and hence t-test could not be conducted on Famagusta station for 2013. At 2014 and 2015, benzene emissions were sufficiently normal for the purpose of conducting a t-test and the variances between benzene emissions at 2014 and 2015 were not assumed to be equal via Levene's F-test, F(717)=16.195, p<0.001. The independent samples t-test was associated with a statistically significant effect, t (686.126) =15.687, p<0.001. Thus, in Famagusta station, benzene emission levels for 2014 were associated with a statistically significant different mean than 2015. Cohen's d was estimated at 1.20, which was a very large decreasing effect. From Table 4, it can be concluded that even the mean benzene emission levels were decreased from 2011 to 2012 with a statistically significantly small amount with Cohen's d=0.35, the mean benzene emission levels in the following two years increased until 2014 when the peak value was reached over the six years in Famagusta. After this peak point, statistically significantly very large amount of decrease, with Cohen's d=1.20, in benzene emission levels were observed for the following year, from 2014 to 2015. However, the large amount of decrease is replaced with a medium effect of increase with Cohen's d=-0.68 in the last year from 2015 to 2016.

3.2.2.3. Nicosia Station

In Nicosia station at 2011 and 2012, CO emissions were sufficiently normal for the purpose of conducting a t-test and variances between CO emissions in Nicosia station at 2011 and 2012 were assumed to be equal via Levene's F-test, F(724)=0.167, p=0.683. The independent samples t-test was associated with a statistically significant effect, t (724) =-8.643, p<0.001. Thus, in Nicosia station, CO emissions for 2011 were associated with a statistically significant different mean than 2012. Cohen's d was estimated at -0.64, which was a medium increasing effect from 2011 to 2012. In Nicosia at 2012 and 2013, CO emissions were also found to be normally distributed. However, variances between CO emission levels in Nicosia station at 2012 and 2013 were not assumed to be equal via Levene's F-test, F(681)=13.275, p<0.001. The independent samples t-test was associated with a statistically significant effect, t (539.135) =3.658, p<0.001. Thus, in Nicosia, the CO emissions for 2012 were associated with a statistically significant different mean than 2013. Cohen's d was estimated at 0.32, which was a small decreasing effect from 2012 to 2013. From those results presented in Table 4, it can be concluded that even the mean differences of CO emission levels between most of the years in Nicosia station were statistically significant, in the last three years from 2013-2015 a small change is observed and the difference of mean CO emissions between 2014-2015 was not even statistically significant.

From the results of independent samples t-test performed for each station to compare the means of CO emission levels between each two consecutive years, as tabulated in Table 4, it can be concluded that in Kyrenia and Nicosia, there were statistically significant differences between mean CO emission levels at the early years (i.e. between 2011-2012, 2012-2013) and not a statistically significant difference at the last two years (i.e. between 2014-2015 in both cities, between 2015-2016 in Kyrenia). However, in Famagusta station, there was a statistically significant difference between mean CO emissions throughout all years tested in this research.

In Nicosia at 2011 and 2012, the benzene emissions were sufficiently normal for conducting a t-test and the variances between benzene emissions at 2011 and 2012 were not assumed to be equal via Levene's F-test, F(666)=17.002, $p<0.001$. The independent samples t-test was associated with a statistically significant effect, t (597.823) =-3.023, p=0.003. Thus, in Nicosia station, benzene emissions for 2011 were associated with a statistically significantly different mean than 2012. Cohen's d was estimated at -0.25, which was a small effect. In Nicosia station at 2012 and 2013 benzene emissions were also found to be normally distributed and variances of benzene emissions between 2012 and 2013 were not assumed to be equal via Levene's F-test, F(588)=39.849, $p<0.001$. The independent samples t-test was not associated with a statistically significant effect, t (570.249) =1.744, p=0.082. Thus, in Nicosia station, benzene emissions for 2012 were not associated with a statistically significantly different mean than 2013.

In Nicosia station at 2013 and 2014 benzene emissions were normally distributed and the variances between benzene emissions at 2013 and 2014 were not assumed to be equal via Levene's F-test, F(650)=85.842, $p<0.001$. The independent samples t-test was associated with a statistically significant effect, t (396.270) =16.852, $p<0.001$. Thus, in Nicosia station, mean benzene emissions for 2013 were associated with a statistically significant different than 2014. Cohen's d was estimated at 1.69, which is nearly huge effect, indicating a large decrease from 2013 to 2014.

From the results of independent samples t-test performed on each station to compare the means of benzene emission levels between each two consecutive years, it can be concluded that the peak benzene emission level for Nicosia over the six years from 2011 to 2016 is observed at 2012 where this peak in Nicosia station is observed at the earliest year compared to other stations; Kyrenia (at 2013) and Famagusta (at 2014). In Nicosia station, comparing the benzene emission levels of 2011 with 2012, a small significant increase (Cohen's d=-0.25) is observed. It was also determined that the decrease in the mean benzene emission level from 2012 to 2013 was not significant. After 2013, a huge decreasing effect (Cohen's d=1.69) was obtained in benzene emission levels from 2013 to 2014 and after this huge effect, a very small increasing effect (with Cohen's d=-0.01 which was statistically insignificant as shown in Table 3) and a medium decreasing effect (Cohen's d=0.44) were achieved for the consecutive years in between 2014-2015 and 2015-2016 respectively. In overall, the effects over the last three years from 2014 to 2016 resulted in a decrease in mean benzene emission levels. From these results, we can strongly conclude that there were statistically significant differences in annual mean CO and benzene emissions in North Cyprus between the years, within each city, indicating the existence of temporal variations in emissions, even though in some few years no changing effects or only small effects were recorded.

3.2.3. Inferential analyses on geographical variations in annual mean CO and benzene emissions

One of the main objectives of this study was to determine any annual differences in emissions with respect to geographical location. Accordingly, the independent samples t-test was conducted to compare the CO and benzene emission levels between any two stations at each year (within the same year) and the results were given in Table 5.

Table 5. Differences between the stations within the same year

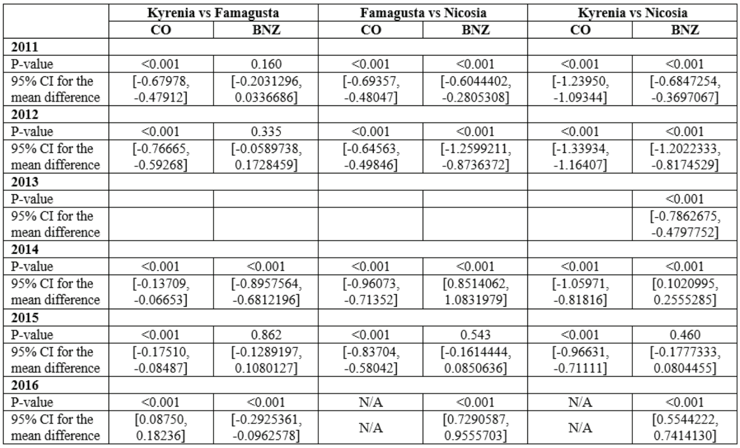

	Kyrenia vs Famagusta		**Famagusta vs Nicosia**		**Kyrenia vs Nicosia**	
	CO	**BNZ**	**CO**	**BNZ**	**CO**	**BNZ**
2011						
P-value	<0.001	0.160	<0.001	<0.001	<0.001	<0.001
95% CI for the mean difference	[-0.67978, -0.47912]	[-0.2031296, 0.0336686]	[-0.69357, -0.48047]	[-0.6044402, -0.2805308]	[-1.23950, -1.09344]	[-0.6847254, -0.3697067]
2012						
P-value	<0.001	0.335	<0.001	<0.001	<0.001	<0.001
95% CI for the mean difference	[-0.76665, -0.59268]	[-0.0589738, 0.1728459]	[-0.64563, -0.49846]	[-1.2599211, -0.8736372]	[-1.33934, -1.16407]	[-1.2022333, -0.8174529]
2013						
P-value						<0.001
95% CI for the mean difference						[-0.7862675, -0.4797752]
2014						
P-value	<0.001	<0.001	<0.001	<0.001	<0.001	<0.001
95% CI for the mean difference	[-0.13709, -0.06653]	[-0.8957564, -0.6812196]	[-0.96073, -0.71352]	[0.8514062, 1.0831979]	[-1.05971, -0.81816]	[0.1020995, 0.2555285]
2015						
P-value	<0.001	0.862	<0.001	0.543	<0.001	0.460
95% CI for the mean difference	[-0.17510, -0.08487]	[-0.1289197, 0.1080127]	[-0.83704, -0.58042]	[-0.1614444, 0.0850636]	[-0.96631, -0.71111]	[-0.1777333, 0.0804455]
2016						
P-value	<0.001	<0.001	N/A	<0.001	N/A	<0.001
95% CI for the mean difference	[0.08750, 0.18236]	[-0.2925361, -0.0962578]	N/A	[0.7290587, 0.9555703]	N/A	[0.5544222, 0.7414130]

As shown in Table 5, the independent samples t-test was conducted to compare the annual mean CO emission levels in Kyrenia and Famagusta, in Famagusta and Nicosia and in Kyrenia and Nicosia respectively in the years; 2011, 2012, 2014, 2015 and 2016. Since distribution of CO emissions in 2013 were determined not to be normal the independent samples t-test could not be performed for 2013. These results showed that there were significant differences in CO emission levels between the stations in all five years separately as obtained by $p<0.001$. Therefore, these results suggested that the location of the station (i.e. Kyrenia or Famagusta or Nicosia) did have an effect on CO emission levels and hence indicated that there were statistically significant differences in CO emission levels in different cities in North Cyprus due to geographical location. The independent samples t-test was conducted to compare the annual mean benzene emissions in between Kyrenia and Famagusta, Famagusta and Nicosia, and Kyrenia and Nicosia, respectively in all of the six years; 2011, 2012, 2013, 2014, 2015 and 2016. These results, as represented in Table 5, showed that there were significant differences in benzene emission levels between Famagusta and Nicosia stations, and between Kyrenia and Nicosia stations in both 2011 and 2012 whereas there were not statistically significant differences between Kyrenia and Famagusta in both 2011 and 2012. Since the distribution of benzene emission levels in 2013 in Famagusta station was not normally distributed, an independent samples t-test could not be performed when comparing with Famagusta station in 2013. However, the comparison of mean annual benzene emission levels between Kyrenia and Nicosia station in 2013 indicated that there was also statistically significant difference between both cities. Even though the results in 2015 indicated that there were not statistically significant differences in mean benzene emission levels between any two stations, the results in 2014 and 2016 show that there were statistically significant differences in mean benzene emission levels between all stations. These results suggested that the geographical location of the city did only have a partial effect on the observed mean annual benzene emission levels in North Cyprus. Based on all the results shown in Table 5, it was not unusual to observe statistical differences in mean CO emission levels between all stations for all years and some major statistical differences in mean benzene emission levels between most stations for most years since all three cities have different levels of population and, different emission inventories due to different levels of industrial activities and traffic loads.

3.3. Diurnal Fluctuations in Hourly CO and Benzene Emission Levels

To get more insight about correlations that may exist between CO and benzene emissions, it was first necessary to study the diurnal emissions more closely in the three cities; accordingly, two separate data sets were selected and used from the measurements of January and July 2015, to represent the cold and hot seasons, for all cities, respectively. The year of 2015 was selected for the diurnal studies since it was the most recent year when both CO and benzene emissions data were recorded in all three stations. In order to study the weekday and weekend diurnal emission profiles, the second week of the month was selected for both January and July; the data for diurnal benzene emissions were plotted in Figure 7 and the data for diurnal CO emissions were plotted in Figure 8, respectively. In all cities, in both seasons, there were remarkable differences between the weekday and weekend benzene and CO emission levels; the weekend emission levels were lower than the weekday levels for all cities in both cold and hot seasons. However, when the weekday and weekend CO and benzene emissions were more carefully compared, similar diurnal emission trends were traced for both seasons, indicating some probable linear correlation between CO and benzene emission levels. During the weekdays, in both seasons, the benzene and CO emissions were observed to rise to two peak values, at morning and late afternoon traffic rush hours, with the latter continuing till night, resulting in two maxima. In the cold seasons, for weekdays, the morning rush hour peaks in benzene and CO emissions were observed to be directly from the automobile exhaust emissions in traffic and household fossil fuel burning, whereas in the hot seasons these morning rush hour emissions were mainly due to traffic and were lower than the concentrations measured in the cold seasons. In the cold seasons, for weekdays, the peak benzene and CO emissions observed in late afternoon till midnight, were due to both traffic emissions and household fossil fuel burning, and were higher in magnitude than those peak emissions measured in the weekday hot seasons coming from the traffic load only. During the weekends, both in cold and hot seasons, benzene and CO emissions were lower in magnitude than the weekday emission levels; these weekend emissions, in both seasons, were characterized with a single peak occurring at between 15:00–22:00 p.m. In the cold seasons, these emissions were due both traffic and household heating, whereas in the hot seasons, they were only due to exhaust gases discharged in traffic. The similar cycles observed in CO and benzene emissions, in both cold and hot seasons, rising to peak values and going down to minimum values within the same time interval of the day showed the existence of correlations between CO and benzene emissions.

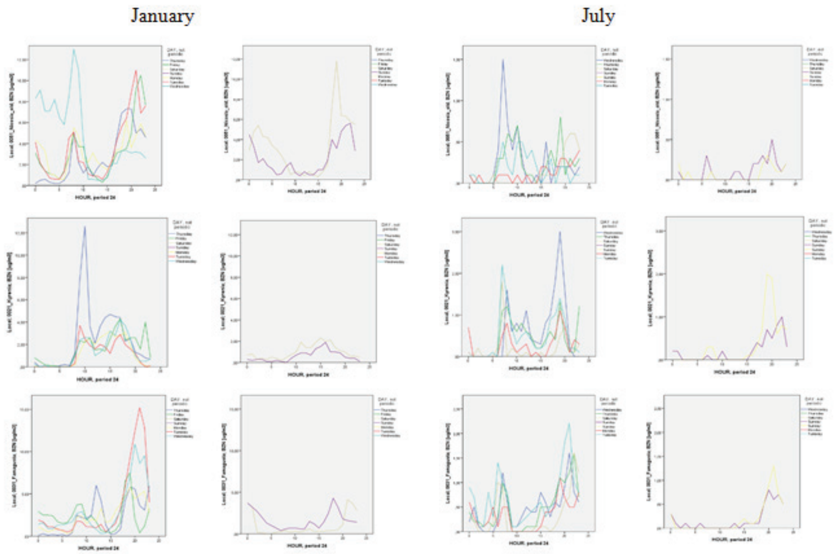

Fig.7. Diurnal benzene emission levels measured at the second week in January and July 2015.

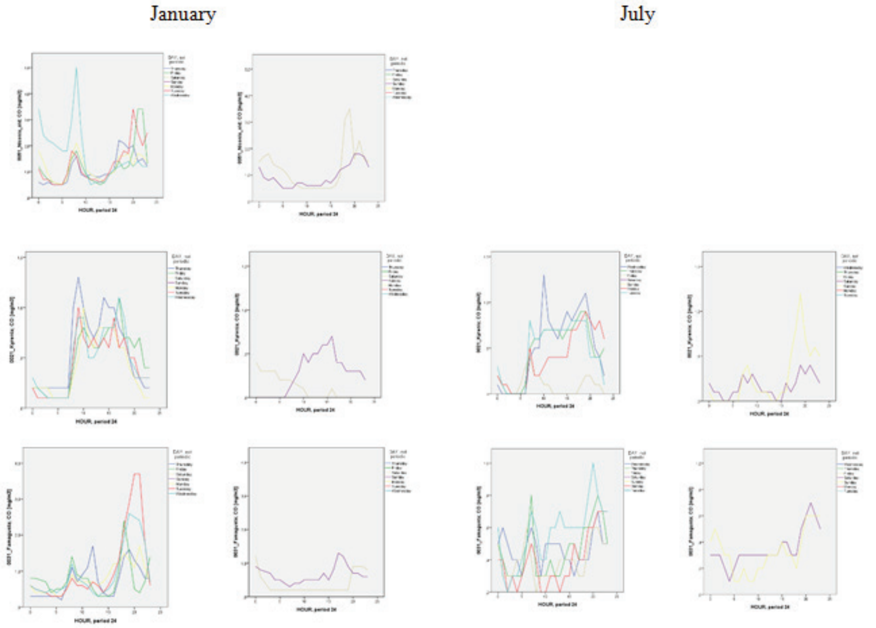

Fig. 8. Diurnal CO emission levels measured at the second week in January and July 2015.

3.4. Correlations Between the Daily CO and Benzene Emissions

In order to study the correlation between benzene and CO emission levels, the daily emission values of CO and benzene emissions (as explained in section 2.2.) were used. The Pearson Correlation coefficient (r) was calculated in the correlation studies for each year, except 2013. Since benzene and CO emission levels were not normally distributed in 2013, a nonparametric correlation statistic namely the Spherman Correlation coefficient (r) was used instead to investigate the correlation between both pollutants in 2013. Firstly, all available data values on daily CO emission levels obtained at a specific year were combined to form a data set on CO emission levels on a yearly base, for each specific station. Similarly, for each year, the daily calculated benzene emission data values at a specific year were combined to include all available data and form a data set for each station. The daily values were preferably used to minimize the effect of fluctuations that might result from the hourly base measurements. The correlations between CO and benzene emissions were determined; for the years 2011, 2012, 2014, 2015 and 2016, the Pearson's correlation coefficients and for 2013, the equivalent non-parametric Spherman correlation coefficient were estimated and tabulated in Table 6, respectively.

Table 6. *Correlation coefficients of CO and benzene for each year from 2011-2016*

	Benzene					
CO	2011	2012	2013	2014	2015	2016
Kyrenia						
Correlation coefficient	0.244	-0.107	0.402	0.372	0.453	0.564
P-value	$p<0.001$	0.053	$p<0.001$	$p<0.001$	$p<0.001$	$p<0.001$
Famagusta						
Correlation coefficient	0.637	-0.189	0.636	0.640	0.792	0.665
P-value	$p<0.001$	$p<0.001$	$p<0.001$	$p<0.001$	$p<0.001$	$p<0.001$
Nicosia						
Correlation coefficient	0.684	-0.044	0.292	0.757	0.687	N/A
P-value	$p<0.001$	0.445	$p<0.001$	$p<0.001$	$p<0.001$	N/A

In Nicosia, since the equipment measuring the CO emission level was impaired in 2016, there were no records of CO emission levels and no correlations could be performed for Nicosia in 2016; though, significant correlations of medium to high strength were obtained for Kyrenia and Famagusta in 2016, respectively. The results tabulated in Table

6 indicated that there were moderate (Kyrenia) to strong (Famagusta and Nicosia) positive correlations which were statistically significant between CO and benzene emission levels in all three stations, in all years, except 2012. The highest relationship for Famagusta occurred at 2015 with r=0.792, p<0.001, for Nicosia station occurred at 2014 with r=0.757, p<0.001 and for Kyrenia station occurred at 2016 with r=0.564, p<0.001. The correlation coefficients calculated between CO and benzene emissions in 2012 for all cities were negative. In order to understand the reason underlying this result, Figures 3 and 4 for 2012, were carefully investigated. In fall 2012, as the CO emissions tended to decrease, the benzene emissions were observed to increase simultaneously whereas in spring and summer times of 2012, decreasing patterns in benzene emissions were followed by increasing patterns of CO emissions for the same period. These observations together with the correlation results of 2012 and the highest levels of CO pollution observed in all cities directed us to conclude that there were external factors affecting the benzene and CO pollution levels in 2012 in terms of discharges from external sources together with transport effects of massive air currents. Thus, it was concluded that there were no statistically significant correlations between CO and benzene emissions in all cities in 2012 and the highest levels of CO emissions observed were at least partially due to external discharges and atmospheric transport processes.

As discussed in section 3.2.2, the distributions of CO emission levels were statistically different in 2012 when compared with before 2012 and after 2012. The highest CO emission levels were attained in all cities in 2012 with some external influences coming into action as depicted by negative correlation coefficients; these in turn should have caused some shifts in the 2013 benzene and CO emissions levels since, in all of the years, the emissions in CO and benzene were normally distributed except 2013. Therefore, the correlations between CO and benzene emission levels were all conducted using the Pearson's Correlation Coefficient test, except in 2013, when the Spherman correlation coefficient was used. Even though the Spherman correlation coefficient was very useful in the analyses, due to the above-mentioned reasons, correlations between CO and benzene emission levels were compared only between the years 2011, 2014 and 2015. When the correlations between CO and benzene emission levels were compared separately for each of those years, statistically significant relations were observed within each year where the weakest correlations between CO and benzene emission levels were obtained in Kyrenia for all three years (2011, 2014 and 2015). In 2011 and 2014, the highest correlations were found in Nicosia whereas in 2015, the highest correlation was in Famagusta. In all of the three years, when the association between

CO and benzene emission levels was compared within the stations, the strength of the association was found to be different over the years in all three stations. The strength of correlations was increased over time from 2011 to 2015 in Kyrenia and Famagusta whereas the strength of this association was decreased from 2014 to 2015 for Nicosia. Among the years compared, the latest where both CO and benzene emission levels were recorded in all three stations was 2015; therefore, this year was selected for further linear regression analyses and the correlations between CO and benzene emissions for all stations in 2015 were plotted as scatter graphs in Fig. 9.

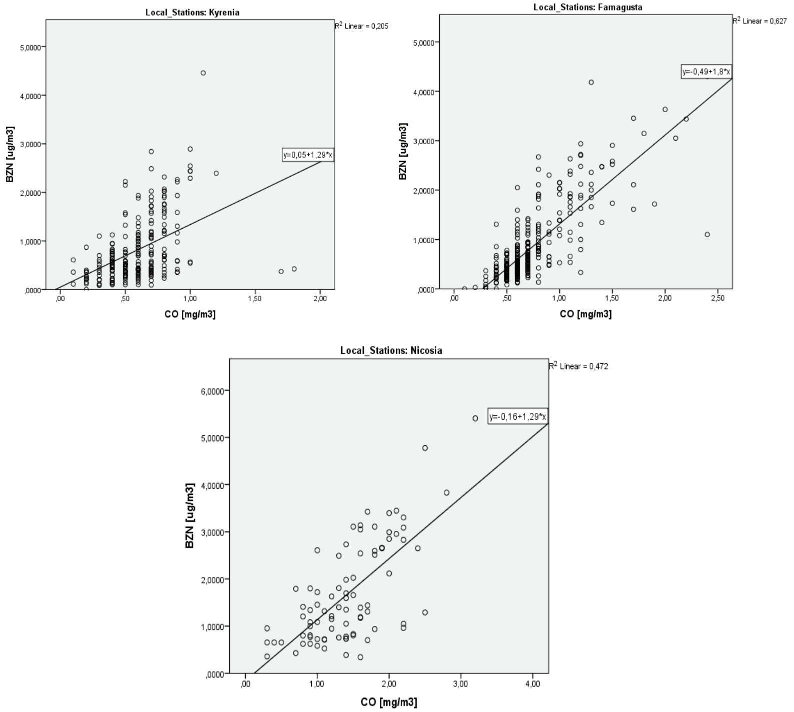

Fig. 9. *Correlations between CO and benzene emissions in 2015 for all stations.*

In Fig. 9, the lines of best fit were drawn, the equations for the corresponding best fit line were given and the R^2 values were reported to indicate the strength of correlation for each city. As depicted in Fig. 9, the strongest correlation between CO and benzene emission levels was observed in Famagusta and the weakest correlation was found in Kyrenia, in 2015. The presence of statistically significant correlations, moderate in Kyrenia and strong in Nicosia and Famagusta, showed us that both CO and benzene emissions were source related in terms atmospheric discharges. This fact was also evidenced by the presence of similar cycles in benzene and CO diurnal emissions for all cities in 2015, as shown in figures 7 and 8. The peaks in both emissions corresponded to times of discharges related with traffic and household heating activities. Therefore, from the statistical evidence in Table 6 and from the data in Figures 7, 8 and 9 it was concluded that there were strong correlations between CO and benzene emissions in North Cyprus since most of the emission discharges were from the same two sources, namely the traffic and household heating.

4. SUMMARY AND CONCLUSIONS

Based on the daily values, temporal variations existed in both CO and benzene emissions in all cities in between 2011-2016 (Fig. 2). Benzene emissions were characterized with seasonal cycles (Fig. 4) but there were no seasonal cyclic trends associated with CO emissions (Fig. 3) in all cities. It was concluded that Nicosia was the most polluted city in CO emissions (Figures 3 and 5) though based on the comparison of the maximum daily eight-hour rolling averages with 10 mg/m^3 (the limit value set by the European Directive), there were no exceedances of the limit value in all cities throughout the whole period including the most polluted city, Nicosia. Even though all mean annual benzene emissions were below 5 µg/m^3 (limit set for annual exposure to benzene by the European Directive) (Fig. 6) some of the daily benzene emissions were above the upper threshold limit, 3.5 µg/m^3 (set by the European Directive for benzene exposure) (Fig. 4). Some of the hourly benzene emissions were even higher than 5 µg/m^3 (maximum limit set for benzene exposure) (Fig. 7) in winter seasons at the weekdays, at morning and evening traffic rush hours and at night hours with intense household heating. This exceedance in benzene emissions above safe limits may impose a health hazard on people who get occupational exposure in open atmosphere. World Health Organization (WHO) stated that certain exposure levels to benzene in air may cause leukaemia and reported that, for general guidance, the concentrations of airborne benzene associated with an excess lifetime risk of leukaemia of 10^{-4}, 10^{-5} and 10^{-6} were 17, 1.7 and 0.17 µg/m^3, respectively (World Health Organisation, 2000b). In overall, the inferential analyses performed and explained in section 3.2.2., and summarized above showed that there were temporal variations in the mean annual CO and benzene emissions within the years 2011-2016, in each city, even though in some few cases no statistical changes were determined.

The differences in the mean annual benzene and CO emissions were also investigated between the stations within the same year as tabulated in Table 5. The results were analyzed in section 3.2.3. and it was concluded that there were significant differences in the mean CO emissions with respect to the cities in each year between 2011-2016, except 2013 (distribution of CO emissions was not normal), showing the effect of geographical location on CO emissions. As outlined in section 3.2.3., the geographical location of the city had only a partial effect on the mean benzene distributions investigated during 2011-2016, as shown in Table 5. When the diurnal CO and benzene emission levels were investigated based on hourly measured values (section 3.3) the weekend diurnal levels were determined to be lower than the weekday levels indicating lower pollution levels at the weekends in both cold and hot seasons, in all cities. In both cold and hot seasons, the weekday diurnal emissions were characterized with two peaks: the first one occurring at morning traffic rush hours and the second one occurring at early evening, in all cities. For all seasons, the weekend diurnal emissions were determined to peak in the afternoon at around 03:00-04:00 p.m. or generally at early evening at around 07:00-08:00 p.m., respectively, in all cities. In the cold seasons, the peak weekday and weekend diurnal emissions were due to traffic and household heating, but in the hot seasons the weekday and weekend diurnal peak emissions were due to traffic load only, respectively, in all cities. In overall, in both hot and cold seasons, the weekend and the weekday CO and benzene emissions were characterized with similar trends and peaks (similar diurnal cycles) confirming the presence of correlation between CO and benzene emissions, in all cities. In order to investigate the correlation levels between CO and benzene emissions, the Pearson and Spherman correlation coefficients were evaluated for emissions in all cities through 2011-2016 by using the daily emission levels. In all years, except 2012, there were moderate positive (Kyrenia) to strong positive significant correlations (Famagusta and Nicosia) between CO and benzene emissions in North Cyprus (Table 6 and Fig. 9), showing that both CO and benzene emissions were originating from the same sources, mainly traffic and household heating. Even the highest CO emission levels were observed in 2012, the negative Pearson coefficients calculated in 2012 (Table 6) have shown that both emission levels were at least partially attributed to discharge interferences from external sources.

REFERENCES

Sheps, D. S., Adams Jr, K. F., Bromberg, P. A., Goldstein, G. M., O'Neil, J. J., Horstman, D., & Koch, G. (1987). Lack of effect of low levels of carboxyhemoglobin on cardiovascular function in patients with ischemic heart disease. *Archives of Environmental Health: An International Journal*, *42*(2), 108-116.

Baudic, A., Gros, V., Sauvage, S., Locoge, N., Sanchez, O., Sarda-Estève, R., ... & Favez, O. (2016). Seasonal variability and source apportionment of volatile organic compounds (VOCs) in the Paris megacity (France). *Atmospheric Chemistry and Physics*, *16*(18), 11961-11989.

Cohen, J., (1988). Statistical *Power Analysis for the Behavioural Sciences* (2nd ed.). Lawrence Erlbaum Associates Publishers, Hillsdale, New York.

Cohen, J. (1992). Methods in psychology. *A power primer. Psychological Bulletin*, *112*(1), 155-159.

CRC Handbook of Chemistry and Physics (2005) . *Lide, D.R. (Ed.), 86th edition*. CRC Press, ISBN 0-8493-0486-5.

Debevec, C., Sauvage, S., Gros, V., Sciare, J., Pikridas, M., Stavroulas, I., ... & Fronval, I. (2017). Origin and variability in volatile organic compounds observed at an Eastern Mediterranean background site (Cyprus). *Atmospheric Chemistry and Physics*, *17*(18), 11355.

Duncan, B. N., Logan, J. A., Bey, I., Megretskaia, I. A., Yantosca, R. M., Novelli, P. C., ... & Rinsland, C. P. (2007). Global budget of CO, 1988–1997: Source estimates and validation with a global model. *Journal of Geophysical Research: Atmospheres*, *112*(D22).

Elbir, T., Müezzinoğlu, A., & Bayram, A. (2000). Evaluation of some air pollution indicators in Turkey. *Environment International*, *26*(1-2), 5-10.

International Programme on Chemical Safety (IPCS) (1993). *Environmental Health Criteria 150; Benzene. World Health Organization, Geneva* retrieved from http://www.inchem.org/documents/ehc/ehc/ehc150.htm (accessed in May 2018).

Kountouriotis, A., Aleiferis, P. G., & Charalambides, A. G. (2014). Numerical investigation of VOC levels in the area of petrol stations. *Science of the total environment*, *470*, 1205-1224.

Kushta, J., Georgiou, G. K., Proestos, Y., Christoudias, T., & Lelieveld, J. (2018). Modelling study of the atmospheric composition over Cyprus. *Atmospheric Pollution Research*, *9*(2), 257-269.

Middleton, N., Yiallouros, P., Nicolaou, N., Kleanthous, S., Pipis, S., Zeniou, M., ... & Koutrakis, P. (2010). Residential exposure to motor vehicle emissions and the risk of wheezing among 7-8 year-old schoolchildren: a city-wide cross-sectional study in Nicosia, Cyprus. *Environmental Health*, *9*(1), 28.

Myriokefalitakis, S., Daskalakis, N., Fanourgakis, G. S., Voulgarakis, A., Krol, M. C., de Brugh, J. A., & Kanakidou, M. (2016). Ozone and carbon monoxide budgets over the Eastern Mediterranean. *Science of The Total Environment*, *563*, 40-52.

Park, K., & Rhee, T. S. (2015). Source characterization of carbon monoxide and ozone over the Northwestern Pacific in summer 2012. *Atmospheric Environment*, *111*, 151-160.

Paxton, M. B., Chinchilli, V. M., Brett, S. M., & Rodricks, J. V. (1994). Leukemia risk associated with benzene exposure in the pliofilm cohort: I. Mortality update and exposure distribution. *Risk analysis*, *14*(2), 147-154.

Peavy, H.S., Rowe, D.R., Tchobanoglous, G. (1985). *Environmental Engineering , in: Verma, K. and Damstra, D.A. (Eds.).* Mc-Graw Hill Company, 445-447.

Retama, A., Baumgardner, D., Raga, G. B., McMeeking, G. R., & Walker, J. W. (2015). Seasonal and diurnal trends in black carbon properties and co-pollutants in Mexico City. *Atmospheric Chemistry and Physics*, *15*(16), 9693.

Revokatova, A. P. (2013). A method of carbon monoxide emission forecast in Moscow. *Russian Meteorology and Hydrology*, *38*(6), 396-404.

Salameh, T., Borbon, A., Afif, C., Sauvage, S., Leonardis, T., Gaimoz, C., Locoge, N. (2017). *Composition of Gaseous Organic Carbon during ECOCEM in Beirut, Lebanon: New Observational Constraints for VOC Antropogenic Emission Evaluation in the Middle East. Atmospheric Chemistry and Physics*, 17, 193-209.

Schmider, E., Ziegler, M., Danay, E., Beyer, L., Buehner, M., (2010). Is It Really Robust? Methodology. *European Journal of Research Methods for the Behavioural and Social Sciences.* 6(4), 147-151.

Sheps, D. S., Adams Jr, K. F., Bromberg, P. A., Goldstein, G. M., O'Neil, J. J., Horstman, D., & Koch, G. (1987). Lack of effect of low levels of carboxyhemoglobin on cardiovascular function in patients with ischemic heart disease. *Archives of Environmental Health: An International Journal*, *42*(2), 108-116.

Sicard, P., De Marco, A., Troussier, F., Renou, C., Vas, N., & Paoletti, E. (2013). Decrease in surface ozone concentrations at Mediterranean remote sites and increase in the cities. *Atmospheric Environment*, *79*, 705-715.

Technical report 3. Ecotech Model 9830 analyzer CO Analyzer. (2018). Available at: https://www.ecotech.com/wp-content/uploads/2015/03/EC9830B-Brochure.pdf (accessed in August 2018).

US Environmental Protection Agency, (1991). *Air Quality Criteria for Carbon Monoxide*. Washington, DC. (Publication EPA-600/B-90/045F).

UNION, PEAN. “Directive 2008/50/EC of the European Parliament and of the Council of 21 May 2008 on ambient air quality and cleaner air for Europe.” *Official Journal of the European Union* (2008).

Topacoglu, H., Katsakoglou, S., & Ipekci, A. (2014). Effect of exhaust emissions on carbon monoxide levels in employees working at indoor car wash facilities. *Hippokratia*, *18*(1), 37.

TRNC State Planning Organisation, Press Release , TRNC Population and Household Count, (2011). Available at: http://www.devplan.org/nufus-2011/nufus%20son_.pdf (accessed in September 2018).

Tsilingiridis, G., Sidiropoulos, C., Pentaliotis, A., Evripidou, C., Papastavros, C., Mesimeris, T., & Papastavrou, M. (2010). A spatially allocated emissions inventory for Cyprus. *Global NEST Journal*, *12*(434), 99-107.

Turnbull, J. C., Tans, P. P., Lehman, S. J., Baker, D., Conway, T. J., Chung, Y. S., ... & Zhou, L. X. (2011). Atmospheric observations of carbon monoxide and fossil fuel CO2 emissions from East Asia. *Journal of Geophysical Research: Atmospheres*, *116*(D24).

Zhong, Q., Huang, Y., Shen, H., Chen, Y., Chen, H., Huang, T., ... & Tao, S. (2017). Global estimates of carbon monoxide emissions from 1960 to 2013. *Environmental Science and Pollution Research*, *24*(1), 864-873.

Yadav, R., Sahu, L. K., Beig, G., Tripathi, N., & Jaaffrey, S. N. A. (2017). Ambient particulate matter and carbon monoxide at an urban site of India: influence of anthropogenic emissions and dust storms. *Environmental Pollution*, *225*, 291-303.

Wolf, P. C. (1971). Carbon Monoxide–Measurement and Monitorong in Urban Air Environment. *Sei and Technol*. 5, 231.

World Health Organisation, (2000a). *Carbon Monoxide. in; Air Quality Guidelines for Europe. World Health Organization Regional Office for Europe Regional Publications, European Series, No. 91, 2nd ed.* Available at: http://www.euro.who.int/__data/assets/pdf_file/0005/74732/E71922.pdf (accessed in September 2018).

World Health Organisation, (2000b). *Benzene. in; Air Quality Guidelines for Europe. World Health Organization Regional Office for Europe Regional Publications, European Series, No. 91, 2nd ed.* Available at: http://www.euro.who.int/__data/assets/pdf_file/0005/74732/E71922.pdf (accessed in September 2018).

Chapter 6

HALF VALUE LAYER, TENTH VALUE LAYER AND MEAN FREE PATH DETERMINATION OF THERMOLUMINESCENT DOSIMETRIC COMPOUNDS

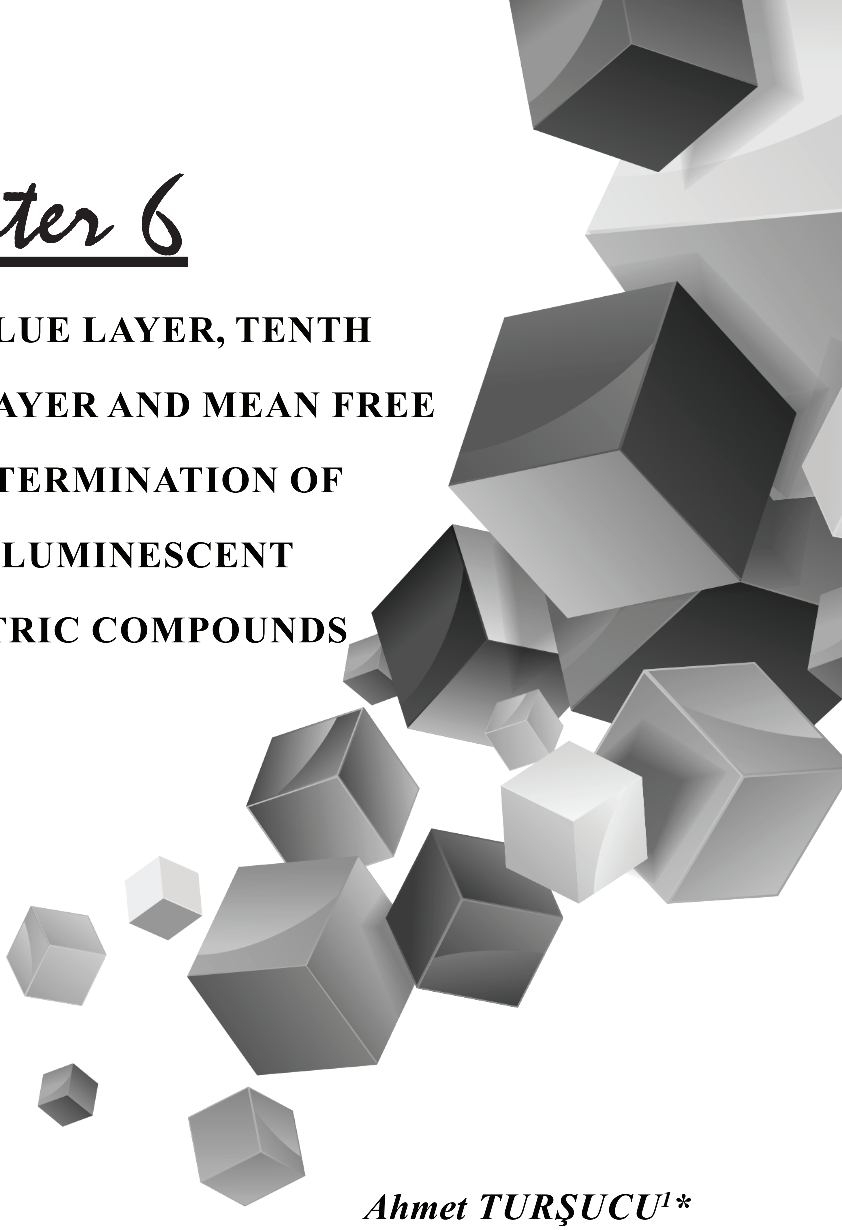

Ahmet TURŞUCU[1]*

1

---

[1] Corresponding author. Tel: + 90 442 231 41 40 E-mail address: ahmettursucu@atauni.edu.tr (A. Turşucu) Department of Electrical & Electronics Engineering, Faculty of Engineering Sirnak University, 73000 Sirnak, Turkey

[*] Sirnak University Technology and Research Centre, 73000 Sirnak, Turkey

1. Introduction

Nuclear energy is a kind of energy derived from the nucleus of the atom. Nuclear energy is recognized as one of the most important energy sources of today and the future. The fact that oil and natural gas are in large reserves in some countries and these resources cannot be renewed has led many countries to benefit from nuclear research and nuclear energy. However, various disasters have occurred in the last 60 years. The impact of nuclear disasters is really terrible. Nowadays, scientists have focused on reducing the effects of nuclear disasters and manufacturing new radiation shielding materials. These radiation shielding materials have widely used in nuclear power plants, nuclear engineering, medical physics, and radiation therapy applications.

Gamma-active radioactive isotopes have used in the determination processes of radiation the shielding parameters. The radiation shielding parameters have composed of an effective atomic number and effective electron density, attenuation coefficient, half-value layer, tenth value layer, mean free path, exposure buildup factor (EBF) and energy absorption buildup factor (EABF) components. These components have been calculated by using different experimental techniques and X-ray fluorescence spectroscopy is one of them. The calculation of the radiation shielding properties has been carried out in two different techniques. One of these techniques is the total photon interaction calculation by using transmission experiments and the other technique was scattering intensity ratio method. The scattering intensity ratio method has been recently introduced and the advantage of this technique depended on a mixture of composite sample material and regardless of the density of the sample. Also, the energy dependence of the radiation shielding parameter can be measured by using the transition method.

The incident strength values of the gamma-ray have attenuated by the thickness of shielding material to one half of incident strength and this phenomenon has been called the half-value layer. In addition, when the attenuation value of incident gamma-ray intensity by using the thicknesses of target material has been reached ten percent, this phenomenon has been called the tenth value layer (TVL). The incident gamma-ray has impinged in target medium and interaction was occurred with atomic clusters. The mean free path (MFP) is the average distance traveled by a gamma ray in the target sample before an interaction takes place [1].

The determination of the radiation shielding properties has become an attractive issue in recent years. Researchers have been used different target samples and different gamma-ray sources in their experiments. Nair et al.have measured mass attenuation coefficients of lead, aluminum, copper, and liquid mercury in various thicknesses [2]. They used 662 keV gamma rays of ^{137}Cs radioactive source, and the experiment was carried out with pure elements and some of their combinations. Kadam et al. have measured the effective atomic number and mass attenuation coefficient of magnesium ferrite [3]. For this purpose, they were used four different gamma-ray source ^{137}Cs, ^{133}Ba, ^{60}Co, and ^{22}Na respectively. The energy range of these radioactive gamma sources is between 0.360 MeV and 1.28 MeV. Rao et al. have determined the effective atomic number of monel metal and tungsten steel [4]. In the experimental procedure, they were used NaI(Tl) scintillation spectrometer at various energies that vary from 145 keV to 1330 keV.

In this present study, the HVL, TVL and MFP values of different TLD compounds have been determined. The experiment has been carried out by using the VEX radioactive source, 10 mCi^{133}Ba and ^{137}Cs radioactive sources. The attenuated values of gamma-ray photons have been collected by using the HPGe semiconductor detector.

2. Theory

In general, when an x-ray impinges upon a sample, three things may happen: the incident x-ray may be diffracted, scattered, or absorbed. In the calculation procedure of the mass attenuation coefficient parameter, the absorbed and transmitted dose of incident radiation is an important parameter. All materials could be used as a radiation shielding material in certain thicknesses. Thus, this situation has shown that the radiation shielding phenomena were related to the density of shielding material. The theoretical and experimental studies were shown that the dense and the higher atomic number materials beneficial in radiation shielding applications. There are many different radiation shielding parameters and the mass attenuation coefficient is only one of them. In the experimental calculation procedure of the mass attenuation coefficient parameter, the transmission geometry has been used. According to the transmission geometry, the incident intensity and the attenuated intensity of gamma or x-ray have been determined by using detection systems. Then, the incident and attenuated gamma or x-ray values have been used in Beer-Lambert's law. According to the Beer Lambert's law, the incident radiation is attenuating exponentially by the target and the attenuation equation is given below,

$$I = I_0 e^{-(\mu/\rho)d} \tag{1}$$

where I and I_0 represents the attenuated and incident radiation, the (μ/ρ) expression represents the mass attenuation coefficient and d is representing the mass per unit area, respectively.

The target materials that were used in this experimental study composed of two or more element. These compound materials have unique mass attenuation coefficients and calculated by using mixture rule. The mixture rule is carried out by using the material weight fraction of each component. The atomic wave function of used target samples is affected by chemical, molecular and crystal environment, normally. The mixture rule ignores these situations [5].

According to the mixture rule, the mass attenuation of any compound is calculating via the following equation

$$\frac{\mu}{\rho} = \sum_i w_i \, (\mu/\rho)_i \qquad (2)$$

where w_i is the weight fraction of element in the material and $(\mu/\rho)_i$ is the mass attenuation of i.th element in the material.

2.1. Half value layer, tenth value layer and mean free path

The half-value layer, tenth value layer, and the mean free path parameters are using in medical applications like radiation therapy. The thickness of the target material and the attenuation value of incident radiation are directly proportional. The half-value layer parameter has known as the thicknesses of the target material that was attenuated %50 of the incident radiation energy. The half-value layer, tenth value layer and the mean free path of any target was calculated by using the following equation,

$$HVL = \frac{\ln 2}{\mu} = \frac{0.693}{\mu}$$

$$TVL = \frac{\ln 10}{\mu} = \frac{2.303}{\mu} \qquad (3)$$

$$MFP = 1/\mu$$

3. Experimental setup and present measurements

This present work has been aimed at the determination of HVL, TVL and MFP parameters of thermoluminescent materials. The related parameters were calculated by using mass attenuation values of specimens. The mass attenuation values of the thermoluminescent materials have been calculated in our previous study. The previous study has been carried out by using transition method and HPGe semiconductor detector [6]. The semiconductor detector was used to collecting the attenuated gamma-rays. The specifications of used detector were given by Table 1. The incident gamma-rays were produced by a radioactive source that was used in the experimental setup and attenuated by target samples. Two different radioactive sources have been used in the mass attenuation calculations and these different sources were emitted 8 keV to 661 keV gamma-ray energies.

Table 1. The characteristics specifications of HPGe detector.

Active Diameter	16 mm
Active Area	200 mm^2
Sensitive Detector Depth	10 mm
Distance From Window	5 mm
Beryllium window thickness	0.12 mm
Supply Voltage	-1500 V
Resolution (5,9-122 keV)	182-488 eV

The schematic diagram of experimental arrangement was given by Fig.1 and Fig.2. As seen from the arrangement figure, the transition geometry was used, and attenuated gamma photons have been collected by using HPGe semiconductor detector. The attenuated gamma-ray spectrums were processed by Pc-based multichannel analyzer card (Accuspec). The analyzer card has been developed by Canberra. The detector was coupled with amplifier to obtain best counting rates. All these specifications have been controlled by using pc-based program Genie-2000. The obtained values of attenuation levels of gamma-rays have been analyzed by Origin 7.5 and spectrum areas were determined.

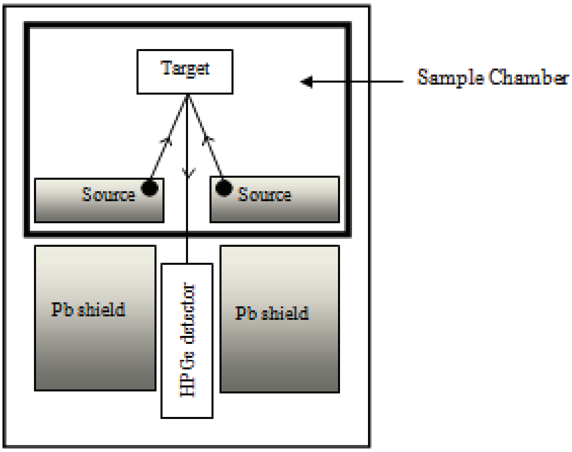

Figure 1. *Experimental setup (radius of collimator is 0.53 cm). This figure is only a schematic diagram of experimental setup.*

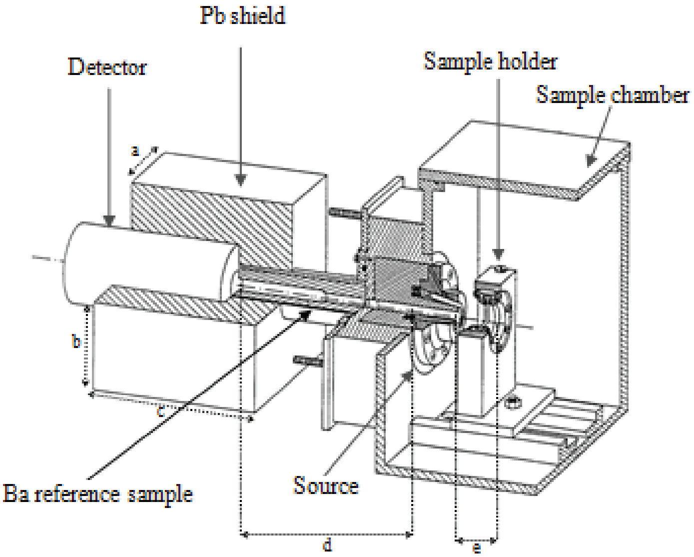

Figure 2. *Sample chamber (a=6.5 cm, b=6.3 cm, c=13.5 cm, d=11 cm, e=5 cm).*

4. Result and discussion

Knowing the radiation shielding level of materials is important in nuclear power plants and in very large areas where daily x-ray use is made. For this purpose, quite a lot of researcher was focused on this subject. They have used different materials and different determination techniques.

Some atomic parameters like the mass attenuation coefficient, the effective atomic number, and the electron densities were calculated and submitted in our earlier paper. The present work was focused on the determination of some radiation shielding parameters of thermoluminescent dosimetric compounds. For this purpose, the mass attenuation coefficients of the target's samples were measured by using experimental techniques. The experimental setup was composed of a radiation source and a semiconductor detector. In this setup, the attenuated percentage of incident radiation dose was calculated determined and used in the calculation of the mass attenuation coefficient parameter.

The samples used in this experimental procedure were quite important materials because of their wide usage. These samples were used in medical physics, laser, radioisotope monitoring, neutron computing, and especially radiation shielding applications. Their radiation shielding values were needed to be measured carefully. The radiation shielding values of related target samples were calculated in a single energy parameter.

The radiation shielding parameter calculation has been carried out by using the calculated values of the mass attenuation parameter. For this purpose, the attenuated and the incident photon spectrums were carefully plotted as a function of the channel firstly. Besides, the channel count and background count corrections were applied.

The HVL, TVL ,and MFP values of the thermoluminescent dosimetric compounds have been given by Table-2, Table-3 ,and Table-4, respectively. It is clearly seen that the deduced experimental values are in good accordance with calculated theoretical values. There is very limited information in the literature about these parameters of the selected thermoluminescent samples. To obtain more definite information about the radiation shielding parameter (HVL, TVL and MFP) of the thermoluminescent samples, researchers must do different experimental measurements in different gamma energies and also, different photon energies.

Table 2 Mass attenuation coefficients (cm^2/g) and HVL values of some TLD compounds.

Energy (keV)	Compound									
	$MgSO_4$		Mg_2SiO_4		SiO_2		$CdSO_4$		$ZnSO_4$	
	μ	HVL	μ	HVL	μ	HVL	μ	HVL	μ	HVL
8.04	38.45 ± 2.73	0.018	31.29 ± 2.22	0.022	35.95 ± 2.55	0.019	135.11 ± 9.60	0.005	45.59 ± 3.24	0.015
8.91	28.52 ± 2.03	0.024	23.18 ± 1.64	0.030	26.55 ± 1.89	0.026	102.12 ± 7.25	0.007	34.22 ± 2.43	0.020
13.37	8.72 ± 0.62	0.079	7.10 ± 0.50	0.098	8.19 ± 0.58	0.085	34.21 ± 2.42	0.020	48.91 ± 3.48	0.014
14.97	6.39 ± 0.45	0.108	5.13 ± 0.36	0.135	5.84 ± 0.42	0.119	25.15 ± 1.78	0.028	36.10 ± 2.56	0.019
17.44	4.11 ± 0.29	0.169	3.20 ± 0.23	0.217	3.74 ± 0.27	0.185	16.55 ± 1.18	0.042	23.81 ± 1.69	0.029
19.63	2.95 ± 0.21	0.235	2.38 ± 0.16	0.291	2.62 ± 0.19	0.265	12.10 ± 0.85	0.057	17.22 ± 1.22	0.040
22.10	2.11 ± 0.15	0.328	1.61 ± 0.12	0.430	1.99 ± 0.14	0.348	8.72 ± 0.62	0.079	12.41 ± 0.88	0.056
24.90	1.52 ± 0.11	0.456	1.25 ± 0.09	0.554	1.39 ± 0.10	0.499	6.29 ± 0.45	0.110	8.81 ± 0.63	0.079
30.82	0.88 ± 0.06	0.788	0.73 ± 0.05	0.949	0.81 ± 0.06	0.856	19.10 ± 1.35	0.036	4.91 ± 0.35	0.141
32.06	0.82 ± 0.06	0.845	0.65 ± 0.05	1.066	0.74 ± 0.05	0.936	17.16 ± 1.22	0.040	4.43 ± 0.32	0.156
35.40	0.63 ± 0.05	1.100	0.53 ± 0.04	1.308	0.60 ± 0.04	1.155	13.25 ± 0.94	0.052	3.35 ± 0.24	0.207
36.39	0.61 ± 0.04	1.136	0.51 ± 0.04	1.359	0.55 ± 0.04	1.260	12.36 ± 0.87	0.056	3.10 ± 0.22	0.224
37.26	0.58 ± 0.04	1.195	0.48 ± 0.03	1.444	0.54 ± 0.04	1.283	11.69 ± 0.82	0.059	2.90 ± 0.21	0.239
43.74	0.41 ± 0.03	1.690	0.35 ± 0.03	1.980	0.39 ± 0.03	1.777	7.51 ± 0.54	0.092	1.91 ± 0.14	0.363
44.48	0.40 ± 0.03	1.733	0.34 ± 0.02	2.038	0.37 ± 0.03	1.873	7.21 ± 0.52	0.096	1.82 ± 0.13	0.381
50.38	0.32 ± 0.02	2.166	0.29 ± 0.02	2.390	0.32 ± 0.02	2.166	5.20 ± 0.37	0.133	1.32 ± 0.09	0.525
51.70	0.31 ± 0.02	2.235	0.27 ± 0.02	2.567	0.30 ± 0.02	2.310	4.87 ± 0.35	0.142	1.21 ± 0.09	0.573
53.16	0.30 ± 0.02	2.310	0.27 ± 0.02	2.567	0.28 ± 0.02	2.475	4.52 ± 0.32	0.153	1.14 ± 0.08	0.608
80.99	0.19 ± 0.01	3.647	0.17 ± 0.01	4.076	0.18 ± 0.01	3.850	1.48 ± 0.11	0.468	0.43 ± 0.03	1.612
276.40	0.11 ± 0.01	6.300	0.11 ± 0.01	6.300	0.11 ± 0.01	6.300	0.14 ± 0.01	4.950	0.10 ± 0.01	6.930
302.85	0.10 ± 0.01	6.930	0.11 ± 0.01	6.300	0.10 ± 0.01	6.930	0.12 ± 0.01	5.775	0.10 ± 0.01	6.930
356.01	0.10 ± 0.01	6.930	0.10 ± 0.01	6.930	0.10 ± 0.01	6.930	0.11 ± 0.01	6.300	0.10 ± 0.01	6.930
383.85	0.10 ± 0.01	6.930	0.09 ± 0.01	7.700	0.10 ± 0.01	6.930	0.11 ± 0.01	6.300	0.09 ± 0.01	7.700
661.66	0.07 ± 0.01	9.900	0.07 ± 0.01	9.900	0.07 ± 0.01	9.900	0.07 ± 0.01	9.900	0.07 ± 0.01	9.900

Energy (keV)	Compound									
	$CaSO_4$		CaF_2		$Ca_5F(PO_4)_3$		$CaCO_3$		Al_2O_3	
	μ	HVL	μ	HVL	μ	HVL	μ	HVL	μ	HVL
8.04	75.85 ± 5.39	0.009	93.08 ± 6.61	0.007	85.39 ± 6.06	0.008	72.60 ± 5.17	0.010	26.95 ± 1.91	0.026
8.91	57.11 ± 4.05	0.012	70.10 ± 4.98	0.010	64.22 ± 4.56	0.011	54.82 ± 3.90	0.013	19.99 ± 1.41	0.035
13.37	18.19 ± 1.29	0.038	22.35 ± 1.59	0.031	20.42 ± 1.45	0.034	17.54 ± 1.24	0.040	6.11 ± 0.43	0.113
14.97	13.12 ± 0.93	0.053	16.25 ± 1.15	0.043	14.75 ± 1.05	0.047	12.72 ± 0.90	0.054	4.30 ± 0.31	0.161
17.44	8.42 ± 0.60	0.082	10.45 ± 0.75	0.066	9.59 ± 0.68	0.072	8.21 ± 0.59	0.084	2.88 ± 0.20	0.241

19.63	6.02 ± 0.43	0.115	7.41 ± 0.53	0.094	6.83 ± 0.48	0.101	5.81 ± 0.42	0.119	2.10 ± 0.14	0.330
22.10	4.33 ± 0.31	0.160	5.30 ± 0.38	0.131	4.86 ± 0.35	0.143	4.29 ± 0.30	0.162	1.42 ± 0.10	0.488
24.90	3.14 ± 0.22	0.221	3.70 ± 0.27	0.187	3.46 ± 0.24	0.200	2.90 ± 0.21	0.239	1.14 ± 0.08	0.608
30.82	1.79 ± 0.12	0.387	2.18 ± 0.15	0.318	1.90 ± 0.14	0.365	1.68 ± 0.12	0.413	0.64 ± 0.05	1.083
32.06	1.54 ± 0.11	0.450	1.81 ± 0.13	0.383	1.73 ± 0.12	0.401	1.50 ± 0.11	0.462	0.58 ± 0.04	1.195
35.40	1.17 ± 0.08	0.592	1.49 ± 0.10	0.465	1.39 ± 0.09	0.499	1.15 ± 0.08	0.603	0.47 ± 0.03	1.474
36.39	1.11 ± 0.08	0.624	1.37 ± 0.10	0.506	1.24 ± 0.09	0.559	1.13 ± 0.08	0.613	0.46 ± 0.03	1.507
37.26	1.12 ± 0.07	0.619	1.21 ± 0.09	0.573	1.11 ± 0.08	0.624	1.05 ± 0.07	0.660	0.44 ± 0.03	1.575
43.74	0.71 ± 0.05	0.976	0.84 ± 0.06	0.825	0.78 ± 0.06	0.888	0.71 ± 0.05	0.976	0.34 ± 0.02	2.038
44.48	0.66 ± 0.05	1.050	0.80 ± 0.06	0.866	0.74 ± 0.05	0.936	0.67 ± 0.05	1.034	0.31 ± 0.02	2.235
50.38	0.53 ± 0.04	1.308	0.62 ± 0.04	1.118	0.57 ± 0.04	1.216	0.51 ± 0.04	1.359	0.28 ± 0.02	2.475
51.70	0.49 ± 0.04	1.414	0.55 ± 0.04	1.260	0.54 ± 0.04	1.283	0.48 ± 0.03	1.444	0.25 ± 0.02	2.772
53.16	0.46 ± 0.03	1.507	0.54 ± 0.04	1.283	0.51 ± 0.04	1.359	0.46 ± 0.03	1.507	0.26 ± 0.02	2.665
80.99	0.23 ± 0.02	3.013	0.25 ± 0.02	2.772	0.24 ± 0.02	2.888	0.23 ± 0.02	3.013	0.17 ± 0.01	4.076
276.40	0.11 ± 0.01	6.300	0.11 ± 0.01	6.300	0.11 ± 0.01	6.300	0.10 ± 0.01	6.930	0.10 ± 0.01	6.930
302.85	0.10 ± 0.01	6.930	0.10 ± 0.01	6.930	0.10 ± 0.01	6.930	0.10 ± 0.01	6.930	0.10 ± 0.01	6.930
356.01	0.10 ± 0.01	6.930	0.10 ± 0.01	6.930	0.10 ± 0.01	6.930	0.10 ± 0.01	6.930	0.10 ± 0.01	6.930
383.85	0.09 ± 0.01	7.700	0.09 ± 0.01	7.700	0.10 ± 0.01	6.930	0.10 ± 0.01	6.930	0.10 ± 0.01	6.930
661.66	0.07 ± 0.01	9.900	0.07 ± 0.01	9.900	0.08 ± 0.01	9.900	0.07 ± 0.01	9.900	0.07 ± 0.01	9.900

Energy (keV)	Compound					
	$NaSO_4$		$Na_4P_2O_7$		$BaSO_4$	
	μ	HVL	μ	HVL	μ	HVL
8.04	36.29 ± 2.58	0.019	32.33 ±2.30	0.021	203.23±14.43	0.003
8.91	27.11 ± 1.92	0.026	23.94 ±1.70	0.029	154.00±10.95	0.005
13.37	8.33 ± 0.59	0.083	7.21 ± 0.52	0.096	52.41 ± 3.73	0.013
14.97	5.90 ± 0.43	0.117	5.20 ± 0.37	0.133	38.82 ± 2.76	0.018
17.44	3.84 ± 0.27	0.180	3.31 ± 0.24	0.209	25.75 ± 1.83	0.027
19.63	2.72 ± 0.20	0.255	2.40 ± 0.17	0.289	18.72 ± 1.33	0.037
22.10	1.97 ± 0.14	0.352	1.71 ± 0.12	0.405	13.52 ± 0.97	0.051
24.90	1.42 ± 0.10	0.488	1.22 ± 0.09	0.568	9.71 ± 0.70	0.071
30.82	0.82 ± 0.06	0.845	0.74 ± 0.05	0.936	5.52 ± 0.40	0.126
32.06	0.75 ± 0.05	0.924	0.67 ± 0.05	1.034	5.04 ± 0.36	0.138
35.40	0.60 ± 0.04	1.155	0.54 ± 0.04	1.283	3.89 ± 0.28	0.178
36.39	0.56 ± 0.04	1.238	0.51 ± 0.04	1.359	3.59 ± 0.26	0.193
37.26	0.54 ± 0.04	1.283	0.49 ± 0.04	1.414	3.40 ± 0.24	0.204
43.74	0.40 ± 0.03	1.733	0.36 ± 0.03	1.925	11.00 ± 0.80	0.063
44.48	0.38 ± 0.03	1.824	0.34 ± 0.03	2.038	10.70 ± 0.77	0.065
50.38	0.32 ± 0.02	2.166	0.28 ± 0.02	2.475	7.83 ± 0.56	0.089
51.70	0.31 ± 0.02	2.235	0.27 ± 0.02	2.567	7.36 ± 0.52	0.094
53.16	0.30 ± 0.02	2.310	0.28 ± 0.02	2.475	6.79 ± 0.48	0.102
80.99	0.18 ± 0.01	3.850	0.18 ± 0.01	3.850	2.21 ± 0.16	0.305
276.40	0.11 ± 0.01	6.300	0.10 ± 0.01	6.930	0.16 ± 0.01	4.331
302.85	0.11 ± 0.01	6.300	0.10 ± 0.01	6.930	0.14 ± 0.01	4.950
356.01	0.11 ± 0.01	6.300	0.10 ± 0.01	6.930	0.12 ± 0.01	5.775
383.85	0.10 ± 0.01	6.930	0.10 ± 0.01	6.930	0.11 ± 0.01	6.300
661.66	0.07 ± 0.01	9.900	0.07 ± 0.01	9.900	0.07 ± 0.01	9.900

Table 3 Mass attenuation coefficients (cm^2/g) and TVL values of some TLD compounds.

Energy (keV)	Compound									
	$MgSO_4$		Mg_2SiO_4		SiO_2		$CdSO_4$		$ZnSO_4$	
	μ	TVL	μ	TVL	μ	TVL	μ	TVL	μ	TVL
8.04	38.45 ± 2.73	0.060	31.29 ± 2.22	0.074	35.95 ± 2.55	0.064	135.11 ± 9.60	0.017	45.59 ± 3.24	0.051
8.91	28.52 ± 2.03	0.081	23.18 ± 1.64	0.099	26.55 ± 1.89	0.087	102.12 ± 7.25	0.023	34.22 ± 2.43	0.067
13.37	8.72 ± 0.62	0.264	7.10 ± 0.50	0.324	8.19 ± 0.58	0.281	34.21 ± 2.42	0.067	48.91 ± 3.48	0.047
14.97	6.39 ± 0.45	0.360	5.13 ± 0.36	0.449	5.84 ± 0.42	0.394	25.15 ± 1.78	0.092	36.10 ± 2.56	0.064
17.44	4.11 ± 0.29	0.560	3.20 ± 0.23	0.720	3.74 ± 0.27	0.616	16.55 ± 1.18	0.139	23.81 ± 1.69	0.097
19.63	2.95 ± 0.21	0.781	2.38 ± 0.16	0.968	2.62 ± 0.19	0.879	12.10 ± 0.85	0.190	17.22 ± 1.22	0.134
22.10	2.11 ± 0.15	1.091	1.61 ± 0.12	1.430	1.99 ± 0.14	1.157	8.72 ± 0.62	0.264	12.41 ± 0.88	0.186
24.90	1.52 ± 0.11	1.515	1.25 ± 0.09	1.842	1.39 ± 0.10	1.657	6.29 ± 0.45	0.366	8.81 ± 0.63	0.261
30.82	0.88 ± 0.06	2.617	0.73 ± 0.05	3.155	0.81 ± 0.06	2.843	19.10 ± 1.35	0.121	4.91 ± 0.35	0.469
32.06	0.82 ± 0.06	2.809	0.65 ± 0.05	3.543	0.74 ± 0.05	3.112	17.16 ± 1.22	0.134	4.43 ± 0.32	0.520
35.40	0.63 ± 0.05	3.656	0.53 ± 0.04	4.345	0.60 ± 0.04	3.838	13.25 ± 0.94	0.174	3.35 ± 0.24	0.687
36.39	0.61 ± 0.04	3.775	0.51 ± 0.04	4.516	0.55 ± 0.04	4.187	12.36 ± 0.87	0.186	3.10 ± 0.22	0.743
37.26	0.58 ± 0.04	3.971	0.48 ± 0.03	4.798	0.54 ± 0.04	4.265	11.69 ± 0.82	0.197	2.90 ± 0.21	0.794
43.74	0.41 ± 0.03	5.617	0.35 ± 0.03	6.580	0.39 ± 0.03	5.905	7.51 ± 0.54	0.307	1.91 ± 0.14	1.206
44.48	0.40 ± 0.03	5.758	0.34 ± 0.02	6.774	0.37 ± 0.03	6.224	7.21 ± 0.52	0.319	1.82 ± 0.13	1.265
50.38	0.32 ± 0.02	7.197	0.29 ± 0.02	7.941	0.32 ± 0.02	7.197	5.20 ± 0.37	0.443	1.32 ± 0.09	1.745
51.70	0.31 ± 0.02	7.429	0.27 ± 0.02	8.530	0.30 ± 0.02	7.677	4.87 ± 0.35	0.473	1.21 ± 0.09	1.903
53.16	0.30 ± 0.02	7.677	0.27 ± 0.02	8.530	0.28 ± 0.02	8.225	4.52 ± 0.32	0.510	1.14 ± 0.08	2.020
80.99	0.19 ± 0.01	12.121	0.17 ± 0.01	13.547	0.18 ± 0.01	12.794	1.48 ± 0.11	1.556	0.43 ± 0.03	5.356
276.40	0.11 ± 0.01	20.936	0.11 ± 0.01	20.936	0.11 ± 0.01	20.936	0.14 ± 0.01	16.450	0.10 ± 0.01	23.030
302.85	0.10 ± 0.01	23.030	0.11 ± 0.01	20.936	0.10 ± 0.01	23.030	0.12 ± 0.01	19.192	0.10 ± 0.01	23.030
356.01	0.10 ± 0.01	23.030	0.10 ± 0.01	23.030	0.10 ± 0.01	23.030	0.11 ± 0.01	20.936	0.10 ± 0.01	23.030
383.85	0.10 ± 0.01	23.030	0.09 ± 0.01	25.589	0.10 ± 0.01	23.030	0.11 ± 0.01	20.936	0.09 ± 0.01	25.589
661.66	0.07 ± 0.01	32.900	0.07 ± 0.01	32.900	0.07 ± 0.01	32.900	0.07 ± 0.01	32.900	0.07 ± 0.01	32.900

Energy (keV)	Compound									
	$CaSO_4$		CaF_2		$Ca_5F(PO_4)_3$		$CaCO_3$		Al_2O_3	
	μ	TVL	μ	TVL	μ	TVL	μ	TVL	μ	TVL
8.04	75.85 ± 5.39	0.030	93.08 ± 6.61	0.025	85.39 ± 6.06	0.027	72.60 ± 5.17	0.032	26.95 ± 1.91	0.085
8.91	57.11 ± 4.05	0.040	70.10 ± 4.98	0.033	64.22 ± 4.56	0.036	54.82 ± 3.90	0.042	19.99 ± 1.41	0.115
13.37	18.19 ± 1.29	0.127	22.35 ± 1.59	0.103	20.42 ± 1.45	0.113	17.54 ± 1.24	0.131	6.11 ± 0.43	0.377
14.97	13.12 ± 0.93	0.176	16.25 ± 1.15	0.142	14.75 ± 1.05	0.156	12.72 ± 0.90	0.181	4.30 ± 0.31	0.536
17.44	8.42 ± 0.60	0.274	10.45 ± 0.75	0.220	9.59 ± 0.68	0.240	8.21 ± 0.59	0.281	2.88 ± 0.20	0.800
19.63	6.02 ± 0.43	0.383	7.41 ± 0.53	0.311	6.83 ± 0.48	0.337	5.81 ± 0.42	0.396	2.10 ± 0.14	1.097
22.10	4.33 ± 0.31	0.532	5.30 ± 0.38	0.435	4.86 ± 0.35	0.474	4.29 ± 0.30	0.537	1.42 ± 0.10	1.622
24.90	3.14 ± 0.22	0.733	3.70 ± 0.27	0.622	3.46 ± 0.24	0.666	2.90 ± 0.21	0.794	1.14 ± 0.08	2.020
30.82	1.79 ± 0.12	1.287	2.18 ± 0.15	1.056	1.90 ± 0.14	1.212	1.68 ± 0.12	1.371	0.64 ± 0.05	3.598
32.06	1.54 ± 0.11	1.495	1.81 ± 0.13	1.272	1.73 ± 0.12	1.331	1.50 ± 0.11	1.535	0.58 ± 0.04	3.971
35.40	1.17 ± 0.08	1.968	1.49 ± 0.10	1.546	1.39 ± 0.09	1.657	1.15 ± 0.08	2.003	0.47 ± 0.03	4.900
36.39	1.11 ± 0.08	2.075	1.37 ± 0.10	1.681	1.24 ± 0.09	1.857	1.13 ± 0.08	2.038	0.46 ± 0.03	5.007
37.26	1.12 ± 0.07	2.056	1.21 ± 0.09	1.903	1.11 ± 0.08	2.075	1.05 ± 0.07	2.193	0.44 ± 0.03	5.234
43.74	0.71 ± 0.05	3.244	0.84 ± 0.06	2.742	0.78 ± 0.06	2.953	0.71 ± 0.05	3.244	0.34 ± 0.02	6.774
44.48	0.66 ± 0.05	3.489	0.80 ± 0.06	2.879	0.74 ± 0.05	3.112	0.67 ± 0.05	3.437	0.31 ± 0.02	7.429
50.38	0.53 ± 0.04	4.345	0.62 ± 0.04	3.715	0.57 ± 0.04	4.040	0.51 ± 0.04	4.516	0.28 ± 0.02	8.225
51.70	0.49 ± 0.04	4.700	0.55 ± 0.04	4.187	0.54 ± 0.04	4.265	0.48 ± 0.03	4.798	0.25 ± 0.02	9.212
53.16	0.46 ± 0.03	5.007	0.54 ± 0.04	4.265	0.51 ± 0.04	4.516	0.46 ± 0.03	5.007	0.26 ± 0.02	8.858
80.99	0.23 ± 0.02	10.013	0.25 ± 0.02	9.212	0.24 ± 0.02	9.596	0.23 ± 0.02	10.013	0.17 ± 0.01	13.547
276.40	0.11 ± 0.01	20.936	0.11 ± 0.01	20.936	0.11 ± 0.01	20.936	0.10 ± 0.01	23.030	0.10 ± 0.01	23.030
302.85	0.10 ± 0.01	23.030	0.10 ± 0.01	23.030	0.10 ± 0.01	23.030	0.10 ± 0.01	23.030	0.10 ± 0.01	23.030
356.01	0.10 ± 0.01	23.030	0.10 ± 0.01	23.030	0.10 ± 0.01	23.030	0.10 ± 0.01	23.030	0.10 ± 0.01	23.030
383.85	0.09 ± 0.01	25.589	0.09 ± 0.01	25.589	0.10 ± 0.01	23.030	0.10 ± 0.01	23.030	0.10 ± 0.01	23.030
661.66	0.07 ± 0.01	32.900	0.07 ± 0.01	32.900	0.08 ± 0.01	32.900	0.07 ± 0.01	32.900	0.07 ± 0.01	32.900

Energy (keV)	Compound					
	$NaSO_4$		$Na_4P_2O_7$		$BaSO_4$	
	μ	TVL	μ	TVL	μ	TVL
8.04	36.29 ± 2.58	0.063	32.33 ±2.30	0.071	203.23±14.43	0.011
8.91	27.11 ± 1.92	0.085	23.94 ±1.70	0.096	154.00±10.95	0.015
13.37	8.33 ± 0.59	0.276	7.21 ± 0.52	0.319	52.41 ± 3.73	0.044
14.97	5.90 ± 0.43	0.390	5.20 ± 0.37	0.443	38.82 ± 2.76	0.060
17.44	3.84 ± 0.27	0.600	3.31 ± 0.24	0.696	25.75 ± 1.83	0.089
19.63	2.72 ± 0.20	0.847	2.40 ± 0.17	0.960	18.72 ± 1.33	0.123
22.10	1.97 ± 0.14	1.169	1.71 ± 0.12	1.347	13.52 ± 0.97	0.170
24.90	1.42 ± 0.10	1.622	1.22 ± 0.09	1.888	9.71 ± 0.70	0.237
30.82	0.82 ± 0.06	2.809	0.74 ± 0.05	3.112	5.52 ± 0.40	0.417
32.06	0.75 ± 0.05	3.071	0.67 ± 0.05	3.437	5.04 ± 0.36	0.457
35.40	0.60 ± 0.04	3.838	0.54 ± 0.04	4.265	3.89 ± 0.28	0.592
36.39	0.56 ± 0.04	4.113	0.51 ± 0.04	4.516	3.59 ± 0.26	0.642
37.26	0.54 ± 0.04	4.265	0.49 ± 0.04	4.700	3.40 ± 0.24	0.677
43.74	0.40 ± 0.03	5.758	0.36 ± 0.03	6.397	11.00 ± 0.80	0.209
44.48	0.38 ± 0.03	6.061	0.34 ± 0.03	6.774	10.70 ± 0.77	0.215
50.38	0.32 ± 0.02	7.197	0.28 ± 0.02	8.225	7.83 ± 0.56	0.294
51.70	0.31 ± 0.02	7.429	0.27 ± 0.02	8.530	7.36 ± 0.52	0.313
53.16	0.30 ± 0.02	7.677	0.28 ± 0.02	8.225	6.79 ± 0.48	0.339
80.99	0.18 ± 0.01	12.794	0.18 ± 0.01	12.794	2.21 ± 0.16	1.015
276.40	0.11 ± 0.01	20.936	0.10 ± 0.01	23.030	0.16 ± 0.01	14.394
302.85	0.11 ± 0.01	20.936	0.10 ± 0.01	23.030	0.14 ± 0.01	16.450
356.01	0.11 ± 0.01	20.936	0.10 ± 0.01	23.030	0.12 ± 0.01	19.192
383.85	0.10 ± 0.01	23.030	0.10 ± 0.01	23.030	0.11 ± 0.01	20.936
661.66	0.07 ± 0.01	32.900	0.07 ± 0.01	32.900	0.07 ± 0.01	32.900

Table 4 Mass attenuation coefficients (cm^2/g) and MFP values of some TLD compounds.

Energy (keV)	Compound									
	$MgSO_4$		Mg_2SiO_4		SiO_2		$CdSO_4$		$ZnSO_4$	
	μ	MFP	μ	MFP	μ	MFP	μ	MFP	μ	MFP
8.04	38.45 ± 2.73	0.026	31.29 ± 2.22	0.032	35.95 ± 2.55	0.028	135.11 ± 9.60	0.007	45.59 ± 3.24	0.022
8.91	28.52 ± 2.03	0.035	23.18 ± 1.64	0.043	26.55 ± 1.89	0.038	102.12 ± 7.25	0.010	34.22 ± 2.43	0.029
13.37	8.72 ± 0.62	0.115	7.10 ± 0.50	0.141	8.19 ± 0.58	0.122	34.21 ± 2.42	0.029	48.91 ± 3.48	0.020
14.97	6.39 ± 0.45	0.156	5.13 ± 0.36	0.195	5.84 ± 0.42	0.171	25.15 ± 1.78	0.040	36.10 ± 2.56	0.028
17.44	4.11 ± 0.29	0.243	3.20 ± 0.23	0.313	3.74 ± 0.27	0.267	16.55 ± 1.18	0.060	23.81 ± 1.69	0.042
19.63	2.95 ± 0.21	0.339	2.38 ± 0.16	0.420	2.62 ± 0.19	0.382	12.10 ± 0.85	0.083	17.22 ± 1.22	0.058
22.10	2.11 ± 0.15	0.474	1.61 ± 0.12	0.621	1.99 ± 0.14	0.503	8.72 ± 0.62	0.115	12.41 ± 0.88	0.081
24.90	1.52 ± 0.11	0.658	1.25 ± 0.09	0.800	1.39 ± 0.10	0.719	6.29 ± 0.45	0.159	8.81 ± 0.63	0.114
30.82	0.88 ± 0.06	1.136	0.73 ± 0.05	1.370	0.81 ± 0.06	1.235	19.10 ± 1.35	0.052	4.91 ± 0.35	0.204
32.06	0.82 ± 0.06	1.220	0.65 ± 0.05	1.538	0.74 ± 0.05	1.351	17.16 ± 1.22	0.058	4.43 ± 0.32	0.226
35.40	0.63 ± 0.05	1.587	0.53 ± 0.04	1.887	0.60 ± 0.04	1.667	13.25 ± 0.94	0.075	3.35 ± 0.24	0.299
36.39	0.61 ± 0.04	1.639	0.51 ± 0.04	1.961	0.55 ± 0.04	1.818	12.36 ± 0.87	0.081	3.10 ± 0.22	0.323
37.26	0.58 ± 0.04	1.724	0.48 ± 0.03	2.083	0.54 ± 0.04	1.852	11.69 ± 0.82	0.086	2.90 ± 0.21	0.345
43.74	0.41 ± 0.03	2.439	0.35 ± 0.03	2.857	0.39 ± 0.03	2.564	7.51 ± 0.54	0.133	1.91 ± 0.14	0.524
44.48	0.40 ± 0.03	2.500	0.34 ± 0.02	2.941	0.37 ± 0.03	2.703	7.21 ± 0.52	0.139	1.82 ± 0.13	0.549
50.38	0.32 ± 0.02	3.125	0.29 ± 0.02	3.448	0.32 ± 0.02	3.125	5.20 ± 0.37	0.192	1.32 ± 0.09	0.758
51.70	0.31 ± 0.02	3.226	0.27 ± 0.02	3.704	0.30 ± 0.02	3.333	4.87 ± 0.35	0.205	1.21 ± 0.09	0.826
53.16	0.30 ± 0.02	3.333	0.27 ± 0.02	3.704	0.28 ± 0.02	3.571	4.52 ± 0.32	0.221	1.14 ± 0.08	0.877
80.99	0.19 ± 0.01	5.263	0.17 ± 0.01	5.882	0.18 ± 0.01	5.556	1.48 ± 0.11	0.676	0.43 ± 0.03	2.326
276.40	0.11 ± 0.01	9.091	0.11 ± 0.01	9.091	0.11 ± 0.01	9.091	0.14 ± 0.01	7.143	0.10 ± 0.01	10.000

302.85	0.10 ± 0.01	10.000	0.11 ± 0.01	9.091	0.10 ± 0.01	10.000	0.12 ± 0.01	8.333	0.10 ± 0.01	10.000
356.01	0.10 ± 0.01	10.000	0.10 ± 0.01	10.000	0.10 ± 0.01	10.000	0.11 ± 0.01	9.091	0.10 ± 0.01	10.000
383.85	0.10 ± 0.01	10.000	0.09 ± 0.01	11.111	0.10 ± 0.01	10.000	0.11 ± 0.01	9.091	0.09 ± 0.01	11.111
661.66	0.07 ± 0.01	14.286	0.07 ± 0.01	14.286	0.07 ± 0.01	14.286	0.07 ± 0.01	14.286	0.07 ± 0.01	14.286

Energy (keV)	Compound									
	$CaSO_4$		CaF_2		$Ca_5F(PO_4)_3$		$CaCO_3$		Al_2O_3	
	μ	MFP	μ	MFP	μ	MFP	μ	MFP	μ	MFP
8.04	75.85 ± 5.39	0.013	93.08 ± 6.61	0.011	85.39 ± 6.06	0.012	72.60 ± 5.17	0.014	26.95 ± 1.91	0.037
8.91	57.11 ± 4.05	0.018	70.10 ± 4.98	0.014	64.22 ± 4.56	0.016	54.82 ± 3.90	0.018	19.99 ± 1.41	0.050
13.37	18.19 ± 1.29	0.055	22.35 ± 1.59	0.045	20.42 ± 1.45	0.049	17.54 ± 1.24	0.057	6.11 ± 0.43	0.164
14.97	13.12 ± 0.93	0.076	16.25 ± 1.15	0.062	14.75 ± 1.05	0.068	12.72 ± 0.90	0.079	4.30 ± 0.31	0.233
17.44	8.42 ± 0.60	0.119	10.45 ± 0.75	0.096	9.59 ± 0.68	0.104	8.21 ± 0.59	0.122	2.88 ± 0.20	0.347
19.63	6.02 ± 0.43	0.166	7.41 ± 0.53	0.135	6.83 ± 0.48	0.146	5.81 ± 0.42	0.172	2.10 ± 0.14	0.476
22.10	4.33 ± 0.31	0.231	5.30 ± 0.38	0.189	4.86 ± 0.35	0.206	4.29 ± 0.30	0.233	1.42 ± 0.10	0.704
24.90	3.14 ± 0.22	0.318	3.70 ± 0.27	0.270	3.46 ± 0.24	0.289	2.90 ± 0.21	0.345	1.14 ± 0.08	0.877
30.82	1.79 ± 0.12	0.559	2.18 ± 0.15	0.459	1.90 ± 0.14	0.526	1.68 ± 0.12	0.595	0.64 ± 0.05	1.563
32.06	1.54 ± 0.11	0.649	1.81 ± 0.13	0.552	1.73 ± 0.12	0.578	1.50 ± 0.11	0.667	0.58 ± 0.04	1.724
35.40	1.17 ± 0.08	0.855	1.49 ± 0.10	0.671	1.39 ± 0.09	0.719	1.15 ± 0.08	0.870	0.47 ± 0.03	2.128
36.39	1.11 ± 0.08	0.901	1.37 ± 0.10	0.730	1.24 ± 0.09	0.806	1.13 ± 0.08	0.885	0.46 ± 0.03	2.174
37.26	1.12 ± 0.07	0.893	1.21 ± 0.09	0.826	1.11 ± 0.08	0.901	1.05 ± 0.07	0.952	0.44 ± 0.03	2.273
43.74	0.71 ± 0.05	1.408	0.84 ± 0.06	1.190	0.78 ± 0.06	1.282	0.71 ± 0.05	1.408	0.34 ± 0.02	2.941
44.48	0.66 ± 0.05	1.515	0.80 ± 0.06	1.250	0.74 ± 0.05	1.351	0.67 ± 0.05	1.493	0.31 ± 0.02	3.226
50.38	0.53 ± 0.04	1.887	0.62 ± 0.04	1.613	0.57 ± 0.04	1.754	0.51 ± 0.04	1.961	0.28 ± 0.02	3.571
51.70	0.49 ± 0.04	2.041	0.55 ± 0.04	1.818	0.54 ± 0.04	1.852	0.48 ± 0.03	2.083	0.25 ± 0.02	4.000
53.16	0.46 ± 0.03	2.174	0.54 ± 0.04	1.852	0.51 ± 0.04	1.961	0.46 ± 0.03	2.174	0.26 ± 0.02	3.846
80.99	0.23 ± 0.02	4.348	0.25 ± 0.02	4.000	0.24 ± 0.02	4.167	0.23 ± 0.02	4.348	0.17 ± 0.01	5.882
276.40	0.11 ± 0.01	9.091	0.11 ± 0.01	9.091	0.11 ± 0.01	9.091	0.10 ± 0.01	10.000	0.10 ± 0.01	10.000
302.85	0.10 ± 0.01	10.000	0.10 ± 0.01	10.000	0.10 ± 0.01	10.000	0.10 ± 0.01	10.000	0.10 ± 0.01	10.000
356.01	0.10 ± 0.01	10.000	0.10 ± 0.01	10.000	0.10 ± 0.01	10.000	0.10 ± 0.01	10.000	0.10 ± 0.01	10.000
383.85	0.09 ± 0.01	11.111	0.09 ± 0.01	11.111	0.10 ± 0.01	10.000	0.10 ± 0.01	10.000	0.10 ± 0.01	10.000
661.66	0.07 ± 0.01	14.286	0.07 ± 0.01	14.286	0.08 ± 0.01	14.286	0.07 ± 0.01	14.286	0.07 ± 0.01	14.286

Energy (keV)	Compound					
	$NaSO_4$		$Na_4P_2O_7$		$BaSO_4$	
	μ	MFP	μ	MFP	μ	MFP
8.04	36.29 ± 2.58	0.028	32.33 ±2.30	0.031	203.23±14.43	0.005
8.91	27.11 ± 1.92	0.037	23.94 ±1.70	0.042	154.00±10.95	0.006
13.37	8.33 ± 0.59	0.120	7.21 ± 0.52	0.139	52.41 ± 3.73	0.019
14.97	5.90 ± 0.43	0.169	5.20 ± 0.37	0.192	38.82 ± 2.76	0.026
17.44	3.84 ± 0.27	0.260	3.31 ± 0.24	0.302	25.75 ± 1.83	0.039
19.63	2.72 ± 0.20	0.368	2.40 ± 0.17	0.417	18.72 ± 1.33	0.053
22.10	1.97 ± 0.14	0.508	1.71 ± 0.12	0.585	13.52 ± 0.97	0.074
24.90	1.42 ± 0.10	0.704	1.22 ± 0.09	0.820	9.71 ± 0.70	0.103
30.82	0.82 ± 0.06	1.220	0.74 ± 0.05	1.351	5.52 ± 0.40	0.181
32.06	0.75 ± 0.05	1.333	0.67 ± 0.05	1.493	5.04 ± 0.36	0.198
35.40	0.60 ± 0.04	1.667	0.54 ± 0.04	1.852	3.89 ± 0.28	0.257
36.39	0.56 ± 0.04	1.786	0.51 ± 0.04	1.961	3.59 ± 0.26	0.279
37.26	0.54 ± 0.04	1.852	0.49 ± 0.04	2.041	3.40 ± 0.24	0.294
43.74	0.40 ± 0.03	2.500	0.36 ± 0.03	2.778	11.00 ± 0.80	0.091
44.48	0.38 ± 0.03	2.632	0.34 ± 0.03	2.941	10.70 ± 0.77	0.093
50.38	0.32 ± 0.02	3.125	0.28 ± 0.02	3.571	7.83 ± 0.56	0.128
51.70	0.31 ± 0.02	3.226	0.27 ± 0.02	3.704	7.36 ± 0.52	0.136
53.16	0.30 ± 0.02	3.333	0.28 ± 0.02	3.571	6.79 ± 0.48	0.147
80.99	0.18 ± 0.01	12.794	0.18 ± 0.01	5.556	2.21 ± 0.16	0.441

276.40	0.11 ± 0.01	20.936	0.10 ± 0.01	10.000	0.16 ± 0.01	6.250
302.85	0.11 ± 0.01	20.936	0.10 ± 0.01	10.000	0.14 ± 0.01	7.143
356.01	0.11 ± 0.01	20.936	0.10 ± 0.01	10.000	0.12 ± 0.01	8.333
383.85	0.10 ± 0.01	23.030	0.10 ± 0.01	10.000	0.11 ± 0.01	9.091
661.66	0.07 ± 0.01	14.286	0.07 ± 0.01	14.286	0.07 ± 0.01	14.286

REFERENCES

1. YASAKA, P., et al. Gamma radiation shielding and optical properties measurements of zinc bismuth borate glasses. Annals of Nuclear energy, 2014, 68: 4-9.
2. NAIR, K. Karunakaran, et al. Simulated mixed absorbers and effective atomic numbers for γ attenuation. Pramana, 2006, 67.3: 501.
3. KADAM, R. H., et al. Measurement of atomic number and mass attenuation coefficient in magnesium ferrite. Pramana, 2007, 68.5: 869-874.
4. RAO, K. Siva Sankara, et al. Studies on the effective atomic numbers of Monel metal and tungsten steel. Il Nuovo Cimento B (1971-1996), 1976, 33.2: 613-618.
5. KERUR, B. R.; THONTADARYA, S. R.; HANUMAIAH, B. Anomalous X-ray attenuation coefficients around the absorption edges using Mn Kα and Cu Kα X-rays. Applied radiation and isotopes, 1994, 45.2: 159-163.
6. ÖNDER, P., et al. Studies on mass attenuation coefficient, effective atomic number and electron density of some thermoluminescent dosimetric compounds. Nuclear Instruments and Methods in Physics Research Section B: Beam Interactions with Materials and Atoms, 2012, 292: 1-10.